# Imaging strategies in bone tissue engineering

Vincentius Matthias Josephus Ida Cuijpers

Publication of this thesis was financially supported by:
Radboud University Medical Center, Bruker microCT N.V.,
Alicona Imaging GmbH, CAM Bioceramics B.V.

## Colofon


Thesis Radboud University Medical Center, Nijmegen, The Netherlands,
with summary in English and Dutch

**Imaging strategies in bone tissue engineering**

| | |
|---|---|
| **Lay-out and cover design** | Vincent Cuijpers |
| **Printed by** | Ipskamp Printing |
| **ISBN** | 978-94-028-0057-9 |

# Imaging strategies in bone tissue engineering

## Proefschrift

**ter verkrijging van de graad van doctor**
**aan de Radboud Universiteit Nijmegen**
**op gezag van de rector magnificus,**
**volgens besluit van het college van decanen**
**in het openbaar te verdedigen op donderdag 14 april 2016**
**om 10.30 uur precies**

**door**

**Vincentius Matthias Josephus Ida Cuijpers**
**geboren op 11 december 1965**
**te Boxmeer**

**Promotor:**

Prof. dr. J.A. Jansen

**Copromotor:**

Dr. X.F. Walboomers

**Manuscriptcommissie:**

Prof. dr. ir. N.J.J. Verdonschot (voorzitter)
Prof. dr. J. Duyck (KU Leuven, België)
Prof. dr. P.J. Slootweg

**Paranimfen:**

Martijn W.W. Martens
Youri J.A. Cuijpers

# Imaging strategies in bone tissue engineering

## Doctoral Thesis

**to obtain the degree of doctor**
**from Radboud University Nijmegen**
**on the authority of the Rector Magnificus,**
**according to the decision of the Council of Deans**
**to be defended in public on Thursday, April 14, 2016**
**at 10.30 hours**

**by**

**Vincentius Matthias Josephus Ida Cuijpers**
**Born on December 11, 1965**
**in Boxmeer (the Netherlands)**

**Supervisor:**

Prof. dr. J.A. Jansen

**Co-Supervisor:**

Dr. X.F. Walboomers

**Doctoral Thesis Committee:**

Prof. dr. ir. N.J.J. Verdonschot (chairman)
Prof. dr. J. Duyck (KU Leuven, Belgium)
Prof. dr. P.J. Slootweg

**Ushers:**

Martijn W.W. Martens
Youri J.A. Cuijpers

*“It is costly wisdom that is bought by experience”*

Kostbaar is de wijsheid die door ervaring wordt verkregen.

Robert Ascham, 1515-1568

# CONTENTS

# CHAPTER 1

## General introduction

The aging of the world population and the associated increase in life expectancy, are demographic factors that will have a huge impact on medicine in the near future. These factors imply that more people will suffer from deteriorating, failing or malfunctioning body parts.[1]
Therefore, it is essential to expand age-related healthcare and further explore advances in medical technology. Innovative biomedical methodologies, such as the application of biomaterial scaffolds in tissue engineering research, were developed and are still subject of research to improve cell, tissue and organ properties and function in humans.[2]

## Tissue engineering and biomaterials

Every day, thousands of surgical procedures are performed in order to repair, replace, enhance and or maintain tissue function that has been damaged through disease, trauma or aging. The developing field of tissue engineering aims to regenerate these damaged tissues by combining cells with biomaterial scaffolds, which act as templates for tissue regeneration, to guide the growth of new tissue. Biomaterial scaffolds can be found in nature, or manufactured using a plethora of fabrication techniques using different approaches. These biomaterial scaffolds, mainly composed of biological and or metallic components or ceramics, must be compatible with the human body to perform, augment, or replace natural biological function of a living structure or biomedical device.[3] Tissue engineering research has yielded a novel set of biomaterial scaffolds and implementation strategies to be applied in orthopedic and dental applications, surgery and drug delivery.[4] Regardless of the tissue type, essential key considerations when designing or determining the suitability of a biomaterial scaffold for use, are the biocompatibility, biodegradability, mechanical properties, scaffold architecture, and manufacturing technology.[5] To monitor and assess processes in tissue engineering applications and biomaterial scaffold function, refined medical imaging techniques are crucial for comprehensive evaluation.

## Medical imaging

It is impossible to imagine modern medicine without the field of imaging. The development of the first microscope by Dutch man Zacharius Janssen in 1590 was a milestone in medical imaging, a magnified image of a "thin" slice of the object for the first time could be produced. Nowadays, it is possible to gather detailed information from tissues, cells and cell organelles at high resolution using microscopical imaging.
Another prominent medical imaging technique was discovered by Röntgen in 1895, by using the properties of X-radiation.[6] X-ray radiography is one of the oldest and most frequently used imaging technique when observing bone or dentition.
Over the last decennia, there has been a revolutionary progress in biomedical imaging, visualization and analysis.[7] There is an ongoing and continuous shift from relatively low resolution conventional two-dimensional imaging modalities to evaluate architecture of biological structures, to non-destructive high resolution advanced three-dimensional tomography imaging techniques to assess dynamics in biological processes, as well as in tissue engineering research.[8,9] Novel dedicated ultrasound-, magnetic resonance-, optical-, and radiology imaging techniques were developed to visualize structures at sub-micron scale and even on molecular and atomic level. However, X-ray imaging is still the most frequently applied imaging modality due its radio-absorbance characteristics and potential in clinical research.

## X-ray imaging, micro-computed tomography

Medical examinations using radiology tomography imaging, i.e. X-ray computed tomography (CT), are currently standard hospital practice. In tissue engineering research, the rapid evolving domain of high resolution CT also called micro-CT, is exceptionally functional to characterize and study the application and potential of scaffolds related to cells and biological structures *in vitro* as well as *in vivo*.[10] Especially bone and radiodense scaffold materials in tissue engineering are major subjects of research in micro-CT imaging.[11]
Nevertheless, a major limitation of X-ray attenuation based imaging is

formed by similar radiolucent characteristics of numerous tissues and scaffold materials in tissue engineering. The assessment of these structures using conventional micro-CT by implementing contrast is challenging, however can be greatly improved using enhanced technologies. Moreover, to improve contrast sensitivity and spatial resolution, X-ray imaging modalities as phase, scatter and fluorescence contrast X-ray imaging are investigated. Additionally, synchrotron light micro-CT expands the applications in the field of tissue engineering research and it is therefore currently applied.[12]

## Objectives of the thesis

The overall objectives of this thesis were to investigate fundamental imaging-based strategies to improve three-dimensional imaging in tissue engineering, and to enhance X-ray micro-computed tomography applications in biomaterial research. This includes techniques to achieve improved sensitivity and specificity, and 3D reconstruction techniques in both microscopy as wells as micro-computed tomography.
Animal models were used to identify the optimal combinations of defect model and imaging modality, depending on the specific application.

More specifically, the following research questions were covered:
1. What is the current state-of-the-art in biomaterial imaging?
2. Is there a straightforward technique to pinpoint biomaterials inside a specimen to facilitate histological tissue processing?
3. Is it possible to visualize and quantify cells on a biomaterial scaffold in 3D with conventional scanning electron microscopy?
4. Is high resolution / nano-computed tomography suitable to analyze sub-micron biomaterials and biological structures in 3D?
5. Is it possible to enhance contrast sensitivity of radiolucent biomaterials in micro-computed tomography imaging?
6. Are 3D bone dynamic studies possible, with a histological approach?

## REFERENCES


1. Christensen, K., Doblhammer, G., Rau, R., Vaupel, J.W., Ageing populations: the challenges ahead. Lancet. 2009;3;1196.
2. O'Brien, F.J., Biomaterials & scaffolds for tissue engineering. Mater Today. 2011;14:88-95.
3. Rebelo, M.A., Alves, T.F., Lima de, R., Oliveira Jr, J.M., Vila, M.M., Balcao, V.M., Balcão, V.M., Severino, P., Chaud, M.V., Scaffolds and tissue regeneration: An overview of the functional properties of selected organic tissues. J Biomedical Mater Res Part B, Appl Biomater. 2015.
4. Patel, M., Fisher, J.P., Pediatr Res. 2008;63:497-501.
5. Giannitelli, S.M., Accoto, D., Trombetta, M., Rainer, A., Current trends in the design of scaffolds for computer-aided tissue engineering. Acta Biomater. 2014;10:580-94.
6. Röntgen, W.C.. On a New Kind of Rays. Science. 1896;3:227-31.
7. Robb, R.A., Biomedical imaging, visualization, and analysis: Wiley-Liss, Inc.; 2000.
8. Advanced Tomographic Methods in Materials Research and Engineering: Oxford University Press; 2008.
9. Sensen, C.W., Advanced imaging in biology and medicine. Technology, software environments, applications, Springer-Verlag, Berlin-Heidelberg; 2009.
10. Barbetta, A., Bedini, R., Pecci, R., Dentini, M., Role of X-ray microtomography in tissue engineering. Annali dell'Istituto superiore di sanita. 2012;48:10-8.
11. Peyrin, F., Evaluation of bone scaffolds by micro-CT. Osteoporosis international : a journal established as result of cooperation between the European Foundation for Osteoporosis and the National Osteoporosis Foundation of the USA. 2011;22:2043-8.
12. Neldam, C.A., Pinholt, E.M., Synchrotron μCT imaging of bone, titanium implants and bone substitutes - a systematic review of the literature. Journal of cranio-maxillo-facial surgery : official publication of the European Association for Cranio-Maxillo-Facial Surgery. 2014;42:801-5.

# CHAPTER 2

# High-resolution X-ray imaging in biomaterial and tissue engineering research

**Vincent M.J.I. Cuijpers.**

## INTRODUCTION

Tissue engineering is an innovative technique for the regeneration, substitution and augmentation of lost or damaged tissues, with the intention to fully restore tissue function. It is important to study the biocompatibility and functionality of tissue engineered constructs, before their clinical application can be considered. However, tissue engineered constructs are becoming more and more alike the natural tissues, and therefore imaging is often challenging. Multiple imaging techniques are available to obtain biological information from tissue specimens.[1-3] Most commonly, light microscopy and histological analysis are applied to study engineered tissues. However, this method is destructive and allows only for two-dimensional assessments. Moreover, histology does not provide information about the functional status of the engineered tissue. Consequently, non-destructive three-dimensional (3D) quantitative imaging techniques are becoming increasingly relevant for tissue engineering and regenerative medicine approaches.[4,5]

All forms of imaging require the interaction of electromagnetic energy, such as sound waves, magnetism, light, or radiation, with an object (Figure 1). The images are subsequently created by measuring energy changes due to absorption, refraction or scatter resulting from the specific interaction. Consequently, each technique differs in spatial resolution, sensitivity, image acquisition time, tissue penetration depth and imaging costs. Ultrasound imaging, magnetic resonance imaging, nuclear imaging, and radiology imaging are well-developed imaging methods using specific electromagnetic energies. Still, the most commonly applied imaging technique exploits X-rays. Especially X-ray computed tomography (CT) is the main medical imaging method for (bone) tissue engineering research. This review presents X-ray imaging techniques for *ex vivo* and *in vivo* biomaterial and tissue engineering research. X-ray CT and micro-CT imaging are extensively described including specific imaging characteristics, potential applications, strengths and limitations. Also, explicit attention is given

to innovative methods to enhance contrast in micro-CT imaging. First, the application of sophisticated contrast compounds is discussed. Thereafter, refined imaging techniques, such as phase-, fluorescence-, and scatter contrast imaging are explained in detail. Finally, novel advanced hybrid imaging modalities using X-radiation are described.

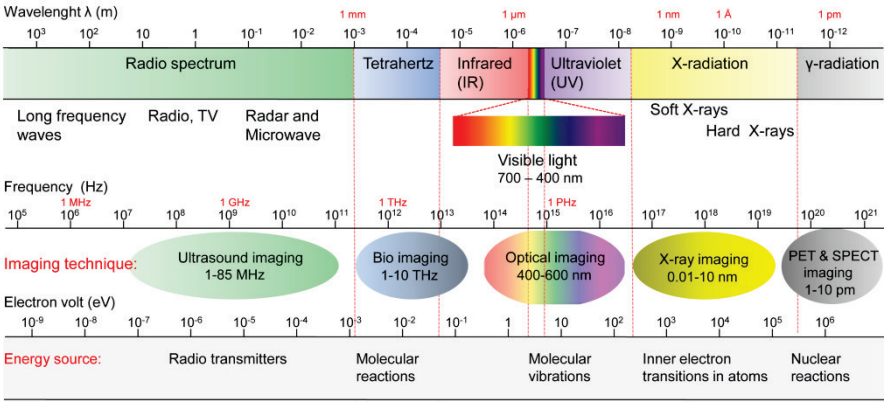


**Figure 1.** An illustration of the electromagnetic spectrum, including wavelength, electron volt, and frequency of imaging techniques including energy source.

## X-RAY IMAGING

X-ray imaging was discovered in 1895 by Wilhelm Conrad Röntgen.[6] X-ray imaging remains the gold standard in bone research, because of the radiopaque characteristics of bone. X-rays contain electromagnetic radiation properties such as phase, polarisation and refraction and reflection through matter. During refraction and reflection from one substance to another, X-radiation induces chemical, optical, thermal and biological effects.

## The generation of X-radiation

X-radiation is consisting of X-rays with a wavelength in the 0.01 to 10 nm range. X-rays can be formed from natural radioactive isotopes, or from artificial sources. The primary methods to generate X-rays are by means of cathode tubes, or by a synchrotron system. Generally, desktop CT systems are using tube-based X-radiation sources.
In the cathode tube (Figure 2A), a stream of electrons is generated, hitting a target material like tungsten at high speed. When these electrons interact with orbital electrons or nucleus of the target surface, they give up a quantity of their energy in the form of electromagnetic energy, known as X-rays.
Synchrotron systems exploit the effects of accelerating subatomic particles through high-powered magnetic fields at speeds near the speed of light. When electrons spiral around a magnetic field at high velocities, they give off radiation in the form of X-rays also, i.e. synchrotron radiation (Figure 2B). Advanced X-ray imaging techniques using synchrotron radiation for the larger part are still in development and subject of research.

## X-ray computed tomography

In traditional radiography no depth information is provided, as all the 3D object structure information is superimposed onto one single 2D image. To overcome this superimposition problem, X-ray computed tomography (CT) was developed.[7] Here, scanning of the object takes place around a trans-axial plane, while scatter of X-rays is minimized by collimating the beam. A full 3D representation of the object is then obtained using digital geometry processing. In this way location and size of the structures of interest are determined. This is done by reconstruction of similar projected cross section images over the object.[8,9] Additionally, the superimposition in CT also enhances the contrast that can be obtained, which is especially useful for observing the soft tissues. The so-called "*direct filtered back-projection*" technique is the most commonly used image reconstruction algorithm

today in CT imaging,[10,11] based on the underlying mathematical principles initially described by J. Radon.[12,13] CT imaging characteristics are extensively reviewed in and thus will not be discussed further.[14-17]

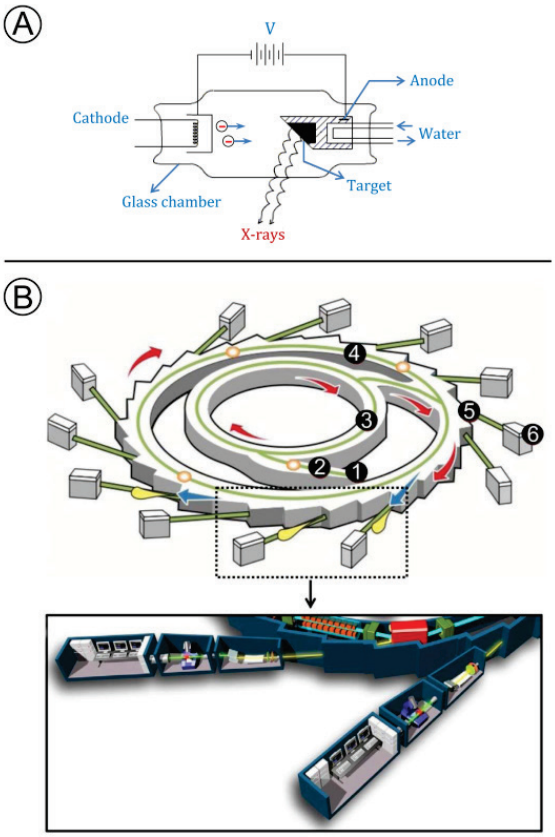


**Figure 2**. X-rays generation using a (A) cathode tube and (B) a synchrotron system. (A) The tube contains the cathode filament which is heated with a low-voltage current, to produce free electrons. The large electrical potential between the cathode and anode induces electrons to be attracted to the anode target. When the stream of high speed electrons interacts with the orbital electrons or the nucleus of the target material, X-radiation is produced. The control console regulates the filament temperature, which corresponds to the intensity of the X-ray output. (B) The synchrotron system accelerates subatomic particles through high-powered magnetic fields at high speed. (1) Electrons are generated inside the electron gun, accelerated using (2) the linear accelerator and exit the accelerator with 100 MeV of energy. (3)

The electrons are transferred to the booster ring, where their energy is boosted using more energy whereby dipole bending electromagnets force the electrons to adopt an almost circular path, before passing into the storage ring. (4) In the storage ring, the circulating electrons are "stored", continuously generating synchrotron light. (5) By bending and curving the path of electrons by magnetic fields, electrons are accelerated and radiate. All generated wavelengths are channelled from the storage ring down by beam-lines, to be utilized for research. Each beam-line includes optical components as different filters and mirrors, to prepare it for use. (6) The beam-line ends in an End Station, where synchrotron radiation interacts with a sample. Hereby, the detector positioned around the sample measures how radiation is transmitted, emitted, scattered or diffracted by the sample. Image (B), courtesy of Australian Synchrotron, Melbourne, Australia.

## MICRO-COMPUTED TOMOGRAPHY

To fulfil the demand for X-ray CT imaging on a more detailed, microscopical level, *ex vivo* and *in vivo* X-ray micro-CT systems were developed. The higher resolution of such systems, compared to conventional CT, is primarily obtained by a greater proximity of the sample to the X-ray source and a smaller spot size of the X-ray source. *Ex vivo* micro-CT systems are suitable for longer irradiation periods, allowing longer image acquisition times. All these differences result in a greatly improved contrast sensitivity and spatial resolution compared to standard CT imaging.[18-23] In the next sections, tube- and synchrotron based X-ray micro-CT systems are described more extensively.

### Tube based X-ray micro-computed tomography

Traditional stand-alone micro-CT systems using tube-based X-radiation are widely used in bone research. Such systems deliver a resolution of 5-10 µm on routine applications. A very common drawback of these systems is that polychromatic X-rays are created. This means that there are high energy rays with low wavelengths as well as lower energy rays with higher wavelengths. All types of X-rays pass through the sample and are subsequently recorded by a detector. It should be noted that the passage through the sample has an influence on the X-ray beam itself and thus on the final image quality,

because passage of the X-rays through a specimen results in easier attenuation of low energy X-ray photons than high energy photons. This is specifically an issue for relatively radiodense materials such as bone, and materials with a high atomic number (e.g. iodine, titanium). It has to be noticed that X-ray beam transmission does not follow the simple exponential decay seen with a monochromatic X-ray. The consequence is "beam hardening", a major disadvantage when using polychromatic X-rays. Due to this effect, further improvement of the image quality is hampered, especially when a sample becomes overly large. Dual energy techniques can to a certain extent correct for the beam hardening effect by using a wide range of high X-ray wavelengths at multiple scans.[24]

Still, sub-micron resolution is definitely possible, especially in *ex vivo* imaging, when smaller samples are used and relatively long exposure times are possible. In nano-CT, the resolution is improved to several hundreds of nanometer. Although, this is unpractical for most applications due to the limited sample size (<$mm^3$).

An additional advantage of the *ex vivo* systems is that the specimen itself is rotating, whilst the X-ray source and detector are in a fixed position, which reduces motion artefacts. In contrast, *in vivo* CT systems show a some lesser resolution due to the restricted exposure time and geometry of the setup, i.e. the X-ray source and detector have to be rotating around the patient or animal. Finally in *in vivo* imaging also necessitates an integrated physiological monitoring subsystem, providing breathing and heart-beat rate information, which is necessary to reduce motion artefacts. Synchronization during imaging, mostly referred to as "gated image acquisition", is often used to reduce blurring in images, as induced by the periodic respiratory and cardiac motions.

### Synchrotron based X-ray micro-computed tomography

Synchrotron micro-CT (SR-micro-CT) systems have multiple advantages over tube-based systems. First, the extraordinary high brilliance of synchrotrons, combined with the continuous spectrum of radiation, allows to select a suitable narrow energy band using a monochromator. Second, the high flux of the radiation allows for short

measuring times and high signal-to-noise ratios at superior spatial resolution. Third, monochromatic synchrotron radiation eliminates any effects of the so-called "beam hardening" artefact, as described above. A fourth and final advantage is that the tuneable synchrotron energy allows for optimal contrast and even for phase contrast research. In view of all these advantages, synchrotron micro-CT is a valuable methodology for biological tissue characterization, from tissue morphology to individual cells. A good example is the work of Zehbe and co-workers, who presented a high spatial resolution of 1.6 µm, using SR-micro-CT imaging of cartilage and bone tissue (Figure 3A,B).[25] Due to optimal image contrast, the segmentation of radio-density differences within the different tissue types became straightforward. Moreover, SR-micro-CT reached a spatial resolution that enabled the topographic representations of the individual cartilage and bone cells residing inside the tissues. In contrast to all these advantages, the shortcoming of synchrotron micro CT is their limited availability.

## Micro-CT analysis of biomaterial scaffolds

Besides the analysis of tissue structures, micro-CT allows for the non-destructive visualization and quantification of the internal structure of scaffold materials, as used in tissue engineering. A wide variety of radiopaque scaffolds can be analyzed, such as ceramics (e.g. hydroxyapatite (HA)), synthetic polymers (e.g. poly lactic-*co*-glycolic acid (PLGA), and poly glycolic acid (PGA)), and natural polymers (e.g. collagen, alginate and chitosan-based substrates).[26-31] Important aspects of scaffold morphology are the porosity, pore characteristics, and interconnectivity.[32,33] Imaging of metal scaffolds however is hampered by scattering of the X-rays at the surface, and impossibility to visualize internal structures within the scaffold.

To characterize injectable CaP cement (CaPC) containing PLGA microparticles, Felix Lanao and co-workers applied *ex vivo* micro-CT prior to use in a *in vivo* biocompatibility study.[34] Their results in Figure 3C illustrate clearly the possibility to visualize the CaPC scaffold, including the pore interconnectivity, in 3D by traditional micro-CT.

However, due to the restrictions of traditional micro-CT imaging, SR-micro-CT is utilized increasingly when sub-micron level imaging is requested.

## Micro-CT analysis in bone tissue research

Due to appropriate radio-absorbance characteristics of bone and teeth, micro-CT is extremely suitable in a broad field of preclinical bone research, as well as for dental applications.[35-37] A good example is the work by Schouten et al., who evaluated the effect of implant design and surface modification on the peri-implant bone response in a femoral defect goat model, using an *ex vivo* desktop micro-CT system, and compared the data with histological analysis of the specimens.[38] Results indicated superior imaging detail of conventional histology over micro-CT. The micro-CT was troubled by the difficulty to discriminate implant material from bone tissue at the implant tissue interface, mainly caused by X-ray scatter of the solid titanium implant. Still, this study confirmed the benefit of 3D bone volume measurements in three different volume zones around the implant (Figure 3D,E) by micro-CT analysis. Therefore, both techniques should not be regarded as competitive or overlapping, but rather be regarded complementary.

Similar findings were reported in large animal model studies. Bobyn and co-workers showed enhanced peri-implant bone volume formation around porous grid-like titanium cylindrical rods in the femur of dogs, treated with bisphosphonate alendronic acid.[39] Also in this report, micro-CT did not provide histological detail to reveal the physical appearance of the bone that was formed in response to the drug. Still, the gross presence or absence of bone could reliably be identified and quantified from the micro-CT images.

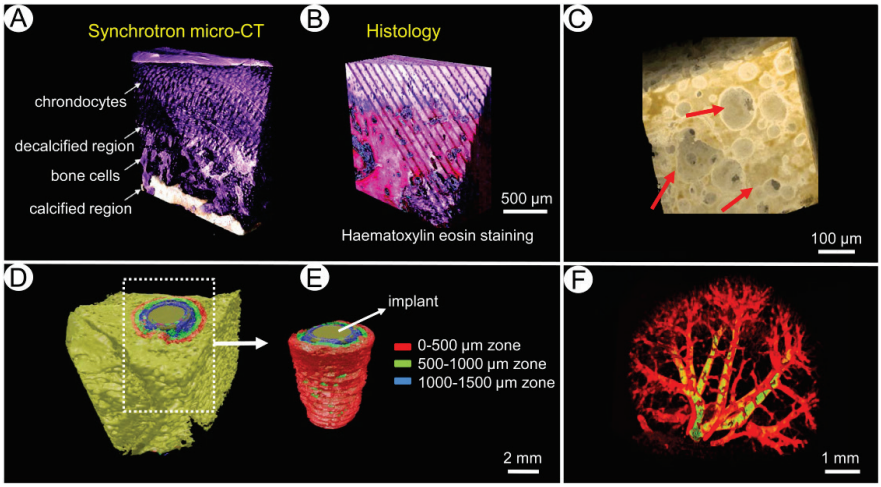


**Figure 3.** Several illustrations of X-ray micro-computed tomography imaging in tissue engineering application. (A) Synchrotron micro-CT (SR-micro-CT) and (B) 3D histology of bone harvested from the joint of a 24-month-old cow, showing similar detail in bone tissue. (C) 3D volume reconstruction (0.5 $mm^3$) of pores (Ø approximately 100 µm) in a calcium-phosphate cement scaffold. Interconnectivity between pores is depicted by red arrows. (D-E) Bench-top micro-CT imaging showing (D) 3D surface reconstruction of bone including a titanium implant and the three bone zones (blue, green and red) surrounding the implant, whereby in (E) bone is made transparent. (F) 3D volume micro-CT reconstruction of perfusion of a mouse kidney using Microfil®, whereby the color-coded structure thickness decreases from yellow to dark-red.

## Micro-CT analysis in bone tissue engineering

Micro-CT is the most frequently applied X-ray imaging technique to characterize and study the application and potential of scaffolds in relation to biological structures in tissue engineering and regenerative medicine.[40-42] First of all, mineralization of cells seeded in scaffolds can be quantified by means of micro-CT.[43-45] Moreover, micro-CT imaging is especially suitable to study the *in vivo* regenerative capacity of bone substitutes,[46-51] e.g. the osteogenic potential of scaffolds with and without bioactive growth factors, such as bone morphogenetic protein-2 (BMP-2), can be studied.[52,53] However, several tissue engineering studies evidence the shortcomings of the micro-CT

technique. One of such studies for instance is the work of Kim and co-workers, who studied the functional enhancement of biphasic CaP (BCaP) cement coated with low-dose BMP-2, in a maxillary sinus model in rabbits.[54] Histological and histomorphometrical analyses proved the bioactivity of this specific cement in *in vitro* experiments. However, micro-CT and histometric analysis failed to confirm such an effect *in vivo*, which was due to the lack of discrimination between cement and native tissue. As a consequence, at the moment a lot of attention is paid to the development of alternative technologies to enhance the contrast in micro-CT imaging to overcome this problem.

## Micro-CT and contrast agents

As illustrated above, micro-CT can be used to study bone formation as well as radiodense (calcified) scaffold materials in 3D, but often fails to discriminate between those materials. In addition, it remains difficult to demonstrate soft tissue components. To overcome the major limitation of radiolucent scaffold (and soft tissue) contrast in *ex vivo* as well as *in vivo* micro-CT applications, contrast agents and comprehensive micro-CT approaches can be applied. The implementation of contrast compounds usually is achieved by perfusion methods and/or impregnation techniques.

Ex-vivo impregnation of soft tissue or radiolucent biomaterial scaffolds with metal-based contrast agents can very well be achieved.[55] Faraj and co-workers introduced micro-CT analysis of two different structurally distinct collagen-based scaffolds, and compared these results with SEM and light microscopy. Optimal contrast was obtained with either a combination of osmium tetroxide and uranyl acetate or a combination of uranyl acetate and lead citrate. The data obtained by micro-CT analysis were in line with those obtained by SEM, yet including additional 3D information. Only the smallest structures (< 10 μm) could not be visualized, due to limited spatial resolution of the micro-CT apparatus.[56]

In *in vivo* studies, barium sulphate-, iodine- and 'heavy element' -based compounds are generally applied as contrast agents in X-ray CT imaging. Figure 3F shows an example of contrast-enhanced micro-CT.

The figure depicts the renal vascular bed within a mouse by using the lead-based compound Microfil®. Usually, the contrast enhancement also improves the reliability of measurements. In this case specifically the blood vessel thickness was visualized color-coded, representing an increase of vessel diameter from yellow to red. However, the same authors underlined a confounding factor in such measurements, i.e. the penetration depth of silicone bead-based contrast agents was limited compared to water-soluble contrast agents. Kerckhofs and co-workers therefore explored an iodine based water-soluble compound to determine the potential of virtual 3D histology and morphometric analysis of subchondral bone and cartilage in mouse knee joints.[57] Unfortunately, results showed that this contrast-enhanced technique could not be used for high resolution *in vivo* micro-CT applications.
Besides penetration depth, there is another main issue in using imaging contrast, i.e. the unavoidable influence that the inclusion of a contrast agent will have on the material properties. This was obvious in a study were tantalum pentoxide ($Ta_2O_5$) was applied as radiopacifier in combination with barium sulphate ($BaSO_4$) in a study monitoring degradation of a self-setting CaP cement in a rabbit femoral condyle model.[58] The results demonstrated that incorporation of either $Ta_2O_5$ or $BaSO_4$, induced no undesirable effects on the biological performance and were applicable to follow cement degradation. Although this seems promising, the inclusion did affect the "handling" problems of the cement, such as an increased setting time. In order to avoid such unwanted side-effects of contrast agents, it can be recommended to focus on more advanced CT techniques, with inherently better discriminative properties.

## ADVANCES IN MICRO-CT IMAGING

New developments in contrast enhancement for micro-CT applications are techniques implementing phase-, scatter- and fluorescence contrast. Conventional (i.e. absorption-based) imaging does not take phase into account, as X-rays of all wavelengths and phases are passing through the samples and only the intensity of the wavelengths is recorded. However, phase contrast (PC), scatter and fluorescence

micro-CT, were specifically developed to exploit the imaging possibilities arising from phase shift or scatter by the object.

## X-ray phase contrast micro-CT

In the quest of better contrast in X-ray imaging, a number of different phase contrast imaging (PCI) techniques have been explored. Unlike absorption-based X-ray CT, X-ray PCI uses the phase shift rather than the absorption as the imaging signal, and therefore provides better image quality in soft tissues and specimens made from low atomic number materials. X-ray PCI techniques are based on the formation and detection of interference patterns between diffracted and un-diffracted waves, resulting in a phase shift. The phase shift is created using several phase contrast mechanisms, such as propagation-based imaging (PBI), analyzer based imaging, interferometry and grating based imaging, which are all described and illustrated in Figure 4 more in detail.[59,60] X-ray PCI modalities have shown promise for a number of biomedical applications, including tissue engineering, owing to their ability to obtain phase-contrast alongside absorption contrast images.

### *Propagation based imaging*

PBI is in many senses the simplest kind of phase contrast imaging, as no optical elements are required in the beam and there is no restriction in the applied X-ray spectrum (Figure 4A). Several research groups have used PBI successful to characterize bone tissue and to study the functionality of scaffolds or constructs in bone tissue engineering.[61]
For instance, a rabbit study using injectable CaP was performed, to directly compare micro-CT and PCI with regards to image quality.[62] Although scaffold materials and mineralized bone were visible using both imaging techniques, only PCI provided high resolution information of the scaffold materials, bone in-growth, and vessel network.

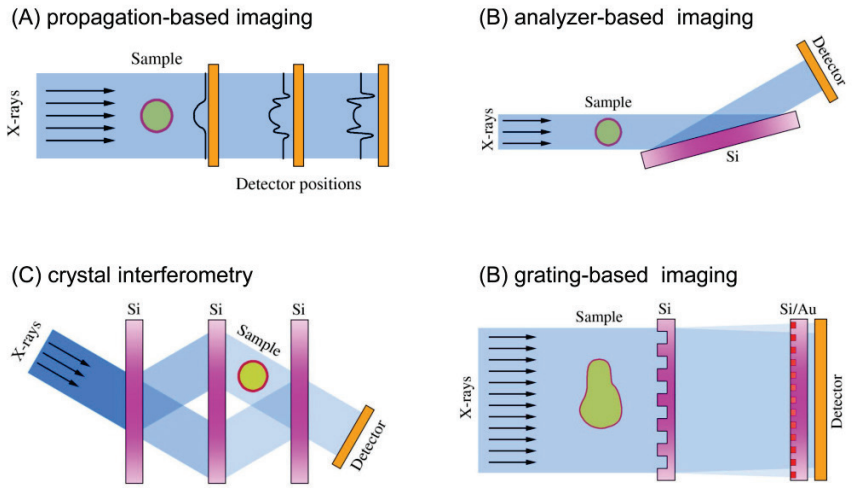


**Figure 4.** Schematic drawing of the phase contrast mechanisms in (A) propagation based imaging (PBI), (B) analyzer based imaging (ABI), (C) crystal interferometry, and (D) grating based imaging (GBI). PBI relies on interference fringes arising in the free space propagation as illustrated in (A). In order to achieve interference of the propagating beam, a very high degree of spatial coherence is required, and a high resolution detector is needed to observe the fringes. A series of images is then recorded at different propagation distances in order to unambiguously determine the phase of the wave front. In (B) ABI, the first derivative of the phase front is measured by detecting refraction angles. This method uses a single or a double crystal as a collimator, to produce a parallel beam (not shown in the figure). The parallel beam penetrates the sample and is then analyzed by a second crystal that reflects the beam onto a detector. The incidence angle of the analyzer crystal can be slightly detuned so that the refracted part of the beam is reflected onto the detector. When the angular detuning is varied, different refraction angles are analyzed from several positions, from which a full data set and the final image is formed. (C) A crystal interferometer is based on three silicon beam splitters that split, redirect and recombine the X-ray beam. A sample is placed in one beam path, and when the split beam is recombined, the phase shift induced by the sample will produce an interference pattern from which the phase shift can be extracted. The beam quality requirements are not very strict, but the silicon crystals act as monochromator selecting a narrow spectral width. Hence a very intense beam is required to reduce exposure time. (D) GBI is related to CI, it consists of a beam splitter and a beam analyzer, and GBI, whereby the first derivative of the phase front is measured. The beam splitter grating splits the beam by diffraction, but the diffraction orders are separated by less than a milli-radian, and the diffracted beams are hence not spatially separated, but will interfere to create an intensity pattern downstream of the beam-splitter at a distance. Refraction in a sample is measured by detecting the transverse shift of the interference pattern with a high resolution detector or an analyzer grating. Images courtesy of Bech et al.[60]

The reported PCI results were consistent with conventional 2D histomorphometric analysis, but at the same time the authors noticed the limited sample size (<0,25 $mm^3$) necessary to reach such high spatial resolution.

### *Analyzer based imaging*

A second approach is analyzer-based imaging (ABI), also called diffraction-enhanced imaging (DEI). A single or double crystal is used to create a phase shift of X-rays (Figure 4B). Several researchers have used ABI in tissue engineering applications, due to its high phase sensitivity, scatter rejection and the ability to separate absorption- and refraction contrast. However, imaging is only possible in the direction perpendicular to the analyzer crystal. Nonetheless, Sun et al. successfully applied ABI to characterize the repair of osteonecrosis in rabbits using a nano-hydroxyapatite/collagen scaffold combined with autologous mesemchymal stem cells.[63] The ABI technique allowed for identification of the biomaterial-host interface, bone tissue formation, and substitution of biomaterials with newly grown tissues, over a period of 12 weeks, at 10 µm resolution. In addition, other researchers found that ABI has significant gains in both resolution and contrast-to-noise-ratio (CNR) over synchrotron radiation imaging.[64] In a follow-up study, the same researchers reported an increased contrast for the titanium-bone interface, when ABI was compared to micro-CT imaging. Especially, scatter of the titanium pins implanted into bone defects was considerably reduced, which was not the case when using conventional micro-CT.[65]

### *X-ray interferometry imaging*

A third technique to obtain phase contrast imaging is crystal interferometry (CI), based on silicon beam splitters that split, redirect and recombine an X-ray beam, resulting in phase contrast, as is illustrated in Figure 4C. CI imaging shows a very high phase sensitivity and can be used to image extremely radiolucent biomaterial scaffolds.

For instance, Momose et al. demonstrated discrimination of polystyrene (PS) and polymethyl methacrylate (PMMA) polymers, within a cylindrically shaped (Ø 2mm) sample, based on their refracted indices.[66] Such material is not discernible in conventional CT imaging. Also, the achieved contrast resolution in this study (4.13 µm) was clearly beyond what could normally be obtained with absorption-based micro-CT. However, an interferometer is very sensitive to mechanical instabilities. Therefore, CI is only suited for high-resolution *ex vivo* imaging at synchrotron sources where the requirement of high beam intensity is met. Besides, in *in vivo* applications the body heat radiated from animal models can interfere with interferometry. Additionally, this method is unsuitable for objects with extremely sharp soft-hard tissue structural boundaries with a large refractive index difference, such as the bone-cartilage interface or implant-host interface. Taken all these disadvantages together, the use of CI is at this moment less applicable in bone tissue engineering.

### *Grating based imaging*

Grating based imaging (GBI) is a fourth approach based on phase contrast imaging. GBI is related to crystal interferometry and consists of a beam splitter and a beam analyser. GBI is related to ABI by the fact that the first derivative of the phase front is measured (Figure 4D). GBI has been applied in the past in visible light phase contrast imaging and has recently been used in X-ray imaging as well.
As in interferometry, GBI can be used to study a broad range of biomaterials with a relatively low refractive index *ex vivo.* Using GBI, Takashima and co-workers were able to visualize the microstructure and degradation profile of implanted biodegradable PGA fibres, with a fibre Ø of 10 µm.[67] They demonstrated that GBI can be used to visualize soft tissue with a large field-of-view (23.4 mm (H) x 15.4 mm (V)) and at high spatial resolution (11.7 µm pixel size).

Based on the above description, it can be conclude that depending on which of the four above described modalities is used, phase contrast

imaging may be an ideal technique to obtain highly detailed qualitative and quantitative characterisation of both radiopaque (hard) and radiolucent (soft) tissues. Furthermore, PCI contrast resolution is many orders of magnitude higher than absorption contrast. It is also possible to combine PCI with X-ray absorption contrast and/or scatter contrast, as will be described in the next paragraph.

### X-ray scatter contrast micro-CT

Scatter X-radiation is a type of secondary radiation that occurs when X-rays intercept any object, interact with electrons and atoms, and causing a number of X-rays to be generated in random directions. Such scatter normally is an undesirable side-effect in X-ray imaging, but can also be functionalized as an alternative application to X-ray absorption imaging. The term X-ray scattering refers to a group of techniques including (ultra) small-angle X-ray scattering ((U)SAXS), wide-angle X-ray scattering (WAXS) and X-ray reflectivity. Although seldom used in bone tissue engineering, scatter micro-CT is an ideal approach to study for instance polymer texture. Appel et al. compared the use of X-ray absorption contrast-, propagation-based phase contrast-, and USAXS imaging to image two types of scaffolds, i.e. PLGA and a PLLA-Fibrin mesh (Figure 5).[68] PLGA scaffolds in cell culture conditions generated contrast in especially PBI and USAXS imaging, allowing 3D assessment of the pore volume and scaffold wall. Furthermore, when these scaffolds were implanted in a critical-sized (Ø 8 mm) rat cranial bone defect, the combination of the diverse imaging modalities allowed for segmentation of soft tissue, newly formed bone within the cranial defect and residual polymer scaffold (Figure 5F). This was not possible with conventional micro-CT. These results prove that also scatter contrast imaging is a valuable and complementary technique to study tissue engineered structures. However, the use of a synchrotron light source again limits the broad application of this method.

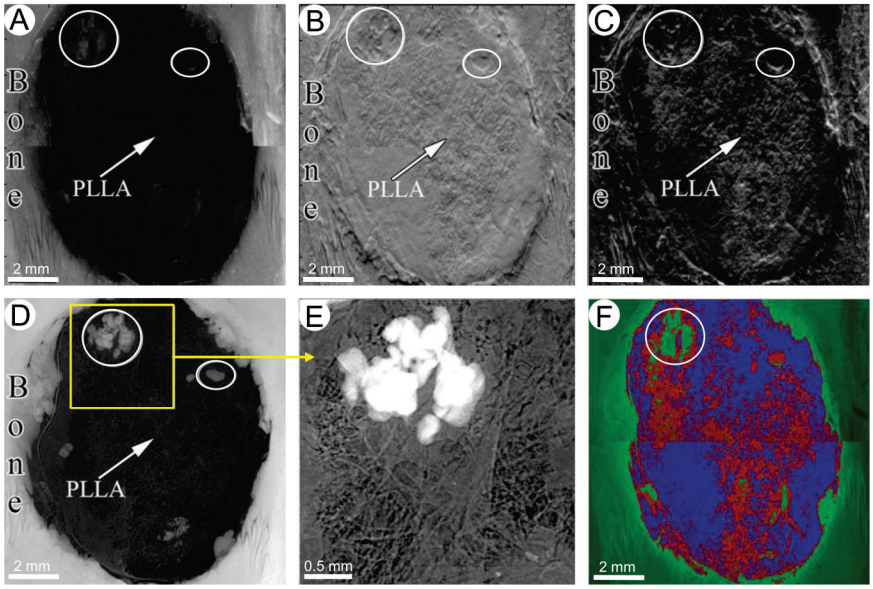


**Figure 5.** X-ray micro-computed tomography imaging in tissue engineering application. (A) absorption contrast-, (B) propagation-based phase contrast- (PBI), and (C) ultra-small-angle-X-ray-scatter (USAXS) imaging, using synchrotron radiation, of a rat cranial defect sample with a poly(L-lactic acid)(PLLA) - fibrin scaffold. (D) Combined absorption-, and phase contrast image, illustrating newly formed bone region (circles), while the PLLA scaffold (arrow) is especially visible in phase contrast- and scatter images (B,C). (E) The magnified region of newly formed bone and PLLA fibres from inset (yellow box). (F) Segmented merged image indicating separate identification of regions of bone (green), PLLA /Fibrin scaffold (red), and soft tissue (blue). Image adapted from Appel et al.[68]

## X-ray fluorescence contrast

Although the term "fluorescence" is well known in light microscopy, it can also be applied to X-rays. The term fluorescence then describes the phenomenon in which the absorption of X-radiation of a specific energy, results in the re-emission of X-radiation of a different energy.

Thus, X-ray fluorescence (XRF) is the emission of characteristic secondary X-rays from a material that has been excited by bombarding with high-energy X-rays. The in this way obtained X-ray fluorescence can be used for functional imaging or to provide molecular information. As the secondary X-rays also allow for non-destructive chemical mapping, this permits the co-registration of 3D micro-morphology and 3D chemical composition. XRF has been used to study moderately X-ray transparent (soft) tissues,[69] but the use of XRF to study bone tissue has also been initiated. In a study on osteoporosis in a rat model, the strontium (Sr) distribution received from a daily dose of Sr-containing drugs, was evaluated and co-registered with a micro-CT absorption contrast image (Figure 6). Despite such new developments in X-ray imaging, also here, spatial resolution was very much restricted compared to more common imaging modalities, such as optical imaging.

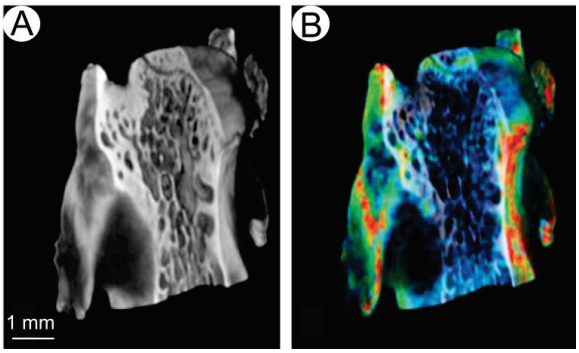


**Figure 6.** Micro-X-ray fluorescence (micro-XRF) imaging in tissue engineering applications. 3D volume rendered micro-CT image (A) and a fused micro-CT – micro-XRF image (B) of a vertebra of an osteoporotic rat which received a daily dose of strontium-containing drugs. The front cover quarter is virtually removed to show the internal microstructure and concentration distribution. The strontium concentration is displayed color-coded in a blue-red scale whereby the highest uptake is indicated in red. Image courtesy of Bruker-Skyscan, Belgium.

## COMPLEMENTARY TECHNIQUES TO X-RAY IMAGING

Finally, it is evident from all above-described applications, that solitary imaging techniques each have their respective pros and cons. Therefore, distinct imaging techniques should be regarded as being complementary, rather than competitive. A main challenge remains to achieve multi-modal imaging, to simultaneously obtain molecular, functional and anatomical information. Therefore, also other imaging techniques than X-ray imaging have to be considered. Magnetic resonance imaging (MRI) has recently made great advances towards bone imaging. Also nuclear imaging (NI) modalities are already frequently used in bone research.[70-74] NI techniques are mostly performed in hybrid imaging machinery combined with X-ray CT.

### Magnetic resonance imaging in bone research

In MRI, a powerful magnet is used to align the nuclei of the atoms inside an object. When the magnet is shut off, nuclei fall back in their original state, which can be recorded after a certain time interval, the so-called echo time. As hydrogen is the smallest atom, it is most easily exited, and thus the image contrast in MRI is typically related to differences in the proton density/water content of the object. Soft tissues therefore are simply detected by conventional MRI, whereas MRI of bone or bone substitutes is cumbersome due to the low water content. Still, also in bone contrast can be generated, when the measurement is performed with an ultra-short echo time (UTE). In practice, data acquisition in UTE is often is suffering from image distortions. Therefore, more recently zero-time-to-echo (ZTE) imaging has been introduced. ZTE resulted in the best MRI contrast for bone so far. For that reason, Sun et al. applied ZTE to study a contrast-agent-enhanced CaP bone filler in bone tissue.[75] The technique allowed to discriminate the bone substitute as well as bone tissue, which was not possible when applying *in vivo* micro-CT. However, it has to be noticed that there are also limitations associated with the use of contrast agents, like long acquisition time, toxicity risks, artifacts and background noise.[76] Therefore, it has been proposed to perform MRI

imaging not based on just a proton signal, but based on heteronuclear nuclei (i.e. $^{19}F$, $^{13}C$, $^{23}Na$, $^{31}P$). Since the element Fluorine does not normally appear in the body (outside the enamel), especially $^{19}F$-based contrast agents (e.g. perfluorocarbons) are investigated in ZTE, in *in vivo* studies on bone biomaterials.[77]
Still, it is important to emphasize that the spatial resolution of micro-MRI remains is approximately ten times lower compared to the micro-equivalent of radiology. Other drawbacks are the high equipment cost of the complex technology, a relatively low signal-to-noise, and the lesser ability to threshold based on image contrast.

### X-ray CT combined with nuclear imaging

In nuclear imaging (NI), positrons or gamma-rays (γ-rays) are identified when emitted from radiopharmaceuticals (radiotracers) incorporated in cells and tissues. The most common forms of NI techniques are positron emission tomography (PET) and single-photon emission computed tomography (SPECT). Both are non-invasive imaging techniques, with no limitation on tissue penetration depth and capable of relaying functional tissue information in clinical applications. Both are successfully applicable in pre-clinical (*in vivo*) animal studies, as well as in tissue engineering research.

#### *X-ray CT combined with positron emission tomography*

In PET imaging, tracers such as Oxygen-15 ($^{15}O$), Carbon-11 ($^{11}C$), Fluorine-18 ($^{18}F$) and Iodine 124 ($^{124}I$)), are attached to biologically active molecules and thereafter introduced into the body. The positrons that are emitted from the tracer are measured, and are relative to the concentration of the radio-tracer. Thus, the measurements are indicative for tissue metabolic activity. Radio-tracers, such as $^{18}F$-NaF, are incorporated into bone and thus valuable for bone tissue engineering research. As an example, Ventura and co-workers monitored BMP-2-release from a porous CaPC scaffold in a rat calvarial model by PET using $^{18}F$.[78] The PET imaging demonstrated

enhanced activity (i.e. increased bone formation) when BMP-2 was applied. The improved bone formation was confirmed in retrospect using micro-CT and histomorphometric analyses (Figure 7A, B).
The main disadvantages of PET imaging are the dependence on an onsite (or close by) cyclotron to produce radioisotopes, due to the relatively short half-life of most used isotopes. Also, the complex chemistry associated with incorporation of the tracer into a molecules of interest, limits the use of very complex tracers.
Gallium 68 ($^{68}$Ga) is a positron emitter, which can be produced independent of a cyclotron by a so-called $^{68}$Germanium/$^{68}$Gallium generator. Therefore, $^{68}$Ga-labelled bone imaging agents are currently the object of extensive preclinical research. Independent of the application, nearly all current day PET set-ups are combined with micro-CT in one hybrid machine.

### *X-ray CT combined with single-photon emission computed tomography*

Also single-photon emission computed tomography (SPECT) tracers are biomolecules, which are linked to isotopes. After administration to the body, the isotopes decay, while producing γ-rays, which can be detected in the SPECT apparatus. The main (pre)clinically employed tracers are Technetium-99m ($^{99m}$Tc), Indium ($^{111}$In) and Iodine isotopes ($^{123}$I, $^{131}$I, $^{125}$I). These isotopes generally have relatively long half-lives (6h for $^{99m}$Tc up to 60 days for $^{125}$I), which allow for longitudinal studies. Compared to PET, SPECT is less sensitive, yet the spatial resolution is higher (1-2 mm vs. <1 mm). Also, multiple SPECT tracers can be applied simultaneously, which offers the possibility to widen the observational time window of several hours to days after administration of the labelled compounds.

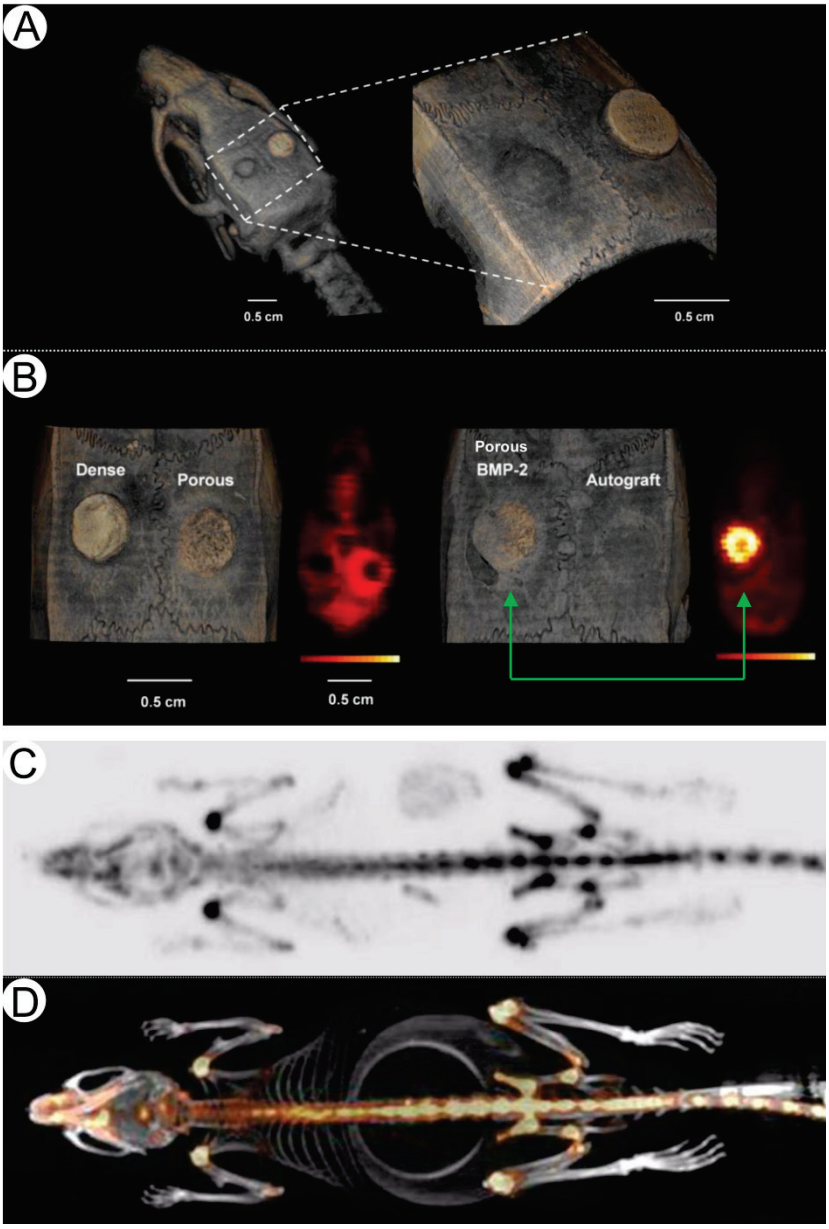


**Figure 7.** Micro-CT combined with nuclear imaging. (A-B) Positron emission tomography (PET) and (C-D) single-photon emission computed tomography (SPECT) imaging combined with X-ray CT. (A-B) PET and X-ray CT imaging of calvarial rat model. (A) 3D reconstruction of CT scans, the right side shows a micro-CT close-up at

2 weeks post-surgery. Both the autograft (left) and the dense CaPC (right) are easily recognizable. (B) Representative micro-CT of four experimental groups (dense, porous, porous-BMP-2 and autograft) 4 weeks post-implantation and corresponding 18F-Fluoride PET uptake. Note (green arrow) that the BMP-2 loaded sample visually gives the highest signal whereas the autograft is lowest. Figures adapted from Ventura et al.[78] (C-D) SPECT imaging, acquired 3h post-injection of $^{99m}$Tc-MDP demonstrating *in vivo* bone imaging in C57BL/6 mouse. (C) Full body SPECT sagittal image, to detect the high MDP uptake within the skeleton with high uptakes in joints (knee, shoulders, hip), spine and in the skull. (D) Micro-SPECT/CT coronal 3D image of the animal showing the MDP uptake; note the high spatial resolution of the CT acquisition to localize the main areas of $^{99m}$Tc-MDP uptake, showing the high uptake (yellow-brown) of the tracer in respectively the skull and shoulder-, hip-, and knee joints. Image adapted from Tremoleda et al.[79]

In bone imaging, diphosphonate compounds are frequently applied due to their affinity to calcium ions. For example, Tremoleda and co-workers have successfully reported the use of $^{99m}$Tc-methylene diphosphonate (MDP) to detect changes in bone turnover and cartilage composition in an osteoarthritis induced rodent model.[79] The co-registration of micro-SPECT and micro-CT images, allows the detection of high $^{99m}$Tc-MDP uptake, depicting areas of high bone turnover, as shown in Figure 7C,D. As in PET imaging, SPECT allows for dynamic image acquisition of the whole-body, whereby CT is functional for anatomical localization of the entire skeleton. Thus, CT is a complementary imaging technique to SPECT and usually present within the same machinery.

## Advances in hybrid X-ray imaging

Also, the combined use of PET and SPECT tracers has been investigated. The aim of such studies is the dual administration of labeled biomolecules, which then can be measured simultaneously.[80] However, such an approach was proven problematic due to "cross-talk", i.e. the PET emission generates noise in the SPECT results.[81] Still, Chapman et al. presented an optimized protocol for sequential tri-modal SPECT/CT/PET *in vivo* imaging with SPECT ($^{99m}$Tc-MMA or $^{99m}$Tc-pentetate) and PET ($Na^{18}F$) probes in a mouse (Figure 8).[82] The SPECT tracers showed distinctive accumulation in the respiratory and urinary system. Subsequent CT imaging visualized the complete anatomical skeleton. Thereafter, injection with $Na^{18}F$ presented clearly characteristic bone activity in PET imaging. The sequence of imaging, calibration of both imaging modalities, and especially the discrimination of emission of multiple isotopes in SPECT and PET, were found very critical, which limits the practical application of such a technique in a wider context.

Besides improvement in multimodal imaging techniques, there are also new developments in synchrotron X-ray sources. For example, a compact stand-alone laser-driven synchrotron light source has been used to create very bright monochromatic light by Eggl et al.[83] They presented this technique to produce different phase contrast images by applying interferometry, grating-based- and attenuation imaging simultaneously. Soft as well as hard tissues and organs of a mouse were presented in detail at sub-micron resolution, which normally is only possible with traditional synchrotron imaging systems.

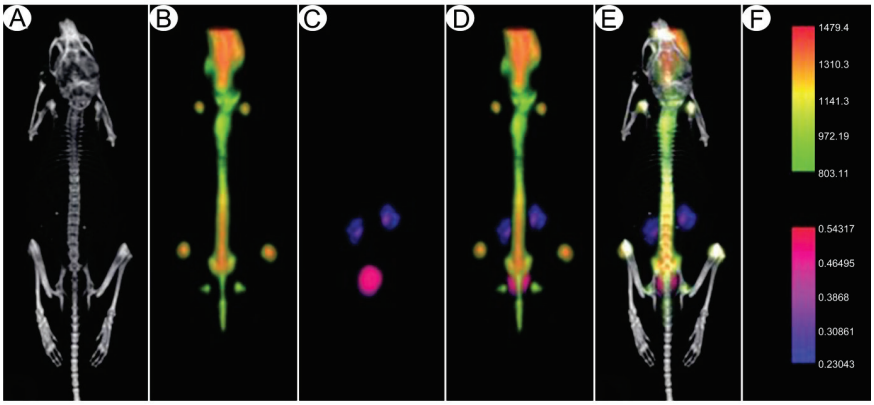


**Figure 8.** Hybrid X-ray imaging. Representative results of dual *in vivo* $Na^{18}F$ and $^{99m}Tc$-Penetate tracer imaging showing individual modality display. (A) CT image for anatomical reference, (B) $Na^{18}F$ showed characteristic bone-labeling activity in PET imaging, (C) $^{99m}Tc$-pentetate showing characteristic accumulation in the urinary system in SPECT imaging, (D) a merged dual modality PET/SPECT display, and (E) a merged tri-modal PET/SPECT/CT display. Unit scale bars for PET (kBq/cc) and SPECT (cps/voxel, voxel size = 250 µm isotropic) are presented in the top and bottom half of frame (F), respectively. Image adapted from Chapman et al.[82]

## CONCLUSION

Tissue engineered constructs more and more become alike the natural tissues they intend to restore. Hence, routine imaging techniques often fall short in characterization, and to determine proper construct placing, and performance over time. The ability to monitor and assess tissue engineering approaches in medicine is a critical need. The imaging techniques described here have successfully been applied to evaluate many specific aspects of bone tissue engineering. However, the ideal technique depends largely on the specifics of the application and the research question. X-ray imaging modalities, including hybrid techniques, show promise for especially *in vivo* purposes due to the spatial resolution and imaging depth capabilities. As advances in each modality are made to improve these capabilities, their applications towards the characterization of structure and function of scaffolds and

engineered tissues will expand. Potentially, the most useful upcoming advances in imaging include the whole range of X-ray phase contrast techniques and the development of bone specific tracers and contrast agents to serve as biomarkers. Finally, in many cases the application of multiple imaging modalities is likely to improve the quality of analysis as it does already for many clinical applications. It is essential that researchers continue to investigate and optimize these imaging modalities as assessment tools and move away from traditional two-dimensional methods so the transition to the clinical setting can be reliable, efficient and accelerated.

Nonetheless, nano-resolution multi-modal *in vivo* imaging within the same species, providing a multi-dimensioned view into associated molecular, functional, and anatomical changes, will remain a challenge for the future.

## REFERENCES


1. Kherlopian, A.R., Song, T., Duan, Q., Neimark, M.A., Po, M.J., Gohagan, J.K., et al. A review of imaging techniques for systems biology. BMC systems biology. 2008;2:74.
2. Smith, L.E., Smallwood, R., Macneil, S., A comparison of imaging methodologies for 3D tissue engineering. Microscopy research and technique. 2010;73:1123-33.
3. Guldberg, R.E., Duvall, C.L., Peister, A., Oest, M.E., Lin, A.S., Palmer, A.W., et al. 3D imaging of tissue integration with porous biomaterials. Biomaterials. 2008;29:3757-61.
4. Appel, A.A., Anastasio, M.A., Larson, J.C., Brey, E.M., Imaging challenges in biomaterials and tissue engineering. Biomaterials. 2013;34:6615-30.
5. Ventura, M., Boerman, O.C., Korte de, C., Rijpkema, M., Heerschap, A., Oosterwijk, E., et al. Preclinical imaging in bone tissue engineering. Tissue engineering Part B, Reviews. 2014;20:578-95.
6. Rontgen, W.C., On a New Kind of Rays. Science. 1896;3:227-31.
7. Hounsfield, G.N., Computerized transverse axial scanning (tomography). 1. Description of system. The British journal of radiology. 1973;46:1016-22.
8. Kalender, W.A., X-ray computed tomography. Phys Med Biol. 2006;51:R29-R43.
9. Fleischmann, D., Boas, F.E., Computed tomography-old ideas and new technology. Eur Radiol. 2011;21:510-7.
10. Pelc, N.J., Chesler, D.A., Utilization of Cross-Plane Rays for 3-Dimensional Reconstruction by Filtered Back-Projection. Journal of computer assisted tomography. 1979;3:385-95.
11. Claus, B.E.H., Eberhard, J.W., Schmitz, A., Carson, P., Goodsitt, M., Chan, H.P., Generalized filtered back-projection reconstruction in breast tomosynthesis. Lect Notes Comput Sc. 2006;4046:167-74.
12. Radon, Johann (1917), "Über die Bestimmung von Funktionen durch ihre Integralwerte längs gewisser Mannigfaltigkeiten", Berichte über die Verhandlungen der Königlich-Sächsischen Akademie der Wissenschaften zu Leipzig, Mathematisch-Physische Klasse [Reports on the proceedings of the Royal Saxonian Academy of Sciences at Leipzig, mathematical and physical section] (Leipzig: Teubner) (69): 262–277.
13. Radon, J., On the Determination of Functions from Their Integral Values along Certain Manifolds. IEEE transactions on medical imaging. 1986;5:170-6.
14. Adams, J.E., Quantitative computed tomography. Eur J Radiol. 2009;71:415-24.

15. Hatcher, D.C., Operational principles for cone-beam computed tomography. J Am Dent Assoc. 2010;141:3S-6S.
16. Wang, G., Yu, H.Y., De Man, B.. An outlook on X-ray CT research and development. Med Phys. 2008;35:1051-64.
17. Feldkamp, L.A., Davis, L.C., Kress JW. Practical Cone-Beam Algorithm. J Opt Soc Am A. 1984;1:612-9.
18. Elliott, J.C., Dover, S.D., X-ray microtomography. Journal of microscopy. 1982;126:211-3.
19. Morton, E.J., Webb, S., Bateman, J.E., Clarke, L.J., Shelton, C.G., 3-Dimensional X-Ray Microtomography for Medical and Biological Applications. Phys Med Biol. 1990;35:805-20.
20. Flannery, B.P., Deckman, H.W., Roberge, W.G., Damico, K.L., 3-Dimensional X-Ray Microtomography. Science. 1987;237:1439-44.
21. Bouxsein, M.L., Boyd, S.K., Christiansen, B.A., Guldberg, R.E., Jepsen, K.J., Muller, R., Guidelines for Assessment of Bone Microstructure in Rodents Using Micro-Computed Tomography. Journal of Bone and Mineral Research. 2010;25:1468-86.
22. Draenert, M.E., Draenert, A.I., Forriol, F., Erler, M., Kunzelmann, K.H., Hickel, R., et al. Value and limits of mu-CT for nondemineralized bone tissue processing. Microscopy research and technique. 2012;75:416-24.
23. Clark, D.P., Badea, C.T., Micro-CT of rodents: State-of-the-art and future perspectives. Phys Medica. 2014;30:619-34.
24. Granton, P.V., Pollmann, S.I., Ford, N.L., Drangova, M., Holdsworth, D.W., Implementation of dual- and triple-energy cone-beam micro-CT for postreconstruction material decomposition. Medical physics. 2008;35:5030-42.
25. Zehbe, R., Haibel, A., Riesemeier, H., Gross, U., Kirkpatrick, C.J., Schubert, H., et al. Going beyond histology. Synchrotron micro-computed tomography as a methodology for biological tissue characterization: from tissue morphology to individual cells. Journal of the Royal Society, Interface / the Royal Society. 2010;7:49-59.
26. Teraoka, K., Kato, T., Hattori, K., Ohgushi, H., Evaluation of the capacity of mosaic-like porous ceramics with designed pores to support osteoconduction. J Biomed Mater Res A. 2013;101:3571-9.
27. Park, S.A., Lee, S.H., Kim, W.D., Fabrication of porous polycaprolactone /hydroxyapatite (PCL/HA) blend scaffolds using a 3D plotting system for bone tissue engineering. Bioprocess and biosystems engineering. 2011;34:505-13.
28. Peng, F., Yu, X.H., Wei, M., *In vitro* cell performance on hydroxyapatite particles/poly(L-lactic acid) nanofibrous scaffolds with an excellent particle along nanofiber orientation. Acta Biomater. 2011;7:2585-92.

29. Laurent, C.P., Latil, P., Durville, D., Rahouadj, R., Geindreau, C., Orgeas, L., et al. Mechanical behaviour of a fibrous scaffold for ligament tissue engineering: Finite elements analysis vs. X-ray tomography imaging. Journal of the mechanical behavior of biomedical materials. 2014;40C:222-33.
30. Melchels, F.P., Barradas, A.M., Blitterswijk van, C.A., Boer de, J., Feijen, J., Grijpma, D.W., Effects of the architecture of tissue engineering scaffolds on cell seeding and culturing. Acta Biomater. 2010;6:4208-17.
31. Kuboyama, N., Kiba, H., Arai, K., Uchida, R., Tanimoto, Y., Bhawal, U.K., et al. Silk fibroin-based scaffolds for bone regeneration. J Biomed Mater Res B. 2013;101B:295-302.
32. Petrie Aronin, C.E., Sadik, K.W., Lay, A.L., Rion, D.B., Tholpady, S.S., Ogle, R.C., et al. Comparative effects of scaffold pore size, pore volume, and total void volume on cranial bone healing patterns using microsphere-based scaffolds. J Biomed Mater Res A. 2009;89:632-41.
33. Giuliani, A., Moroncini, F., Mazzoni, S., Belicchi, M.L., Villa, C., Erratico, S., et al. Polyglycolic acid-polylactic acid scaffold response to different progenitor cell *in vitro* cultures: a demonstrative and comparative X-ray synchrotron radiation phase-contrast microtomography study. Tissue engineering Part C, Methods. 2014;20:308-16.
34. Liao, H., Felix Lanao, R.P., Beucken van den, J.J., Zhou, N., Both, S.K., Wolke, J.G., et al. Size matters: effects of PLGA-microsphere size in injectable CPC/PLGA on bone formation. J Tissue Eng Regen Med. 2013.
35. Barbe, M.F., Adiga, R., Gordiienko, O., Pleshko, N., Selzer, M.E., Krynska, B., Micro-computed tomography assessment of vertebral column defects in retinoic acid-induced rat model of myelomeningocele. Birth defects research Part A, Clinical and molecular teratology. 2014;100:453-62.
36. Korbmacher, H., Schilling, A., Puschel, K., Amling, M., Kahl-Nieke, B., Age-dependent three-dimen\sional micro-computed tomography analysis of the human midpalatal suture. J Orofac Orthop. 2007;68:364-76.
37. Huang, C.C., Chang, Y.C., Chuang, M,C., Lin, H.J., Tsai, Y.L., Chang, S.H., et al. Analysis of the Width of Vertical Root Fracture in Endodontically Treated Teeth by 2 Micro-Computed Tomography Systems. J Endodont. 2014;40:698-702.
38. Schouten, C., Meijer, G.J., Beucken van den, J.J., Spauwen, P.H., Jansen, J.A., The quantitative assessment of peri-implant bone responses using histomorphometry and micro-computed tomography. Biomaterials. 2009;30:4539-49.

39. Bobyn, J.D., Thompson, R., Lim, L., Pura, J.A., Bobyn, K., Tanzer, M., Local Alendronic Acid Elution Increases Net Periimplant Bone Formation: A Micro-CT Analysis. Clin Orthop Relat R. 2014;472:687-94.
40. Alghamdi, H.S., Beucken van den, J.J., Jansen, J.A., Osteoporotic rat models for evaluation of osseointegration of bone implants. Tissue engineering Part C, Methods. 2014;20:493-505.
41. Barbetta, A., Bedini, R., Pecci, R., Dentini, M., Role of X-ray microtomography in tissue engineering. Annali Dell Istituto Superiore Di Sanita. 2012;48:10-8.
42. Cleynenbreugel van, T., Schrooten, J., Oosterwyck van, H., Sloten, J.V., Micro-CT-based screening of biomechanical and structural properties of bone tissue engineering scaffolds. Medical & Biological Engineering & Computing. 2006;44:517-25.
43. Cartmell, S., Huynh, K., Lin, A., Nagaraja, S., Guldberg, R., Quantitative microcomputed tomography analysis of mineralization within three-dimensional scaffolds *in vitro*. J Biomed Mater Res A. 2004;69A:97-104.
44. Panzavolta, S., Torricelli, P., Amadori, S., Parrilli, A., Rubini, K., Bella della, E., et al. 3D interconnected porous biomimetic scaffolds: *In vitro* cell response. J Biomed Mater Res A. 2013;101:3560-70.
45. Papantoniou, I., Sonnaert, M., Geris, L., Luyten, F.P., Schrooten, J., Kerckhofs, G., Three-Dimensional Characterization of Tissue-Engineered Constructs by Contrast-Enhanced Nanofocus Computed Tomography. Tissue Eng Part C-Me. 2014;20:177-87.
46. Watering van de, F.C.J, Beucken van den, J.J.J.P., Walboomers, X.F., Jansen, J.A., Calcium phosphate/poly(D,L-lactic-co-glycolic acid) composite bone substitute materials: evaluation of temporal degradation and bone ingrowth in a rat critical-sized cranial defect. Clin Oral Implan Res. 2012;23:151-9.
47. Chappard, C., Bensalah, S., Olivier, C., Gouttenoire, P.J., Marchadier, A., Benhamou, C., et al. 3D characterization of pores in the cortical bone of human femur in the elderly at different locations as determined by synchrotron micro-computed tomography images. Osteoporosis international : a journal established as result of cooperation between the European Foundation for Osteoporosis and the National Osteoporosis Foundation of the USA. 2013;24:1023-33.
48. Britz, H.M., Jokihaara, J., Leppanen, O.V., Jarvinen, T., Cooper, D.M.L., 3D visualization and quantification of rat cortical bone porosity using a desktop micro-CT system: a case study in the tibia. Journal of microscopy. 2010;240:32-7.
49. Meleo, D., Bedini, R., Pecci, R., Mangione, F., Pacifici, L., Micro-tomographic and morphometric characterization of a bioceramic

bone substitute in dental implantology. Ann I Super Sanita. 2012; 48:59-64.

50. Komlev, V.S., Mastrogiacomo, M., Pereira, R.C., Peyrin, F., Rustichelli, F., Cancedda, R., Biodegradation of Porous Calcium Phosphate Scaffolds in an Ectopic Bone Formation Model Studied by X-Ray Computed Microtomography. Eur Cells Mater. 2010;19:136-46.
51. McLaren, J.S., White, L.J., Cox, H.C., Ashraf, W., Rahman, C.V., Blunn, G.W., et al. Biodegradable Antibiotic-Impregnated Scaffold to Prevent Osteomyelitis in a Contaminated *in Vivo* Bone Defect Model. Eur Cells Mater. 2014;27:332-49.
52. Cao, L.Y., Wang, J., Hou, J., Xing, W.L., Liu, C.S., Vascularization and bone regeneration in a critical sized defect using 2-N,6-O-sulfated chitosan nanoparticles incorporating BMP-2. Biomaterials. 2014;35:684-98.
53. Yang, S., Xu, S., Zhou, P., Wang, J., Tan, H., Liu, Y., et al. Siliceous mesostructured cellular foams/poly(3-hydroxybutyrate-co-3-hydroxy-hexanoate) composite biomaterials for bone regeneration. Int J Nanomedicine. 2014;9:4795-807.
54. Kim, M.S., Kwon, J.Y., Lee, J.S., Song, J.S., Choi, S.H., Jung, U.W., Low-dose recombinant human bone morphogenetic protein-2 to enhance the osteogenic potential of the Schneiderian membrane in the early healing phase: *in vitro* and *in vivo* studies. Journal of oral and maxillofacial surgery : official journal of the American Association of Oral and Maxillofacial Surgeons. 2014;72:1480-94.
55. Luderer, F., Begerow, I., Schmidt, W., Martin, H., Grabow, N., Bunger, C.M., et al. Enhanced visualization of biodegradable polymeric vascular scaffolds by incorporation of gold, silver and magnetite nanoparticles. J Biomater Appl. 2013;28:219-31.
56. Faraj, K.A., Cuijpers, V.M.J.I., Wismans, R.G., Walboomers, X.F., Jansen, J.A., Kuppevelt van, T.H., et al. Micro-Computed Tomographical Imaging of Soft Biological Materials Using Contrast Techniques. Tissue Eng Part C-Me. 2009;15:493-9.
57. Kerckhofs, G., Sainz, J., Marechal, M., Wevers, M., Putte van de, T., Geris, L., et al. Contrast-Enhanced Nanofocus X-Ray Computed Tomography Allows Virtual Three-Dimensional Histopathology and Morphometric Analysis of Osteoarthritis in Small Animal Models. Cartilage. 2014;5:55-65.
58. Hoekstra, J.W.M., Beucken van den, J.J.J.P., Leeuwenburgh, S.C.G., Bronkhorst, E.M., Meijer, G.J., Jansen, J.A., Tantalum oxide and barium sulfate as radiopacifiers in injectable calcium phosphate-poly(lactic-co-glycolic acid) cements for monitoring *in vivo* degradation. J Biomed Mater Res A. 2014;102:141-9.

59. Betz, O., Wegst, U., Weide, D., Heethoff, M., Helfen, L., Lee, W.K., et al. Imaging applications of synchrotron X-ray phase-contrast microtomography in biological morphology and biomaterials science. I. General aspects of the technique and its advantages in the analysis of millimetre-sized arthropod structure. Journal of microscopy. 2007;227:51-71.
60. Bech, M., X-ray imaging with a grating interferometer. 2009.
61. Albertini, G., Giuliani, A., Komlev, V., Moroncini, F., Pugnaloni, A., Pennesi, G., et al. Organization of Extracellular Matrix Fibers Within Polyglycolic Acid-Polylactic Acid Scaffolds Analyzed Using X-Ray Synchrotron-Radiation Phase-Contrast Micro Computed Tomography. Tissue Eng Part C-Me. 2009;15:403-11.
62. Weiss, P., Obadia, L., Magne, D., Bourges, X., Rau, C., Weitkamp, T., et al. Synchrotron X-ray microtomography (on a micron scale) provides three-dimensional imaging representation of bone ingrowth in calcium phosphate biomaterials. Biomaterials. 2003;24:4591-601.
63. Sun, W., Li, Z.R., Yang, Y.R., Shi, Z.C., Wang, B.L., Liu, B.L., et al. Experimental Study on Phase-contrast Imaging With Synchrotron Hard X-ray for Repairing Osteonecrosis of the Femoral Head. Orthopedics. 2011;34:E530-E4.
64. Connor, D.M., Hallen, H.D., Lalush, D.S., Sumner, D.R., Zhong, Z., Comparison of diffraction-enhanced computed tomography and monochromatic synchrotron radiation computed tomography of human trabecular bone. Phys Med Biol. 2009;54:6123-33.
65. Connor, D.M., Sayers, D., Sumner, D.R., Zhong, Z., Diffraction enhanced imaging of controlled defects within bone, including bone-metal gaps. Phys Med Biol. 2006;51:3283-300.
66. Momose, A., Fujii, A., Kadowaki, H., Jinnai, H., Three-dimensional observation of polymer blend by X-ray phase tomography. Macromolecules. 2005;38:7197-200.
67. Takashima, K., Hoshino, M., Uesugi, K., Yagi, N., Matsuda, S., Nakahira, A., et al. X-ray phase-contrast computed tomography visualizes the microstructure and degradation profile of implanted biodegradable scaffolds after spinal cord injury. J Synchrotron Radiat. 2015;22:136-42.
68. Appel, A.A., Larson, J.C., Somo, S., Zhong, Z., Spicer, P.P., Kasper, F.K., et al. Imaging of Poly(alpha-hydroxy-ester) Scaffolds with X-ray Phase-Contrast Microcomputed Tomography. Tissue Eng Part C-Me. 2012;18:859-65.
69. Pereira, G.R., Rocha, H.S., Calza, C., Anjos, M.J., Lima, I., Perez, C.A., et al. 3D elemental distribution images in biological samples by XRF mu CT. X-Ray Spectrom. 2011;40:260-4.

70. Klodowski, K., Kaminski, J., Nowicka, K., Tarasiuk, J., Wronski, S., Swietek, M., et al. Micro-imaging of implanted scaffolds using combined MRI and micro-CT. Computerized medical imaging and graphics : the official journal of the Computerized Medical Imaging Society. 2014;38:458-68.
71. Schulz, G., Waschkies, C., Pfeiffer, F., Zanette, I., Weitkamp, T., David, C., et al. Multimodal imaging of human cerebellum - merging X-ray phase microtomography, magnetic resonance microscopy and histology. Scientific reports. 2012;2:826.
72. Lee, C.L., Min, H., Befera, N., Clark, D., Qi, Y., Das, S., et al. Assessing cardiac injury in mice with dual energy-microCT, 4D-microCT, and microSPECT imaging after partial heart irradiation. Int J Radiat Oncol Biol Phys. 2014;88:686-93.
73. Locatelli, E., Gil, L., Israel, L.L., Passoni, L., Naddaka, M., Pucci, A., et al. Biocompatible nanocomposite for PET/MRI hybrid imaging. International Journal of Nanomedicine. 2012;7:6021-33.
74. Tetsumoto, S., Takeda, Y., Imai, H., Kimura, A., Jin, Y., Nakanishi, K., et al. Validation of noninvasive morphological and diffusion imaging in mouse emphysema by micro-computed tomography and hyperpolarized (129)Xe magnetic resonance imaging. American journal of respiratory cell and molecular biology. 2013;49:592-600.
75. Sun, Y., Ventura, M., Oosterwijk, E., Jansen, J.A., Walboomers, X.F., Heerschap, A., Zero echo time magnetic resonance imaging of contrast-agent-enhanced calcium phosphate bone defect fillers. Tissue engineering Part C, Methods. 2013;19:281-7.
76. Srinivas, M., Heerschap, A., Ahrens, E.T., Figdor, C.G., Vries de, I.J.M., (19)F MRI for quantitative *in vivo* cell tracking. Trends Biotechnol. 2010;28:363-70.
77. Srinivas, M., Cruz, L.J., Bonetto, F., Heerschap, A., Figdor, C.G., Vries de, I.J.M., Customizable, multi-functional fluorocarbon nanoparticles for quantitative *in vivo* imaging using (19)F MRI and optical imaging. Biomaterials. 2010;31:7070-7.
78. Ventura, M., Boerman, O.C., Franssen, G.M., Bronkhorst, E., Jansen, J.A., Walboomers, X.F., Monitoring the biological effect of BMP-2 release on bone healing by PET/CT. Journal of controlled release : official journal of the Controlled Release Society. 2014;183:138-44.
79. Tremoleda, J.L., Khalil, M., Gompels, L.L., Wylezinska-Arridge, M., Vincent, T., Gsell, W., Imaging technologies for preclinical models of bone and joint disorders. EJNMMI research. 2011;1:11.
80. Pagnanelli, R.A., Hanson, M.W., Turkington, T., Coleman, R.E., Borges-Neto, S., Gated 99mTc-tetrofosmin and 18F-FDG studies: a comparison of single-acquisition and separate-acquisition protocols. Journal of nuclear medicine technology. 2002;30:175-8.

81. Wong, F.C., Kim, E.E., A review of molecular imaging studies reaching the clinical stage. Eur J Radiol. 2009;70:205-11.
82. Chapman, S.E., Diener, J.M., Sasser, T.A., Correcher, C., Gonzalez, A.J., Avermaete, T.V., et al. Dual tracer imaging of SPECT and PET probes in living mice using a sequential protocol. American journal of nuclear medicine and molecular imaging. 2012;2:405-14.
83. Eggl, E., Schleede, S., Bech, M., Achterhold, K., Loewen, R., Ruth, R.D., et al. X-ray phase-contrast tomography with a compact laser-driven synchrotron source. P Natl Acad Sci USA. 2015;112:5567-72.

# CHAPTER 3

# Three-dimensional localization of implanted biomaterials in anatomical and histological specimens using combined X-ray computed tomography and 3D surface reconstruction

**Vincent M.J.I. Cuijpers, X. Frank Walboomers, John A. Jansen.**

**Tissue Eng Part C Methods. 2010 Feb;16(1):63-69.**

## INTRODUCTION

In biomaterials and tissue engineering research, multiple descriptive research methods as histology, immunohistochemistry, histomorphometry and image analysis are combined to understand scaffold-to-tissue relations and interaction. In order to adequately process tissues from patients and animal studies, it is desirable to know the exact three dimensional (3D) position of structures or objects within different tissue samples in relation to the specimen surface. Without knowing the exact location of the object of interest, it is hard to trim tissue blocks to the desired size or to determine the optimal sectioning plane in relation to the internal biomaterial/scaffold structure. E.g. when histological sections have to made perpendicular or parallel to the object (or an anatomical) structure.

Further, basic information of the object, such as surface pattern and color, is lost when processing the sample. Recording and the availability of this information can be very useful when evaluating and analyzing results. The application of 3D Surface Reconstruction (SR) can be a useful tool to localize structures of interest within an object because of the additional photorealistic texture information like color and surface pattern.[1,2] In addition, computed tomography (CT) techniques such as X-ray cone beam CT and micro-CT can be used to visualize radiodense biomaterials (metals, ceramics) within the specimens. A combination of 3D SR models and 3D CT models can then give more insight into the exact localization of the scaffold, and thus how to handle the sample for further histological processing.[3-5]

Therefore, for the current study we hypothesized that fusion of a transparent 3D SR model including all surface information and landmarks, with the 3D model derived from CT is an optimal approach to facilitate the exact localization of anatomical structures, biomaterials, and tissue-engineered scaffolds, and further tissue processing.

# MATERIALS AND METHODS

## Used specimens

A small sphere with a 1.5 cm diameter was used to determine the calibration error of the 3D SR set-up, by checking whether the object became indeed reconstructed as a sphere. A hydroxyapatite-phantom cylinder of 4mm in diameter and 6mm in height, normally used in bone mineral density research, and an air-dried extracted human molar with evident caries were used for 3D SR to check the minimal size of objects as can be studied and combined in 3D SR and 3D micro-CT models.

The right part of the lower jaw of a macaque monkey, with dimensions of approximately 7.5cm in length and 2.5cm height and containing a modular endoprosthesis made of Ti-Al6-V4, was used to make a 3D SR, as an example of a structure of larger dimensions. Finally the left part of a porcine lower jaw, with dimensions of approximately 25 cm in length and 15 cm in height, was used. In this jaw, three radiodense reference objects, i.e. a titanium disk (diameter 6.0mm, 0.8mm height), a massive titanium rod (diameter 4.0mm, length 3.0mm) and a titanium screw implant, were placed at different positions to analyze whether landmarks can be added for proper localization of the object of interest. Therefore, first an incision was made in the connective and muscle tissue surrounding the jaw bone, followed by the installation of the titanium rod and titanium screw implant into the two holes as drilled in the jaw bone. The titanium disk was placed subcutaneously. Finally, the connective and muscle tissue were sutured back in place. All samples were fixed for 10 days in a 4% formaldehyde solution, rinsed using demineralized water, and placed into a 70% ethanol solution.

## 3D surface reconstruction

For the examination of all three types of specimens, a 3D SR set-up was established (Figure 1). The sample was placed on a mold made of Optosil Comfort Putty combined with Optosil Xantopren universal activator paste (Heraeus Kulzer, Dormagen, Germany) and placed on a rotating horizontal stage containing a calibration sheet for registration of the landmarks.
Images were taken using a Nikon (Nikon, Tokyo, Japan) D70 camera and a Nikon Nikkor AF-S 18-70mm or Sigma (Nieuwegein, The Netherlands) 105 mm 1:2.8D DG Macro objective, depending on the size of the sample, under a fixed angle of 45°, each 10° of the total rotation of 360°, resulting in 36 high-resolution images (3008 x 2000 pixels). The specific software iModeller 3D Professional Edition 2.6 (UZR GmbH & Co, Hamburg, Germany) was used for 3D SR.

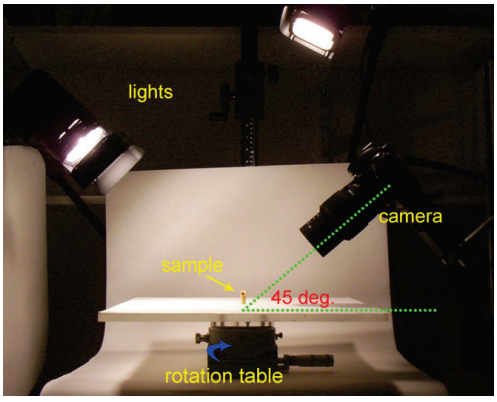


**Figure 1.** Three-dimensional surface reconstruction (3D SR) setup. Regular illuminated sample on rotation step table, acquiring images on an angle of 45°.

## X-ray computed tomography

Depending on the size of the sample studied, two different methods of X-ray CT were used. Micro-CT under optimal conditions theoretically can have a maximal spatial resolution of 4-5µm, whereas whole-body CT systems can reach up to 0.2mm. However, micro-CT is not able to handle specimens sizes above approximately 2.5cm in diameter. In

this study, we used the Skyscan 1072 desktop X-ray micro-CT system (Skyscan, Kontich, Belgium) for small objects, and subsequently the i-CAT cone beam 3D-dental imaging system (Imaging Sciences International, Hatfield, PA) for large objects.[6,7]

The Skyscan 1072 desktop X-ray micro-CT system has a focal spot of 7µm, a 1024x1024x12 bit digital cooled CCD X-ray detector, and the scanning settings were set to magnification 15x, rotation step 0.9°, field of view 19.13mm, and X-ray source 100 kVp, 98µA (10W). The distance from the sample to the detector determines the magnification factor. The cone beam reconstruction method according to Feldkamp was performed using the NRecon V1.4.4. (Skyscan) software package. The X-ray source of the i-CAT system, with a high frequency fixed anode, was set to 121 kVp and 47,74 mA. Compared to micro-CT, resolution was notably lower with a focal spot of 0.5mm. In contrast to micro-CT, where the X-ray beam and detector are fixed and the sample is rotating, in the i-CAT machine the X-ray beam and detector are rotating 360° around the sample during image acquisition, with a rotation step of 1.15°. Further, i-CAT did not involve magnification of the image beyond 1x. During rotation, the amorphous silicon flat panel image detector of 20 x 25cm in dimension, containing a cesium iodide conversion layer, acquired all projected images in 12-bit gray scale. Thereafter, using the i-CAT image reconstruction algorithm, the projected images were reconstructed and converted into a stack of DICOM format image files and converted from 16-bit gray-scale to 8-bit gray-scale images using 3D-Doctor software. In principle, the i-CAT system can also scan for soft tissue contour, but only with a very limited resolution and no information on texture and color.[6.7] Hence, this acquisition mode was not applied.

For both techniques, subsequently, the files were imported in CT-Analyser V1.7 (Skyscan) and then re-sliced, and the volume of interest was selected, while images without useful information were discarded. The volume of interest files was imported in 3D-Doctor (V4.0) (Able Software Corp., Lexington, MA) and interactive segmentation was performed to generate bone object boundaries (grey value range, 190-255). A 3D polygonal representation was finally generated using complex surface rendering with the recommended software settings for denseness of triangle mesh using

Rhinoceros (V4.0). Flamingo (V1.1) software (Robert McNeel & Associates, Seattle, WA) was used for 3D reconstruction and full-color photorealistic rendering of 3D SR models.

## RESULTS AND DISCUSSION

The 3D SR setup proved easy to construct; using SR software, representative suitable reliable 3D SR models could be created. Creating and merging 3D models derived from different techniques requires standardization. A relative solid ingenious 3D SR technique was chosen to create 3D SR models using commercially available semi automated software. A correct 3D SR setup, decent calibration, and a uniform white background were essential for acquiring suitable images for 3D SR software processing. Out of focus and shadow of the object influence the image quality and therefore the final 3D SR model. Further, attention must be paid to the angle between the camera and horizontal surface on which the sample is placed to avoid distorted 3D SR models. When increasing the angle, texture information located at the base of the sample was reduced, while decreasing the angle, the surface texture information at the top of the sample was reduced. Although the creation of a second 3D SR model of the same object after turning it upside down and the junction of this model with the first initial 3D SR model can presumably optimize the final merged 3D SR model, this was not necessary for the purpose of our study. Besides a higher pixel size of the images, the resolution and texture of the 3D SR models can be increased when acquiring more images at smaller standardized rotation angles. The mesh resolution also plays an important factor in the final 3D SR model. Increasing the mesh resolution will improve the number of polygons, color and texture detail, but will also amplify noise and errors from the original two-dimensional images.

Using CT systems, the micro-CT and i-CAT equipment, 3D models of objects of different sizes can be generated. Furthermore, by utilizing specific software programs, merging of 3D SR and 3D CT models was found to be possible.

## Results 3D surface reconstruction

Performing SR software processing, the reference points on the calibration sheet were used to align all images, and a masking tool was used to select the parts that were to be reconstructed (Figure 2).

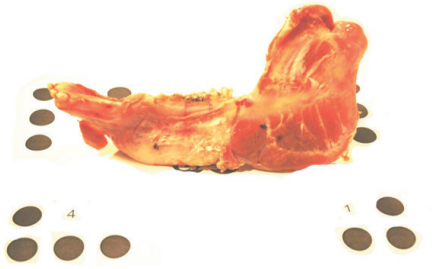

**Figure 2.** Three-dimensional SR software processing: a sample placed on calibration sheet containing reference points to align all images.

Finally, a wire-frame or plain 3D model was created using surface rendering. The model could be created and viewed using a different mesh resolution depending on the final resolution of the 3D model. The texture mode finally created the color and pattern of the objects' surface, whereby all texture information was saved in a separate texture chart file. Increasing the mesh resolution and the number of polygons resulted in more detailed smooth 3D SR models with less jagged shaped objects. However, amplified errors and artefacts were induced when the mesh resolution was set to the maximum (4.41 x $10^4$ polygons). The texture file charts showed clearly the increasing amount of polygons and related texture information of each different mesh resolution setting (Figure 3).

Using a standardized model as a sphere, the 3D SR set-up could be checked, calibrated and eventually corrected. 3D SR was possible of objects of different sizes, from a few cm as the human molar, up to approx. 20 cm as the porcine mandible. 3D SR showed clearly the texture information as surface pattern and color of these samples as depicted in Figure 4.

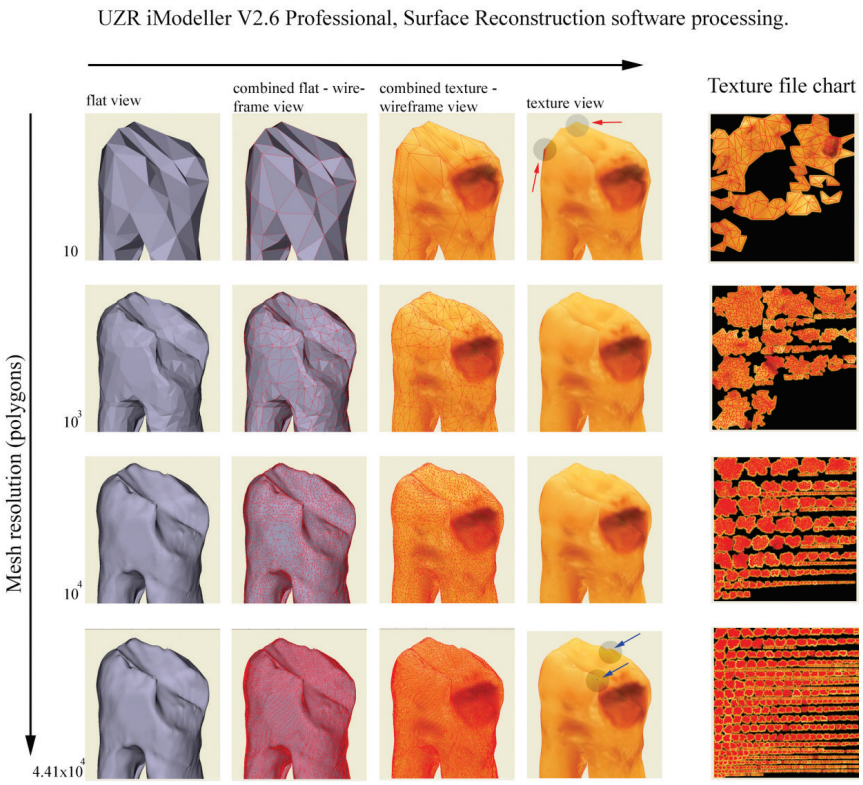


**Figure 3.** Three-dimensional SR software processing of a human molar: mesh resolution (polygon number) related to 3D SR texture quality. Increase in polygon number is related to increase in smoothness and texture. Red arrows indicate jagged 3D objects due to low number of polygons ($10^2$). Blue arrows indicate artefacts at maximum mesh resolution ($4.41x10^4$ polygons).

Different software packages could be used to merge the two separated 3D models derived from the different SR and CT techniques. The most suitable compatible 3D format file when merging SR 3D and CT 3D reconstructions using the Rhinoceros software package including texture characteristics are *object* (OBJ) and *three-dimensional studio* (3DS). The stereo lithography (STL) format file without texture information is sufficient for creating 3D CT models.
The SR-3D reconstruction of small objects was complicated due to the increased influence of the SR set-up, like focussing, camera angle and

distance of the sample to the camera.

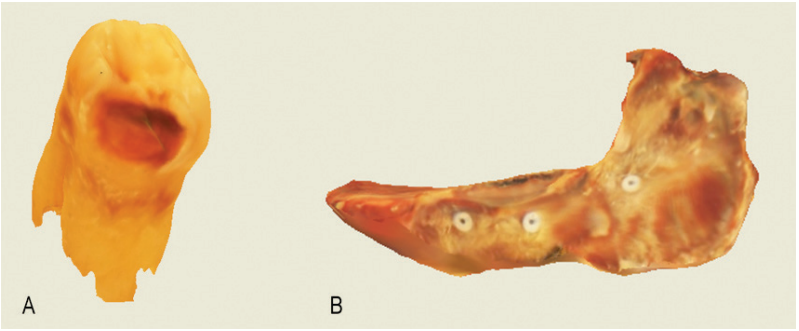


**Figure 4.** Final 3D SR models of (A) a human molar showing the carries affected area and (B) the left part of porcine lower jaw containing attached dots, suitable surface landmarks.

## Results 3D computed tomography

The major advantage of the micro-CT system for small objects is the relative high resolution, due to the small focal spot size and distance of the sample to the detector compared to the i-CAT cone beam CT system. Therefore, the dimensions of the objects to study determine the choice of X-ray CT. Using the micro-CT system, the affected human molar showed a diversity of different radio densities through which several internal structures of the human molar as root channels, dentine and enamel could be visualized in 3D (Figure 5).

Performing X-ray CT, the i-CAT cone beam X-ray CT system was used, which has a higher resolution compared to traditional conventional whole body CT systems, while the cone beam reconstruction is not limited by distortion, magnification changes, restricted clarity, and lack of accuracy in image measurements. The i-CAT provides high-definition images at 0.2mm voxel size of objects up to 17cm in diameter and 13cm in height. Additionally, implanted biomaterials are easily to locate in large samples. A disadvantage remains the low resolution compared to micro-CT.


**Figure 5.** Visualization of 3D micro-computed tomography (CT) models of a caries affected human molar (in pink, A) showing different partly transparent and combined 3D structures as root channels (B), enamel (in orange, C and D) and dentin (in yellow, E).(F) Combined image from transparency of (A) together with (E). Segmentation was based on greyvalue threshold settings of the different radiopaque structures of interest.

Nevertheless, the i-CAT Cone Beam CT application, in combination with the i-CAT specific observation software showed clearly the radiodense massive and hollow titanium landmarks as placed in the porcine mandible (Figure 6). These landmarks were not only visible in two-dimensional cross-sections, but could also easily found back in the final generated 3D reconstruction. The location of the massive titanium implant in the lower jaw of the macaque was also detectable.

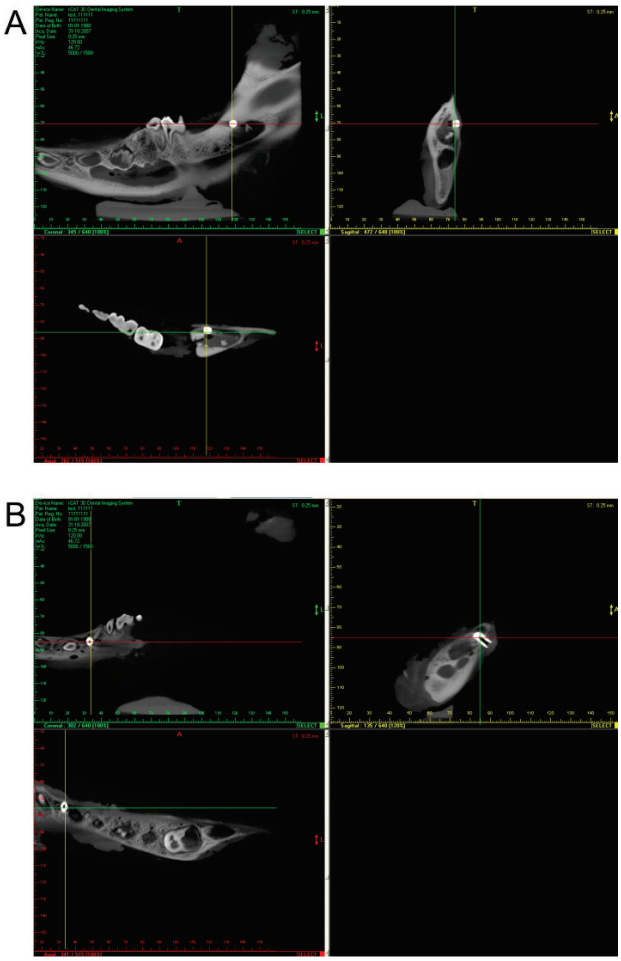


**Figure 6.** Coronal, sagittal, and axial views of the locations of an implanted titanium disc (A) and (B) screw in the lower jaw of a macaque species using i-CAT cone beam 3D dental imaging specific visualization software.

## Fusion of 3D surface reconstruction and 3D computed tomography models

Merging the 3D SR and the 3D micro-CT of the human molar associated the surface information with the internal structures of the molar. The distance of the affected dark reddish brown transparent SR model to the radiodense structures viewed by micro-CT was simple to

determine (Figure 7A). For this purpose, the 3D SR and 3D micro-CT models were imported into 3D-Doctor software, followed by Rhinoceros software (V4.0; Robert McNeel & Associates), for scaling, rotation, and full-color photorealistic rendering. This resulted in both 3D models placed on each other. Merging and full-color photorealistic rendering, including lights, transparency, shadows and textures, of the 3D SR models was done using Flamingo (V1.1) (Robert McNeel & Associates) to enhance observation of the evident caries and finally to determine the dimensions and depth of the caries.

When the porcine jaw was evaluated, a similar result was obtained, but one additional step was required, i.e. using the 3D-Doctor software program, both 3D SR and 3D CT models were imported and the shape function had to be used to adjust the X, Y and Z rotation values in degrees, and X, Y and Z moving values of the 3D models were adjusted within the 3D space. Re-positioning was also performed using the Rhinoceros software transforming functions as moving, 3D-scaling, 3D-rotating and alignment.

Finally, the surface of the imported 3D SR model was rendered using Flamingo software and the texture transparency intensity was set to 75%. When the transparent color 3D SR model and the 3D CT model were merged, the underlying 3D CT model became clearly visible (Figure 7B, C) showing texture and color, and the implanted biomaterials within the object of interest. Radiopaque landmarks, as titanium rods placed into the tissue or in combination with colored features as small ink spots placed onto the objects surface, display in combination with the localization of structures within the 3D CT model how to handle the object for further histological processing as sawing and slicing. Additional evidence of the usefulness of merging 3D SR and 3D cone beam CT was provided during analysis of the macaque tissue sample.

Besides adding an extra box and the X, Y and Z axis, the position of the structure of interest was easily located. The exact localization of the object assisted and facilitated how to cut and handle the tissue for further histological processing. Using different gray-value threshold settings in 3D-Doctor™ software, variations in transparency of the

different 3D CT models as the radiopaque titanium implant in the more radiodense lower jaw tissue of the macaque contributed in better visualization of implant both in hard and soft tissue (Figure 7D, E). The exact location of the implant depicted in Figure 7, as well as the informative texture features of the transparent soft and hard tissues, assisted in a proper histological sectioning of the sample, i.e. perpendicular to the red arrows.

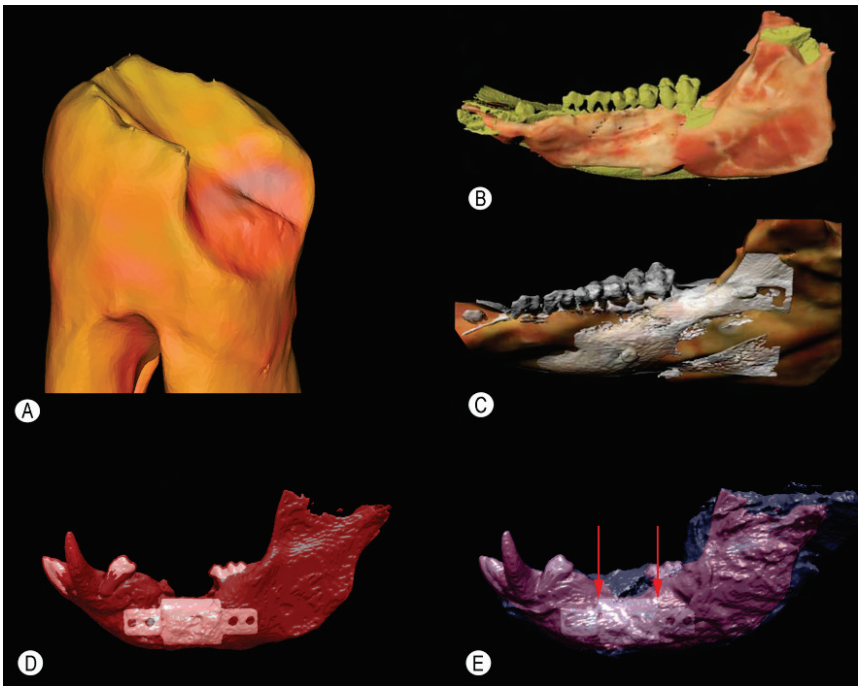


**Figure 7.** Visualization of merged 3D SR and 3D CT models and localization of implanted biomaterials in tissue. (A) merged 3D SR and 3D CT model of an affected human molar. (B) Merged 3D SR and 3D CT model of the left porcine lower jaw part, partially transparent 3D SR model with underlying bone and teeth in (C). (D) Massive titanium implant (yellow arrow) viewed in the lower jaw bone (in red) of a macaque. Note the same artificial white colored teeth and implant due to the corresponding radiodensity. (E) The exact location of the implant depicted in the same sample, bone and teeth in transparent dark purple, and soft tissue in transparent dark blue. Red arrows could indicate a possible site to cut the sample for further histological processing.

Registration of the two different 3D models, 3D CT and SR 3D, is an important essential step for fusion of the models.[3-5,8-11] Besides ink or other marks placed onto the object surface, X, Y and Z axis placed into the 3D space can be used as additional tool for localization of the implanted biomaterials. Even though automatic registration in 3D is often used, scaling and landmark-based registration of both complete 3D models, 3D CT and 3D SR, into a 3D space can be done manually with the use of ink placed on the objects surface or metal rods placed in the tissue. Furthermore, automatic registration of complete 3D models, as iterative closest point algorithm used to merge two cloud-point models, is not always incorporated in all 3D reconstruction software programs.

## CONCLUSION

Visualization of 3D surface reconstruction, including basic photorealistic texture characteristics as surface pattern and color combined with X-ray 3D computed tomography reconstruction at different levels, is a useful approach to localize certain anatomical structures, biomaterials, or tissue-engineered scaffolds within experimental tissue samples. Because of the possible visualization of structures of interest in a 3D environment, fusion of these techniques can greatly facilitate histological processing. As described herein, the technique is rather elaborate and thus only feasible for delicate specimens that require exact processing. However, after establishment of the technique, the development of hardware and software applications will be optimized to simplify the combination of 3D visualization and inspection techniques in the future.

## REFERENCES


1. Tsyganov, E.N., Antich, P.P., Kulkarni, P., Manson, R.P., Parkey, R.W., Seliuonine, S.Y., Shay, J.W., Soesbe, T.W., Zhezher, V., Zinchencko, A.I., 3D Reconstruction using optical images [Internal report]. University of Texas Southwestern Medical Center, Dallas, E19-2005-112, May 9 , 2003.
2. Niederöst, M., Niederöst, J., Ščučka, J., Automatic 3D reconstruction and visualization of microscopic objects from a monoscopic multifocus image sequence. International Archives of the Photogrammetry, Remote Sensing and Spatial Information Sciences, Vol.XXXIV-5/W10
3. Khambay, B., Nebel, J.C., Walker, F., Bowman, J., Hadley, D., Ayoub, A.F., A pilot study: 3D photogrammetric image superimposition on to 3D CT scan images - the future of orthognathic surgery. Int J Adult Orthod Orthognath Surg. 2002;17:331.
4. Ayoub, A.F., Xiao, Y., Khambay, B., Siebert, J.P., Hadley, D., Towards building a photo-realistic human face for craniomaxillofacial diagnosis and treatment planning. Int. J. Oral Maxillofac. Surg. 2007;36:423.
5. Miller, L., Morris, D.O., Berry, E., Visualizing three-dimensional facial soft tissue changes following orthognathic surgery. Eur. J. Orthod. 2007;29(1):14.
6. Pinsky, H.M., Dyda, S., Pinsky, R.W., Misch, K.A., Sarment, D.P., Accuracy of three-dimensional measurements using cone-beam CT. Dentomaxillofac. Radiol. 2006;35:410.
7. Scarfe, W.C., Farman, A., Sukovic, P., Clinical applications of Cone-Beam Computed Tomography in Dental Practice. J Can Dent Assoc, 2006;72:75.
8. Sun, W., Starly, B., Nam, J., Darling, A., Bio-CAD modelling and its applications in computer-aided tissue engineering. Computer-Aided Design. 2005;37:1097.
9. Weng, N., Yang, Y.H., Pierson, R., 3D surface reconstruction using optical flow for medical imaging. *IEEE Trans. on Medical Imaging. 1997;*16(5):630.
10. Mamourian, A. C., Pluta, D.J., Eskey, C.J., Merlis, A.L., Optimizing computed tomography to reduce artefacts from titanium aneurysm clips: an *in vitro* study. Technical note. J Neurosurg. 2007;107:1238.
11. Tsyganov, E.N., Antich, P.P., Kulkarni, P.V., Mason, R.P., Parkey, R.W., Seliuonine, S.Y., Shay, J.W., Soesbe, T.W., Zinchenko, A.I., Micro-SPECT combined with 3D optical imaging. Nuclear Science Symposium Conference Record, 2004;5:3275

# CHAPTER 4

# Scanning electron microscopy stereo-imaging for three-dimensional visualization and analysis of cells in tissue engineered constructs

**Vincent M.J.I. Cuijpers, X. Frank Walboomers, John A. Jansen.**

Tissue Eng Part C Methods. 2011 Jun;17(6):663-668.

## INTRODUCTION

In tissue engineering research, different techniques are available to study cells, cell structures, biomaterials and their relations. Depending on the research question, various methods are suitable for visualization, each with their respective pros and cons.
Surface measurements methods include profilometry, (environmental) scanning electron microscopy ([E]SEM), atomic force microscopy (AFM) and laser interferometry, whereas volumetric measurement methods include for example, brightfield and fluorescence microscopy (using shape from focus), confocal laser scanning microscopy (CLSM), and micro-computed tomography (micro-CT). For three-dimensional (3D) assessment CLSM requires fluorescent labeling, whereas the obtained resolution in depth of the image (z-direction) is restricted to the micrometer scale. Micro-CT is a valuable method if 3D morphometric analysis of biomaterials has to be performed. This non-destructive and non-invasive quantification method is based on X-ray tomography and is especially useful because of its relative high resolution (down to 1 μm). After X-ray image acquisition and cone beam reconstruction, 3D information of the studied sample is obtained, and surface- or volume-rendered 3D models can be created. A known disadvantage is the occurrence of scattering of the X-rays. As a consequence, the interface between biological and radiopaque biomaterials cannot always be analyzed correctly. Synchrotron X-ray micro-tomography, using monochromatic X-ray beams, provides more detailed 3D information and has more advantages as higher resolution, but this technique is less accessible and not available to easily develop into routine laboratory or clinical application. [1-3]
In contrast to these micro-CT techniques, SEM can be used to analyze radiolucent materials as human tissue, radiodense materials as biomaterials and scaffolds, and the surface of radiopaque materials as titanium (Ti) implants and scaffolds. SEM creates highly magnified gray-scale images of the studied objects and approximately has a factor 1000x higher resolution than micro-CT. Also, SEM provides very high focus depth images, which give a pseudo-3D view. Still, only the

surface of the samples can be analyzed. Newly developed SEM tools such as focus ion beam SEM can create and analyze the 3D structure immediately.[4,5] However such techniques are destructive so the original sample integrity will be lost.

To fill the obvious void in analysis techniques between micro-CT and routine SEM, stereo-imaging SEM can be proposed. Weibel et al. already described practical stereological methods for morphological analysis of cells in 1966.[6] Stereo height measurements in scanning electron microscopy were elucidated by Cripps et al.[7] 3D stereoscopic imaging is used for various research purposes. Besides these virtual stereoscopic images, 3D morphometry information as depth, 3D profile and volume can be generated from different structures and surfaces. Several studies describe algorithms and methods by[8-10], and nowadays specific 3D stereoscopic imaging software is commercially available.[11-15] We can find the 3D SEM application in various research fields as in cosmetics,[16] food industry[17,18] wear of materials[19,20] and frequently in medical research.[21,22] A major advantage is that this 3D SEM application could be used on mostly every material and specimen. Besides, the application is already combined and compared to other 3D imaging techniques as AFM.[23,24]

However, such 3D SEM quantification has not been applied for tissue engineering scaffolds provided with cells, although this technique can yield important information. In tissue engineering there is a constant focus on the improvement of scaffold materials. Overall design, physicochemical properties, and surface composition and roughness are modulated extensively to obtain smart scaffolds which can actively influence cell attachment, cell spreading and cell morphology. However, it is difficult to study these phenomena quantitatively in the porous and/or non opaque scaffold environments which are typical for tissue engineering.

Therefore, in the current study, SEM and 3D stereo-imaging were combined to visualize and analyze 3D cell morphology and cellular interaction with biomaterials.[25,26] We hypothesize that 3D SEM quantification could accurately be validated using standardized microspheres. Furthermore we hypothesize that 3D SEM could be used to provide quantitative information of single cell spreading on the surface of a non-opaque scaffold material.

## MATERIALS AND METHODS

Three different sized of polymethyl metacrylate microspheres (Fluka, Buchs, Switzerland) were used: Ø 10, 20 and 100 µm, The microspheres were assessed on solid Ti discs (Ø 12 mm, 1.5 mm height), or mixed with calcium phosphate (CaP) cement. This cement consisted of 85% α-tri-calcium phosphate (α-TCP) sinterered powder (CAM Bioceramics BV. Leiden, The Nethelands), 10% CaP dibasic (Sigma, St. Louis, MO) and 5% hydroxyapatite (Merck, Darmstadt, Germany). A ratio of 380 µL (2%) $Na_2HPO_4$ (Merck) solution to 1g CaP was used for hardening the cement. The final weight ratio of CaP to microspheres was 100 to 1. For each type of microsphere always at least 10 examples were selected at random for analysis. Subsequently, two types of biomaterial scaffolds were used for cell culture, i.e. the Ti substrates, and preset CaP cement discs (Ø 6 mm, 3.0 mm height) made from the same material as above. These Ti and CaP discs were autoclaved and subsequently investigated with the addition of MC-3T3 cells.

### Cell culture

Murine MC3T3-E1 subclone-14 pre-osteoblastic cells (ATCC, Manassas, VA) were cultured in α-Minimum Essential Medium (α-MEM)(Gibco BRL, Canada) supplemented with 10% fetal bovine serum (FBS) at 37° in an atmosphere of 100% humidity and 5% $CO_2$. The complete medium was replaced every 1-2 days until subconfluency was reached. To study the cell morphology, cells were seeded on the surface of Ti or CaP scaffolds at a density of $5x10^5/cm^3$. The cells were allowed to adhere to the scaffolds for 15, 30, 45, 60, 120 and 240 minutes until further analysis. Again, for each disc and at each time point, at least 10 representative cells were selected at random for analysis.

## Scanning electron microscopy

Scaffolds with microspheres or cells were washed twice in phosphate-buffered saline (PBS) and fixed for 5 minutes in 2% glutaraldehyde in 0.1M sodium cacodylate buffer (pH 7.4), dehydrated in serial ethanol (70%, 80%, 90%, 96%, 100% and filtered 100% ethanol) and dried using tetramethylsilane (TMS) to air. The specimens were coated using a 30mnm thin layer of Au-Pd, using a Cressington sputter coater 208HR (Watford, United Kingdom), while mounted onto Al stubs using carbon tape and imaged using a JEOL JSM 6330F Field Emission SEM (JEOL Corporation, Tokyo, Japan) operated at an accelerating voltage of 3 keV.

## Three-dimensional scanning electron microscopy

Spheres were applied onto the Ti material, or into the CaP cement material. Standardized eucentric tilted high-quality SEM photomicrographs were collected at -5°, 0 and +5°, and exported using the JEOL PC SEM V3.20 software Package (JEOL). For imaging, the required illumination, contrast, sharpness, disparity, magnification and tilting angle were determined. Also, SEM settings as working distance, bar size and eucentric tilting were recorded as these are essential for later 3D reconstruction and further 3D analysis.

## Alicona MeX analysis

All tilted pairs of images of all samples, the calibration microspheres and MC-3T3 cells on the different biomaterials, were imported into Alicona MeX V4.1. software (Alicona Imaging GmbH, Graz, Austria). The SEM images were calibrated using the bar size, tilting angle and working distance, and subsequently a virtual anaglyph image was automatically created to get more insight into the real 3D structure. Both the path length (x-axis) and height (y-axis) of the calibration spheres and MC-3T3 cells were determined along the optimal axis using the primary profile analysis tool. Thereafter, the region of interest (ROI) of the cell was determined by selecting a defined area

around the cell including cell processes using the volume analysis module. The Z-position of the reference plane was adjusted and defines finally the bounding frame of the base of the 3D model. The cutting plane was rotated around the x and y axis to set the volume of interest (VOI).
The total cell volume was calculated after adjusting and fine-tuning the surface of the cutting plane by visual inspection of the surface of the substrate and cutting plane.
After creating the final 3D volume of the object, all 3D data points were exported and saved in VRML2.0 (*.wrl) format files, which could be viewed with many plug-ins. To get more insight into the exact 3D model, the 3D data were imported and rendered using the more flexible 3D reconstruction software packages Rhinoceros V4.0 (Robert McNeel & Associates, Seattle, USA) and 3D Doctor (Able Software Corp., Lexington, MA). Further, height and length of separate MC-3T3 cells on both Ti and CaP discs were determined by fine-tuning of the X, Y and Z positions of the cutting plane.

## Statistical analysis

Statistical analysis was performed on the spreading of MC-3T3 cells on Ti versus CaP substrates. First, the spreading of the cells was calculated as the ratio of measured height over surface. Since not all combinations of Ti or CaP on different time points contained equal numbers of data, bootstrapping was used to resample the data 1000x and obtain estimated ratio's and standard deviations for each parameter. Subsequently, the ratios on the Ti and CaP material over time, and the differences between Ti and CaP were statistically compared using Student's *t*-test. The significance level was set at $p<0.05$. Calculations were performed in R™(R Development Core Team, Vienna, Austria).

# RESULTS AND DISCUSSION

## Validation analysis

First, the 3D-SEM technique was validated on individual spheres using the profile analysis tool of the Alicona MeX software package (Figure 1). The results on Ti showed that depth values ranged from 94 to 100 µm and width from Ø 95 to 100 µm for 100 µm microspheres. The diameter dimensions found for individual microspheres on Ti matched exactly with the Ø 10 µm and 20 µm materials used. However, the depth values varied in the CaP cements samples because of parts of the microspheres were situated within the cement.

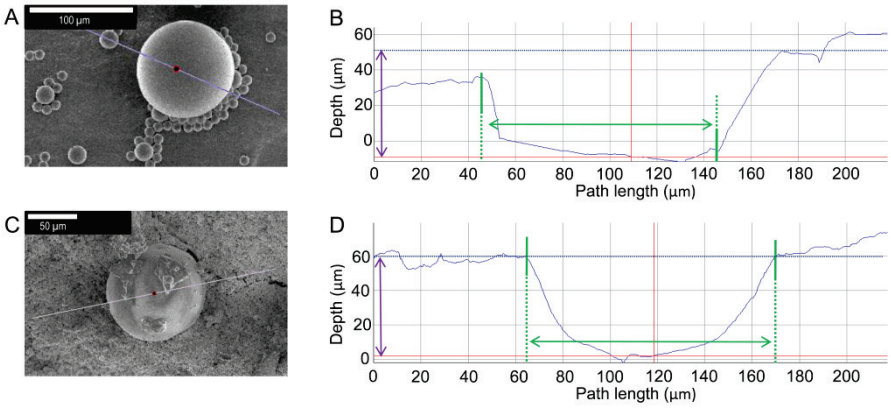


**Figure 1.** Analysis of microspheres. (A,C) Scanning electron microscopy (SEM) images of microspheres, and (B,D) profile of the microspheres along the blue line on the SEM images. (A,B) Ø 100 µm individual micro particle, width 98 µm, height 100 µm (twice 50 µm due to the sphere shape), (C,D) Ø 100 µm partly embedded (40 µm) in calcium phosphate cement samples, width 105 µm and height 60 µm.

Initially, we had also performed the exact same study on the individual microspheres, using a conventional micro-CT system (Skyscan 1072, Kontich, Belgium). In this approach it proved impossible to reliably quantify individual microspheres smaller than 20 µm (data not shown). Only the confirmed validation of 3D-SEM results obtained with the standardized microspheres allowed for subsequent 3D

analysis of MC-3T3 cells.

## Morphometric analysis

After the validation, the real 3D structure of cells was assessed (Figure 2A). The profile analysis module of the Alicona MeX software was used to determine the object height and object width by drawing perpendicular multiple lines over the center of the object, as illustrated in Figure 2B-C. Both parameters were easily distilled from the profile graph. Thereafter, a slightly abundant ROI of the cell was determined by selecting a defined area around the cell, to ensure that all cell processes were included, using the volume analysis module (Figure 2D). The total cell volume was calculated after adjusting and fine-tuning the surface of the cutting plane by visual inspection of the surface of the substrate and cutting plane (Figure 2E).

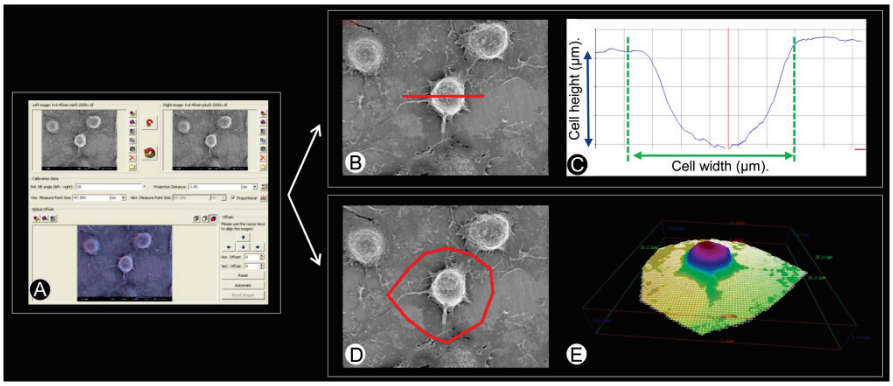


**Figure 2.** Quantitative analysis procedure. (A) Calibration of stereo-pair images. (B,C) Profile analysis module showing cell height and cell width through one direction. (D,E) Volume analysis module showing ROI (in red) and final three-dimensional volume model.

After the measuring method was determined, the behavior of cells in time was regarded. Upon visual inspection of such SEM images, it was evident that the morphological shape of the cells changed in time. On Ti discs, the cells changed after 15-30 minutes from a spherical shape into more elongated phenotype, with branching membrane processes

after 45 minutes (Figure 3A-C). After 1h, the cells became more flat and spread out on the surface. After 2h the cells were completely flat and spread (Figure 3D-E). On CaP discs, besides round spherical cells, some cells were already spread after 30 minutes showing extensive membrane processes.

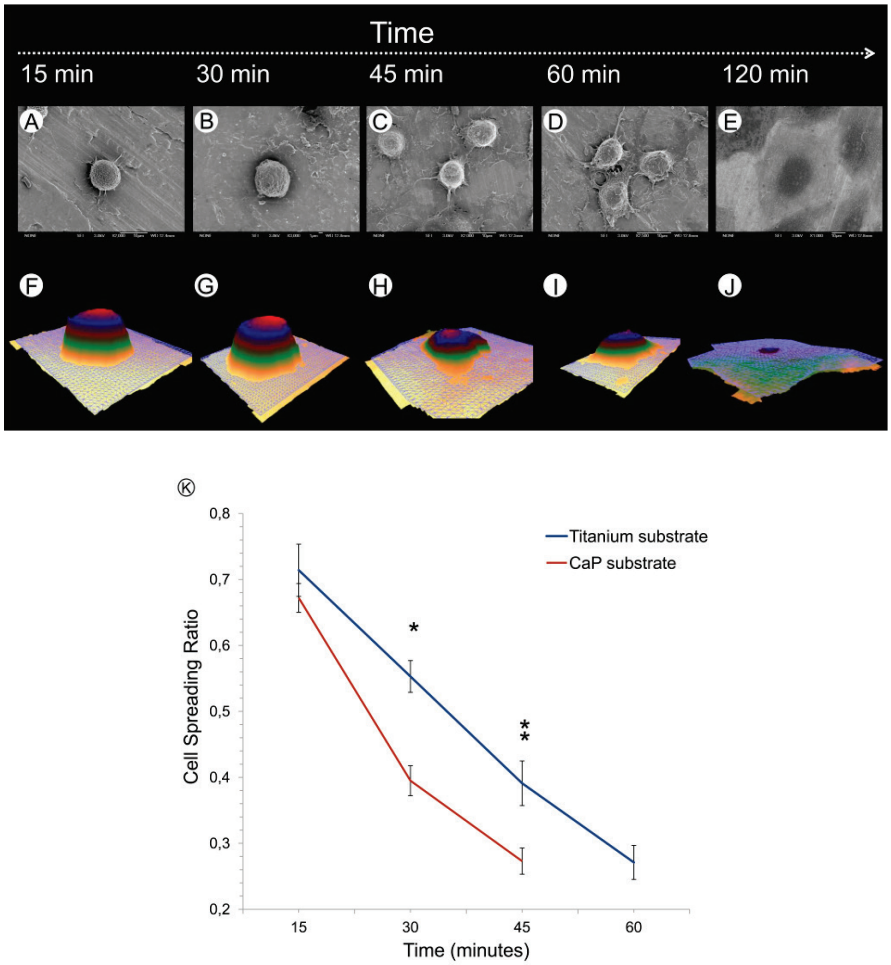


**Figure 3.** Cell spreading analysis. (A-E) Scanning electron micrographs as seen on the titanium samples in time.(F-J) Pseudo-colored depth images of corresponding cells from (A-E). (K) Spreading ratio (cell height/cell length) of cells on titanium and calcium-phosphate substrates in time as derived from all series of images, * $p<0.001$, ** $p<0.005$.

This difference in cell morphology in time clearly indicated a substrate dependency. After this visual inspection of the cell morphology, the cell volume, height, and width were quantified on both Ti (Figure 3F-J) and CaP substrates in time. Logically, cell volume stayed equal and there were no significant differences in time or between substrates (data not shown). However, the quantitative data in the graph in Figure 3K show clearly the difference in spreading ratios of the MC-3T3 cells on Ti and CaP substrates in time. Initially, the cells render an equal measurement. However, the spreading ratio at each subsequent time period is significantly different between the materials (due to the totally completed cells spreading there are no measurement presented beyond the 60 minute time point). The faster decrease in the cell spreading ratio of MC-3T3 cells on CaP discs indicates faster cell spreading compared to MC-3T3 cells on Ti discs. As expected, the surface chemical composition and/or rougher irregular surface of CaP discs initiated expeditious spreading of the MC-3T3 cells. In other words, this substrate dependency could be quantified on the basis of the 3D SEM method, as shown by the statistical differences in Figure 3K.

In our analysis, the ROI, reference and cutting plane adjustment is important for 3D analysis (Figure 4). Especially for the rougher CaP material this proved critical (Figure 4A-D). Incorrect ROI, reference, or cutting plane positions, results in over- or underestimated results. When the cutting plane is placed lower, it becomes evident that material surface volume will erroneously get included in the estimation. For instance, when the plane is lowered by 0.1 µm, the volume increases by 3 $\mu m^3$, which is 2% of the total volume. Opposite, when the cutting plane is placed too high, inclusion of cellular processes is lost, and for instance choosing a plane 0.1 µm too high results in the loss of 15 $\mu m^3$ (i.e. 14%) of volumetric cell measurement (Figure 4E-G). In other words, in our measurement system still careful visual inspection and adjustment of the cutting plane always had to be performed to achieve optimal final results. Reproducibility studies should be necessary to confirm these findings, as logically such results are highly dependent on user decisions. Still, it should be regarded more critical to develop standardization of the ROI, reference, and

cutting planes. The development of further automation is required before this method of analysis can be routinely and swiftly applied on complex 3D scaffold architectures.

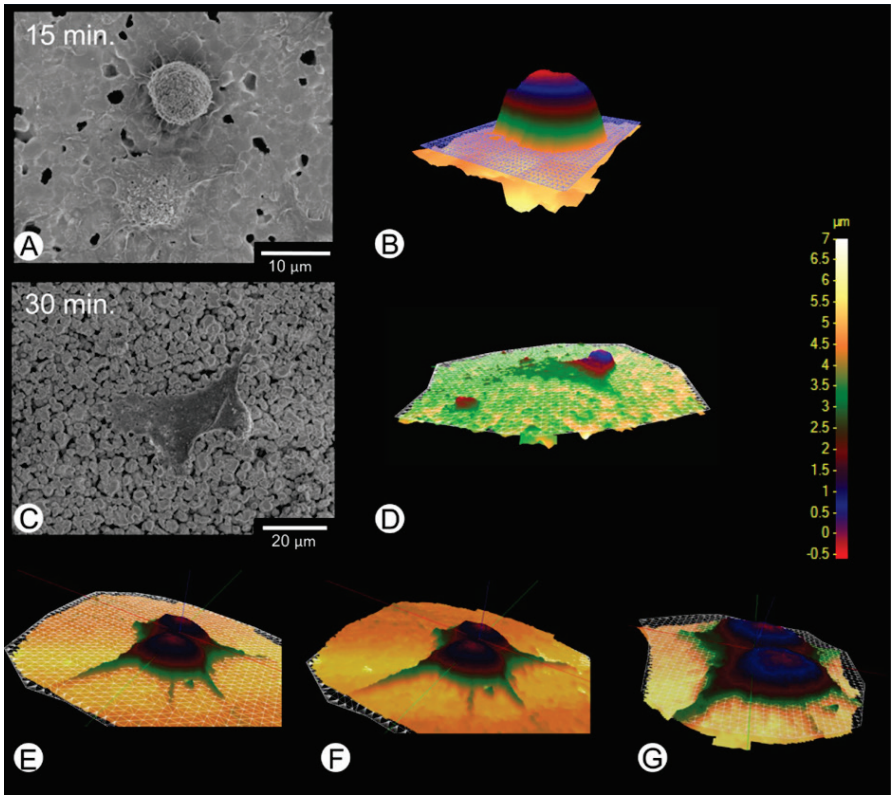


**Figure 4.** Cell morphology, substrate dependency and critical software settings. (A,B) SEM and three-dimensional pseudo-colored image of cell on CaP cement disc at 15 minutes, and (C,D) 30 minutes. (E) Correct fine-tuning of the regions of interest and iso-surface for cell volume analysis, (F) lowering of the cutting plane settings leads to a 2% overestimated volume, whereas (G) a too high setting leads to a 14% underestimated cell volume.

Calibration of the stereoscopic images is essential when using the Alicona MeX software algorithm for 3D SEM analysis. Bar sizes are automatically generated in the SEM acquisition, however, have to be transferred manually into the software module, so can causes errors in

the X and Y dimensions. Second, the tilting angle is set by hand and also transferred into the software. To our experience this angle should be optimized dependent on the height of the sample, and generally lies in between -15° and 15°. In the current study values of -5° and 5° were found optimal. Related to the angle, also the working distance will slightly vary and should be optimized by trial and error. An incorrect bar size, causes errors in the X and Y dimensions, whereas incorrect tilting angle and working distance provoke miscalculations and errors, all leading to inaccurate measurements and analysis. When optimal conditions are met, using the Alicona MeX software, relative basic software processing with easy to determine ROI and final volume of interest operations creates a final 3D model of the structure of interest.

A final remark would be the limitation of the technique as currently presented. Of course, by fixing and coating samples for SEM analysis still a technique is applied, which is destructive to samples, and thus longitudinal studies are not yet possible. However, such a shortcoming could be circumvented when using an environmental condition (e-SEM) approach, enabling true real-time measurements of spreading in time, and on the same sample.

## CONCLUSION

In conclusion, we can maintain both our initial hypotheses. It was well possible to reliably validate stereo-SEM measurements using standardized microspheres. Furthermore, 3D SEM stereo-imaging is a useful and accurate tool to visualize and analyze 3D cell parameters, such as spreading and cell volume in tissue-engineered constructs. Besides 3D visualization of the cells, quantitative assessment showed significant substrate dependency of cell spreading in time. Such quantification of cell spreading kinetics can be used for optimization of tissue engineering scaffold surface properties. However, further standardization of SEM image acquisition and 3D SEM software settings are still essential for 3D cell analysis.

## REFERENCES


1. Thurner, P., Müller, R., Raeber G., Sennhauser, U., Hubbell, J.A., 3D morphology of cell cultures: a quantitative approach using micrometer synchrotron light tomography. Microsc ResTech. 2005;66:289.
2. Weiss, P., Obadia, L., Magne, D., Bourges, X., Rau, C., Weitkamp, T., Khairoun, I., Bouler, J.M., Chappard, D., Gauthier, O., Daculsi, G., Synchrotron X-ray microtomography (on a micron scale) provides three-dimensional imaging representation of bone ingrowth in calcium phosphate biomaterials. Biomaterials. 2003;24:4591.
3. Choi, W., Fang-Yen, C., Badizadegan,K., Oh, S., Lue, N., Dasari, R.R., Feld, M.S., Tomographic phase microscopy, Nat Methods. 2007;9:717.
4. Zeng, P., Inkson, B.J., Rainforth, W.M., Stewart, T., 3D surface reconstruction and FIB microscopy of worn alumina hip protheses. J Phys Conf Ser. 2008;126, 012044.
5. Ostadi, H., Jiang, K., Prewett, P.D., Characterisation of FIB milling yield of metals by SEM stereo imaging technique. Microelectron Eng. 2009;86:1021.
6. Weibel, E.R., Kistler, G., Scherle, W.F., Practical stereological methods for morphometric cytology. J Cell Biol. 1966;30:23.
7. Cripps, J.B.F., Sang, H., Stereo Height Measurements in Scanning Electron Microscopy. Rev Sci Instrum. 1970;41:1825.
8. Samak, D., Fisher, A., Rittel, D., 3D Reconstruction and visualization of microstructure surfaces from 2D images. Annals of the CIRP. 2007;56:149.
9. Marschall,H.U., Danzer, H., Three-dimensional analysis of decorated ceramic fracture surfaces by automatic stereophotogrammetry. J. Am. Soc. 2000;83:223.
10. Pourchou, J.-P., Boivin, D., Beauchêne, P., Besnerais Le, G., Vignon, F., 3D reconstruction of rough surfaces by SEM stereo imaging., Mikrochim Acta 139, 135, 2002.
11. Ponz, E., Ladaga, J.L., Bonetto, R.D., Measuring surface topography with scanning electron microscopoy. I. EZEImage: A program to obtain 3D surface data. Microsc Microanal. 2006;12:170.
12. Chan, E., Darendeliler, M.A., Physical properties of root cementum : Part 5. Volumetric analysis of root resorption craters after application of light and heavy orthodontic forces. Am J Orthod Dentofac. 2005;127:186.
13. Nichols, A.B., Lange, D.A., 3D surface image analysis for fracture modeling of cement-based materials. Cement Concrete Res. 2006;36:1098.
14. Manelli, A., Sangiorgi, S., Binaghi, E., Raspanti, M., 3D analysis of SEM images of corrosion casting using adaptive stereo matching. Microsc Res Techniq. 2007;70:350.

15. Schroettner, H., Schmied, M., Scherer, S., Comparison of 3D surface reconstruction data from certified depth standards obtained by SEM and an Infinite Focus Measurement Machine (IFM). Microchim Acta. 2006;155:279.
16. Tomes, C., Jones, J.T., Carr, C.M., Jones, D., Three-dimensional imaging and analysis of the surface of hair fibers using scanning electron microscopy. Int J Cosmetic Sci. 2007;29:293.
17. Tang X., Rooij de, M.R., Duynhoven van, J., Breugel van, K., Dynamic volume change measurements of cereal materials by environmental scanning electron microscopy and video microscopy. J Microsc. 2008;230:100.
18. Tang, X., Rooij de, M., Jong de, L., Volume change measurements of rice by environmental scanning electron microscopy and stereoscopy. Scanning. 2007;29:197.
19. Tan, L., Shaw, G., Sridharan, K., Crone, W.C., Effects of oxygen ion implantation on wear behavior of NiTi shape memory alloy. Mech Mater. 2005;37:1059.
20. Barranco, V., Escudero, M.L., García-Alonso, M.C., 3D, chemical and electrochemical characterization of blasted TI6Al4V surfaces: Its influences on the corrosion behavior. Electrochim Acta. 2007;52:4374.
21. Anderson, R.K., Anderson, E., Shakir, L., Glover, S.C., Image analysis of extracellular matrix topography of colon cancer cells, Microscopy and Analysis. 2006;20(4):5.
22. Marending, M., Luder, H.U., Brunner, T.J., Knecht, S., Stark, W.J., Zehnder, M., Effect of sodium hypochlorite on human root dentine – mechanical, chemical and structural evaluation. Int Endod J. 2007;40:786.
23. Raspanti M., Binaghi, E., Gallo, I., Manelli, A., A vision-based, 3D reconstruction technique for scanning electron microscopy: direct comparison with atomic force microscopy, Microsc Res Tech. 2005;67:1.
24. Lyroudia, K.M., Dourou, V.I., Pantelidou, O.C., Labriandidis, T., Pitas, I.K., Internal root resorption studied by radiography, stereomicroscope, scanning electron microscope and computerized 3D reconstructive method. Dent Traumatol. 2002;18:148.
25. St-Pierre, J.-P., Gauthier, M., Lefebvre, L.-P., Tabrizian, M., Three-dimensional growth of differentiating MC3T3-E1 pre-osteoblasts on porous titanium scaffolds. Biomaterials. 2005;26:7319.
26. Smith, I.O., McCabe, L.R., Baumann, M.J., MC3T3-E1 osteoblast attachment and profileration on porous hydroxyapatite scaffolds fabricated with nanophase powder. Int J Nanomed. 2006;1:189.

# CHAPTER 5

# Resolution, sensitivity, and *in vivo* application of high-resolution computed tomography for titanium-coated polymethylmethacrylate (PMMA) dental implants

**Vincent M.J.I. Cuijpers, Jakub Jaroszewicz, Anil Sukumaran, Abdullah Al Farraj Alsosari, X. Frank Walboomers, John A. Jansen.**

**Clin Oral Implants Res. 2014 Feb;25:359-365.**

## INTRODUCTION

In current dentistry, titanium implants are often used. The success rate of an implant is characterized by the presence of direct contact between the implant surface and surrounding bone. The bright-field microscopy of histological stained slices remains the most frequently used tool for qualitative and quantitative evaluation of the bone response to an implant material in preclinical studies. Other conventional methods such as transmission electron microscopy (TEM), scanning electron microscopy (SEM) and atomic force microscopy (AFM) are available to study the bone-implant interface. Likewise, such two-dimensional analysis techniques are not completely representative for the whole specimen. As a result, also computed tomography (CT) is used frequently as a non-invasive non-destructive three-dimensional (3D) method to study radiopaque structures. On a microscopical level, the micro-CT technique is useful to determine bone volume and bone structural parameters.[1-3] Still, the micro-CT technique for research approaches in bone has three major shortcomings. First, micro-CT systems contain various limitations, which restrain the image reconstruction and final quantification.[4-6] Reconstruction artifacts, reconstruction center errors, mechanical imperfections (such as specimen axis wobble and rotation axis misalignment), and beam hardening can occur. Some of the limitations can be corrected using software algorithms, for example, for beam hardening and ring reduction.[7-9] The occurrence of scattering at the titanium implant-bone interface is a second problem. For research purposes, scattering can be greatly reduced when polymer implant materials are used, which are equipped with a titanium surface coating.[4] The third limitation is the resolution of conventional micro-CT, which is inferior to conventional two-dimensional (2D) microscopic images. To overcome these problems, higher spatial resolution and contrast sensitivity are required. Possibly, this can be achieved using CT systems at sub-micron resolution, such as synchrotron-CT, SEM based nano-CT instruments, and stand-alone tube-based nano-CT systems.[6,8] However, comparative studies of the 3D bone-implant interface area between the micro- and nano-CT

approaches have not been performed yet.
In view of the above-mentioned facts, the goal of this study was dual. Firstly, it was aimed to determine the spatial resolution and sensitivity of micro- versus nano-CT using standardized samples composed of well-defined synthetic microspheres embedded in matrices of varying X-ray absorption coefficients. Secondly, the objective was to validate the micro- versus nano-CT technique *in vivo*. For this purpose, titanium-coated polymethylmethacrylate (PMMA) implants were placed in the mandible of Beagle dogs, a frequently used model for biomedical implant interface studies.[10,11] After harvesting and fixing the biological specimens, *ex vivo* micro-CT and nano-CT was performed, and compared to descriptive histology and histo-morphometry.

## MATERIALS AND METHODS

### Standardized nano- and microsphere samples

Standardized polymethacrylate (PMA) poly(1-phenylethane-1,2-diyl), polystyrene (PS), silicon dioxide ($SiO_2$) (all Fluka, Buchs, Switzerland), and titanium dioxide ($TiO_2$) (Corpuscular, Cold Spring, NY) nano- and microspheres of different sizes were used to determine the spatial resolution of the used micro- and nano-CT systems. The selected spheres ranged in size from 500 nm to 100 µm. The nano- and microsphere density (g/cm$^3$) and solid content (%WT) data were used to create a uniform solution. The particle solution ranged from 3.5 * $10^4$ of the 100 µm spheres, up to 1.3 * $10^{12}$ of the 500 nm spheres, per milliliter (Table 1). Subsequently, 100 µl of the sphere solution was centrifuged 5 min, at 4.8 * $10^3$ rpm. The supernatant was removed and the spheres were dried overnight at 37°C. Thereafter, the spheres were mixed with respectively silicone rubber and calcium-phosphate cement (CaPC) matrices.
Silicone rubber samples were created as follows. Each sphere type was mixed with a total volume of 0.7 ml of silicone compound (Elastosil RT 601B and Elastosil RT 601A, ratio 1:20; Wacker Silicones, Riemerling, Germany) and placed in an Eppendorf tube (Eppendorf

AG, Hamburg, Germany). After overnight polymerization at 37°C, the silicone samples were removed from the tubes.
CaPC consisted of 0.5 g calcium-phosphate mixture (85% α-tri-calcium phosphate (Cam Bioceramics B.V., Leiden, The Netherlands), 10% $CaHPO_4$ (Sigma, St. Louis, MO) and 5% $HCa_5O_{13}P_3$ (J.T. Baker Chemical Co, Phillipsburg, NJ) was blended for 20 s with each type of sphere. Thereafter, 190 µl of 2% $Na_2HPO4$ (Merck, Darmstadt, Germany) solution was added and thoroughly mixed for 20 s. The thus obtained deformable paste was placed in cylindrical Teflon moulds, and the CaPC was hardened overnight at 37°C.

**Table 1**. Composition, size, density, solid content, and particles per milliliter of micro- and nanospheres.

| Particle composition | Particle size (µm/nm) | Density ($g/cm^3$) | Solid content (% WT) | Particles/ml |
|---|---|---|---|---|
| Polystyrene | 100 µm<br>10 µm<br>1 µm | 1.05<br>1.05<br>1.05 | 2<br>2<br>2 | $3.5 * 10^4$<br>$3.5 * 10^7$<br>$3.5 * 10^{10}$ |
| Polymethacrylate | 100 µm<br>50 µm<br>20 µm | 1.19<br>1.19<br>1.19 | 10<br>10<br>10 | $2.0 * 10^5$<br>$1.6 * 10^6$<br>$2.5 * 10^7$ |
| $SiO_2$ | 1 µm<br>500 nm | 1.8-2<br>1.8-2 | 2.5<br>5 | $7.9 * 10^{10}$<br>$1.3 * 10^{12}$ |
| $TiO_2$ | 1 µm<br>500 nm | 2.2<br>2.2 | 2.2<br>2.5 | $8.1 * 10^{10}$<br>$7.3 * 10^{11}$ |

Both silicone rubber and CaPC samples were finally trimmed to a fixed volume of approximately 8 $mm^3$ for further micro- and nano-CT analysis.
To confirm sphere size, surface texture and distribution of the nano- and micro-spheres in both samples, SEM analysis was performed. The specimens were coated using a 30 nm thin layer of Au-Pd, using a high resolution sputter coater (208HR, Cressington Scientific, Watford, United Kingdom), and imaged using a Field Emission SEM (JSM 6330F, JEOL Corporation, Tokyo, Japan) operated at an accelerating voltage of 3 keV.

## Implant design

Custom-made polymethylmethacrylate (PMMA) implants (3.2 mm in Ø by 4 mm in length) were used. All implants were coated with titanium (Ti), using a radio frequency magnetron-sputtering unit (Edwards ESM 100, Crawford, United Kingdom). During the sputtering process, a commercially pure Ti target was used. The Ti target was sputter cleaned before deposition. The target was considered clean when the plasma turned from pink to blue, resulting from blue light emitting Ti in the plasma. Pressure was kept at 5.0 x $10^{-3}$ mbar using Argon gas, and the power was set at 100 W. Thereafter, the PMMA implants were sputter coated for 3x5 min, with a rotation of the implant of 120° before each time step to ensure homogenous coverage. The coating thickness was determined to be 10 nm using a Nanoscope IIIA atomic force microscope (Veeco Industries, Santa Barbara, CA). Before use in the animal study, the implants were autoclaved for 15 min at 121°C.

## Implantation procedure and implant retrieval

Ten adult Beagle dogs (1-2 years old, weight 10-12 kg) were used. The research protocol was approved by the ethical committee of King Saud University (Riyadh, Kingdom of Saudi Arabia) and national guidelines for care and use of laboratory animals were observed. The animals were anesthetized and after intubation, general anesthesia was maintained with Isoflurane® (Rhodia Organique Fine Limited, Avonmouth, Bristol, UK).

In a first surgical session, three premolars (P2-4) were delicately removed in the left side of the mandible. Healing time for the extraction sockets was three months.

In a second surgical session, in the left side of the mandible of the10 Beagle dogs, 10 implants were placed, i.e. one implant per dog. To reduce peri-operative bleeding, local anesthesia was performed with 2% lidocaine-containing epinephrine (1:100,000). Before surgery the local mucosa was cleaned with a 10% Povidone-iodine and incised. A bone defect of 3.2 mm in diameter by 8 mm in depth was created by drilling, using low rotational drill speeds (800-1200 rpm) and

continuous external cooling with saline. The implant was placed press-fit at the bottom of the defect. Finally, the gingiva was sutured and all implants were left in a submerged position for an implantation time of 4 weeks. After surgery, Finadyne® (Schering corporation, Kenilworth, NJ) and a broad-spectrum antibiotic (Gentamycin, SPIMACO, Qassim, Saudi Arabia, 4 mg/kg body weight intramuscularly) was given for 7 days.

At the end of the implantation period, the animals were euthanized by an overdose of Pentobarbital and the implants with surrounding tissue were harvested. The specimens were fixed in 10% neutral buffered formalin solution with subsequent dehydration in a graded series of ethanol (70-100%). Thereafter, specimens were hemi-sectioned. The top part was used for micro-CT and subsequent nano-CT analysis. For nano-CT, it was necessary to reduce the size of the specimen further, as the maximum size for nano-CT specimens was approximately 2.5 x 2.5 x.2.5 mm. Sectioning and reduction of the specimen was done using a Leica EM TXP target preparation device (Leica Microsystems, Wetzlar, Germany), with a 300 µm diamond coated disc cutter blade. The bottom part was used to prepare histological sections.

## Micro- and nano-computed tomography

The standardized samples, as well as the implant samples, were scanned using the Skyscan micro-CT system model 1172 and nano-CT system model 2011 V 2.3 (Skyscan, Kontich, Belgium). Selection of these systems was based on the minimal image pixel size, respectively 0.8 µm and 150 nm.[12]

The SkyScan 1172 system was operated at 100 kV and 100 µA and the exposure time was set to 260 ms. Scanning was performed by 180° rotation around the vertical axis and with rotation step of 0.5°. During scanning a 0.5 mm aluminium filter was used. The necessary field of view (FOV) for the standardized and implant samples was determined, resulting in an optimal image pixel size of 3 and 4.37 µm, respectively. Subsequently, the projected images were reconstructed in 2000 x 2000 pixel sized cross-section images using the Skyscan NRecon® cone beam reconstruction software with beam-hardening compensation

and ring artifact correction set to 30% and 15, respectively. For nano-CT, samples were scanned 180° around the vertical axis in rotation steps of 0.3 degrees. The X-ray source was set to a voltage of 40 kV and current of 180 µA. The exposure time was 2.0 s using a detector of 1280x1280 pixels. Raw data were reconstructed with the NRecon® cone beam reconstruction software. Images with pixel size of 500 nm and 2 µm were generated from the standardized and implant samples, respectively. As a results, the FOV was 2.56 x 2.56mm; i.e. capable to include the entire specimen.

### Micro- and nano-computed tomography analysis

Skyscan CTAn V.1.11 software was used for segmentation, registration and quantification of all reconstructed images. The obtained images of the standardized samples were used to determine resolution and sensitivity limit. The digital ruler of the CT-An software program was used to measure the smallest visible sphere present in 10 representative images, with known image pixel size. The variation in radiodensity was detected using the gray-scale histogram (range 0-255) values of the complete data set of the standardized sample.
For the implant samples, bone regeneration routinely is detected in a 500 µm zone from the surface of the implant.[13,14,15] Thus, in 2D cross sections of the reconstructed CT images, a standardized threshold of the gray-values for bone within the total data was set. Then, the bone area (BA) percentage was analyzed in the region of interest (ROI) zone of 500 µm surrounding the implant.
Further, for the complete 3D reconstructions the bone volume (BV) percentage was calculated in a fixed volume of interest (VOI) zone of 500 µm surrounding the implant surface with a depth of 2 mm. Also, the bone-to-implant contact (BIC) percentage was calculated using an algorithm including automated adaptive segmentation of the bone and morphology-based operations as dilatation.

## Histology and histomorphometry

The bottom part of the specimens was embedded in epoxy resin (EpoFix®, Struers, Rødovre, Denmark). After polymerization, thin sections of the implants were prepared using a modified SP1600 inner circular sawing microtome[16] (Leica) and stained with methylene blue and basic fuchsin. The sections were made in a cross-sectional direction perpendicular on the longitudinal implant axis. Acquisition of microscopical images and histological evaluation was performed using an automated light microscope (Axio Imager Z1, Carl Zeiss Micro Imaging GmbH, Göttingen, Germany). With the aid of the digital image processing software module MosaiX of the Axiovision V4.6.3. software package combined with a motorized microscope stage, a high resolution image (0.27 µm pixel size) of the complete ROI was obtained.
For final image quantification, a computer-based image analysis system (Leica QWIN Pro image analysis software, Leica Imaging Systems, Cambridge, UK) was used. For calibrating the Leica QWIN quantification program for further histomorphometrical analysis of the microscopic images, the known pixel size was imported. The ROI's of corresponding planes of the 2D micro-CT and histological slices were quantified in $\mu m^2$. The BA percentage was determined in a 500 µm ROI zone from the implant surface, and the BIC percentage was calculated using the perimeter of the implant and total of contact parts of bone tissue with the implant surface.

## Statistical analysis

The mean gray-values of both silicone and CaPC matrices when using micro- and nano-CT were compared using an unpaired *t*-test (InStat, version 3.05, GraphPad Software Inc., San Diego, CA). Statistical analysis of BA, BV and BIC percentage measurements of the different samples using both CT techniques and histology were conducted using paired *t*-tests (SPSS version 20, IBM Statistics, Armonk, NY). For repeated testing of BA and BIC, Bonferroni correction was applied.

# RESULTS

## Standardized samples

Using SEM, all four types of micro- and nano-spheres were detected by visual inspection and observed to be distributed evenly in both silicone rubber and CaPC matrices. The rough surface of CaPC made it more difficult to distinguish 1 µm and 500 nm spheres in CaPC (Figure 1).

The micro-CT system allowed the detection of the 10 and 100 µm microspheres inside the silicone rubber as well as CaPC matrix. On the other hand, due to limitations in spatial resolution, the one-micron spheres could only be detected using the nano-CT system, while the 500 nm spheres could not be detected at all.

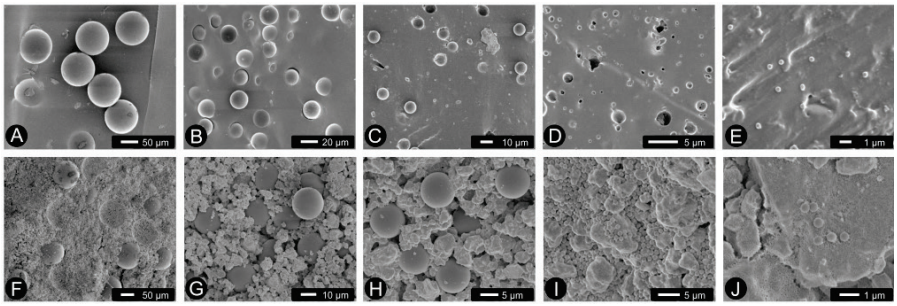


**Figure 1.** Scanning electron micrographs of solitaire nano- and microspheres in respectively, silicone rubber containing (A) 100 µm PS, (B) 20 µm PMA, (C) 10 µm PS, (D) 1 µm $SiO_2$ and (E) 500nm $SiO_2$ spheres, and calcium phosphate matrix containing (F) 100 µm PMA, (G) 20 µm PMA, (H) 10 µm PS, (I) 1 µm $SiO_2$ and (J) 500 nm $SiO_2$ spheres.

The sensitivity limits were also determined. After normalization, the gray-value ranges in the histograms of the radio-absorption in micro-CT for silicone matrices were 31-124 (mean 49.0 ± 19.3) and 55-187 (mean 104.3 ±21.7) for CaPC matrices. When using nano-CT, gray-value ranges in the radio-absorption histograms were 39-138 (mean 55.4 ± 25.7) for silicone matrices and 50-187 (mean 89.3 ± 25.8) for CaPC matrices.

Due to the more uniform radiodensity of the silicone matrix, the microspheres could be easily discriminated in the obtained histogram. The more irregular texture and variation in radiodensity in the CaPC allowed for less sensitivity (Figure 2).
There was no significant difference of the mean gray-values of both silicone and CaPC samples when using micro- and nano-CT. *p*-values were respectively 0.804 and 0.593 for silicone and CaPC.

## Implants

At the end of the 4-week implantation time, one implant was found to be lost. All other implants could be harvested, and there were no visible signs of an excessive inflammatory response or adverse tissue reaction.

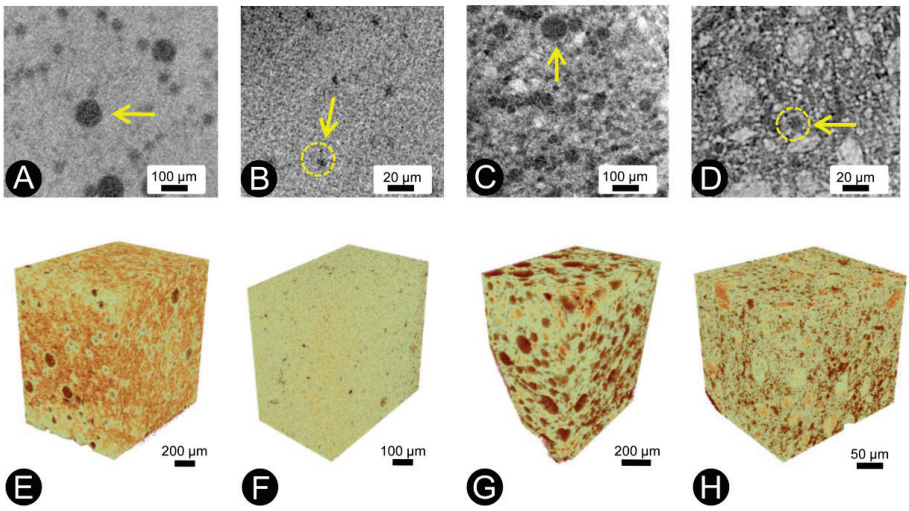


**Figure 2.** (A-D) Single 2D micro-CT X-ray images and (E-H) 3D volume reconstruction models of (A,B,E,F) silicone and (C,D,G,H) calcium phosphate cement matrices containing, respectively, (A,C,E,G) Ø 100 µm and (B,D,F,H) Ø 10 µm microspheres.

## Micro- and nano-computed tomography evaluation

Using micro-CT, the total field of view (8.7 mm), containing the implant with a surrounding 500 µm wide bone area, could be analyzed at 4.37 µm resolution in terms of pixel size. No scattering of the thin Ti layer applied on the PMMA implant surface was found. The PMMA implant and the bone were visible at high magnification (Figure 3A, B). Morphological detail of the bone was restricted to overall structure including the shape of the trabeculae. The extraction of the 3D VOI from the total sample is shown in Figure 4A, B.
Using nano-CT, even at 2 µm resolution, the limited FOV (2.56 mm) included the entire ROI. Similar to micro-CT, no scattering artifacts were found. Compared with micro-CT, in the nano-CT, a much higher histomorphological detail of bone and other tissues could be detected (Figure 3D, E). Even the structure of the osteons and small blood vessels was clearly visible (Figure 3G).

For both CT techniques and histology, the BA, BIC, and BV percentage results and-obtained paired *t*-test data are listed in Table 2.

**Table 2.** Mean and SD of the bone area (BA), bone-implant-contact (BIC) and bone volume BV percentage in micro-CT, nano-CT and histology. Shown are number of measurements (N), compared groups, mean difference (MD), 95% confidence interval (CI) and *p*-value for BA, BIC and BV.

| | | T-test | | | |
|---|---|---|---|---|---|
| | Mean ± SD | N | Compared groups | MD (95% CI) | P-value |
| BA micro-CT | 86.3 ± 6.8 | 3 | BA micro-CT vs. BA nano-CT | 21.4 (2.3, 40.5) | 0.040 |
| BA nano-CT | 65.5 ± 11.0 | 7 | BA micro-CT vs. BA histology | 0.2 (-3.0, 3.5) | 0.869 |
| BA histology | 84.1 ± 8.0 | 3 | BA nano-CT vs. BA histology | -18.3 (-39.1, 2.6) | 0.064 |
| BIC micro-CT | 84.0 ± 4.0 | 3 | BIC micro-CT vs. BIC nano-CT | 21.5 (-0.1, 43.1) | 0.051 |
| BIC nano-CT | 62.8 ± 11.7 | 7 | BIC micro-CT vs. BIC histology | 0.3 (-4.4, 5.0) | 0.881 |
| BIC histology | 82.5 ± 5.9 | 3 | BIC nano-CT vs. BIC histology | -19.1 (-38,8, 0.5) | 0.052 |
| BV micro-CT | 81.4 ± 5.5 | 3 | BV micro-CT vs. BV nano-CT | 26.7 (-58.4, 111.8) | 0.157 |
| BV nano-CT | 55.4 ± 7.4 | | | | |

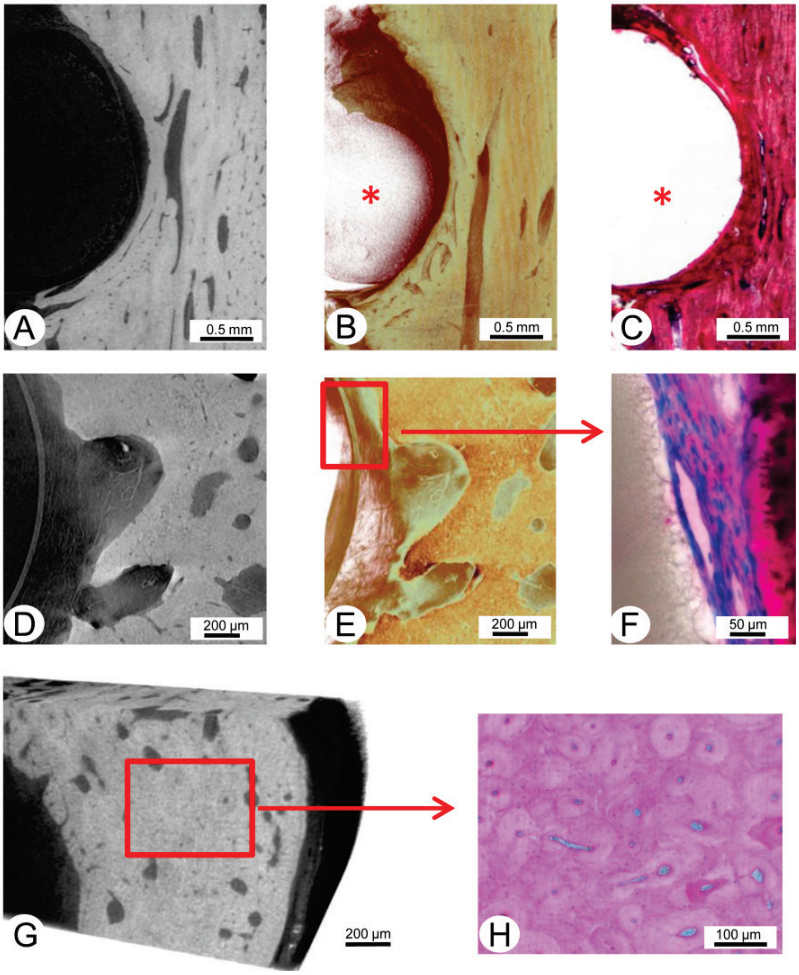


**Figure 3.** (A,B) Micro-CT analysis showing implant (*) and bone. (A) single 2D X-ray image at 3 µm resolution, (B) 4 $\mu m^3$ voxel sized 3D volume reconstruction and (C) corresponding histological stained microscopic slice at 50x magnification. (D,E) Nano-CT analysis showing (D) detailed 2D X-ray image with titanium-coated implant and bone part at 500 nm resolution and (E) corresponding 3D volume reconstruction at 500 $nm^3$ voxel size. (F) Blue-stained layers of stromal cells lining the pre-existing bone (red-pink) at the bone-implant (gray) surface at 400x magnification. Histological details of osteons in both (G) micro-CT and (H) histology at 100x magnification.

## Histological evaluation

Histological sections showed excellent preservation of the bone morphology when embedded in epoxy resin. Because of sample loss and tissue processing, 8 out of the 9 samples were finally suitable for final histological analysis. The outline of the Ti-coated PMMA implant was always visible. Pre-existing and newly formed bone was clearly visible. In areas where no bone contact existed, locally a thin layer of stromal cells was lining the implant interface (Figure 3F). Moreover, histological details as osteons and small blood vessels were clearly visible due to sub-micron resolution (Figure 3H).
Different bone cell types were clearly visible when using magnifications with pixel sizes up to 0.27 µm. Figure 4C,D visualizes the extraction of the 2D ROI from the histological stained slice for analysis. Quantification of the BA and BIC of the histological slices is listed in Table 2.

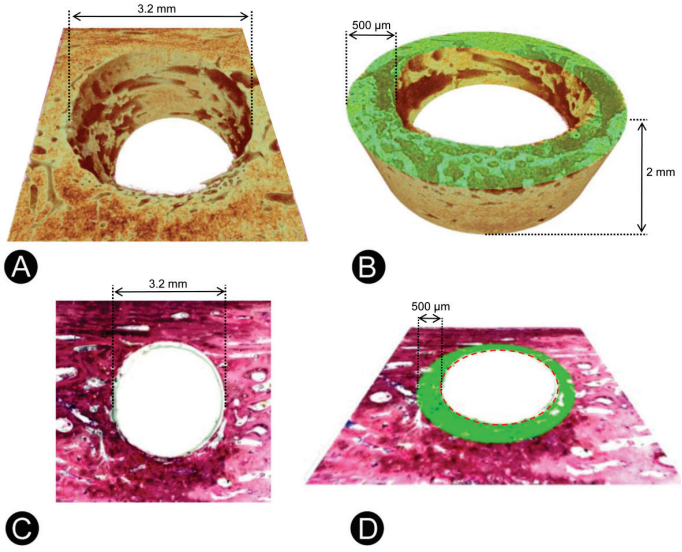


**Figure 4.** (A-D) Visualization and selection of bone area (BA) and bone-implant contact (BIC) in micro-CT and histomorphometry analysis. (A) 3D volume reconstruction of bone with transparent implant part, (B) selection of 3D VOI (500 µm width and 2 mm in height) extracted from the bone (BA in green, BIC in red), (C) histological stained slice part and corresponding (D) BA selection (green) and BIC (red).

### Comparative analysis of computed tomography and histomorphometric data

Statistical comparison of the micro-CT, nano-CT, and histomorphometric paired data, showed no significant difference in BA ($p$=0.869) and BIC ($p$=0.881) for micro-CT versus histology. In contrast, BA and BIC as assessed in nano-CT were always significantly lower compared to micro-CT ($p$=0.040 and $p$=0.064) as well as histology ($p$=0.051 and $p$=0.052). BV could not be determined in 2D histomorphometrical analysis. For BV, a significantly lower value was found in nano-CT compared with the micro-CT analysis. Notable was also the large diversity in standard deviations for nano-CT (from 35 up to 295%) compared with micro-CT and light microscopy.

## DISCUSSION

This study aimed to evaluate spatial resolution and sensitivity of micro- versus nano-CT, including a comparative validation of both techniques versus light microscopical imaging as the gold standard. Overall, it was found that nano-CT provided better resolution, which proved to result in a detail of observation close to histological assessment. However, in terms of quantification, micro-CT showed to result in a more reliable assessment of bone healing parameters matching histomorphometry. Although the image acquisition principles between nano- and micro-CT are similar, there are limitations in sample size. For nano-CT, the achievable volume-of-interest is smaller, which affects the reliability of the obtained data. In this case the measurement turned out to be too low. In addition, the individual measurements showed a large statistical scattering resulting in higher diversity of the standard deviations. Therefore, a direct comparison between both CT techniques reveals a more optimal resolution for nano-CT, but a superior capacity for quantification for micro-CT. Thus both techniques should be regarded as complementary on basis of detail and accuracy.

Considering the current study design, several remarks have to be made. First, the comparative steps were performed using standardized samples made of silicone rubber and ceramic material. This was done purposely, as these two matrices exhibit completely different radio absorption coefficients, hardness and texture. As a consequence, they provide the optimal means to assess resolution and sensitivity of the used CT systems. Resolution in nano-CT was found to be significantly better, but sensitivity appeared to be similar. Probably, the use of Synchrotron micro-CT with a high intensity monochromatic X-ray beam, combined with phase contrast-enhanced imaging, is a better approach to increase sensitivity and result in a better sensitivity.[17-19]

For the comparative evaluation of CT and histological imaging, Ti-coated PMMA implants were placed in the mandibles of Beagle dogs. This implant design was chosen as the most reliable model to quantify bone healing parameters, as the use of solid titanium implants affects the CT assessment negatively, due to electron-scattering artifacts.[4] Even when specific combined metal filters are used to reduce scattering at the implant surface.[5] A polymer implant behaves superior due to the diminished occurrence of X-ray scattering, while the surface coating of titanium serves as a close representation of a solid titanium implant. PMMA was chosen as the implant core because Perilli et al. reported that this polymer is very suitable to study structural parameters of human bone biopsies with micro-CT without obtaining undesirable artifacts.[20]
Besides these aspects related to the CT imaging, a second reason to apply a PMMA based implant was based on the ease of histological processing. Previously, it was shown that polycarbonate plastic implants, vapor-coated with a layer 120-250 nm of titanium, were applicable for implant research purposes. Such implants were integrated in rabbit bone at 12 weeks of implantation and subsequently could even be processed for electron microscopy.[21] Albrektsson and Hansson corroborated such results in a later study, using a 100 nm titanium or zirconium coating, which enabled light and electron microscopy to study the host bone response, in high detail up to protein attachment level.[22] Thus our current study followed such

principle as well. Because our implant was made of PMMA, for subsequent histological analysis, embedding in epoxy was preferable over routine MMA embedding.

The final validity of CT measurements was performed in comparison with such histological analysis. Of course, no direct comparison could be made as the implant was split in an upper part for CT and lower part for histology. Still, Britz et al.[23] showed that the matching of the same images, but acquired via different techniques, can also not always be performed at a high accuracy. Histological processing of the samples can result in minor loss of form; moreover, there will always be intrinsic differences in thickness and localization between histological sections in contrast to the CT reconstructed cross-sections. Others compared the use of micro-CT and histology for the evaluation of cortical bone structure and were capable to obtain a very close correlation between the three-dimensional micro-CT parameters versus two-dimensional histological sections.[24] Herein, we assumed that bone morphology was similar between upper (CT) and lower (histology) parts of the implant for regions less than 500 µm apart. The present study confirmed the correlation between micro-CT and histology for the analysis of bone parameters, as also had been determined earlier.[1,7] In contrast, the use of nano-CT was found to be less accurate, resulting in lower values compared with micro-CT and light microscopical histomorphometry. The explanation for this observation is that micro-CT is able to study larger samples (~centimeter range) compared with nano-CT (~millimeter range). In addition, when nano-CT is used at nanometer resolution, analysis of only a very limited VOI is possible. This will always result in over- or underestimation errors during quantification. As a second consequence, also the diversity of the standard deviation is large.

Only a very limited number of publications are available describing the use of stand-alone nano-CT systems for the analysis of bone tissue.[25,26] Salmon et al. explored the resolution limitations of nano- and micro-CT when studying the ultra structure of bone.[25] The juvenile murine fibula was chosen as a useful site for nano-CT imaging due to the requirements of a very small specimen size for attaining optimum resolution. A range of histomorphometric parameters was

generated including bone area, osteocyte lacuna characteristics, and cellular resorption and formation factors. Nevertheless, no validation of obtained parameters versus other measuring techniques was implemented.

Van Hove et al. studied the osteocyte morphology in human tibiae with a different bone mineral density (BMD) using confocal laser scanning microscopy (CLSM) and nano-CT.[26] The latter technique quantitatively determined 3D morphology and alignment of osteocytes and osteocyte lacunae in human proximal tibial bone with relatively low (osteopenic), medium (osteoarthritic), and high (osteopetrotic) BMD. Both CLSM and nano-CT demonstrated significant differences in osteocyte 3D morphology in all pathologies. Shape differences in terms of elongation and roundness were found, but there was little difference in cell size. On the other hand, statistical analysis showed a significant difference in the sizes of the osteocyte lacunae. As this study was carried out at cellular level, again limitations to sample size or VOI are less relevant compared to the current work.

In conclusion, this study showed that micro-CT analysis is an efficient tool to quantify bone healing parameters at the bone-implant interface, especially when using titanium-coated PMMA implants. Nano-CT is not suitable for such quantification, but reveals complementary morphological information rivaling histology.

## REFERENCES


1. Stoppie, N., Waerden van der, J-P., Jansen, J.A., Duyck, J., Wevers, M., Naert, I.E. Validation of microfocus computed tomography in the evaluation of bone implant specimens. Clinical Implant Dentistry and Related Research. 2005;7:87.
2. Chappard, C., Marchadier, A., Benhamou, C.L., Side-to-side and within-side variability of 3D bone microarchitecture by conventional micro-computed tomography of paired iliac crest biopsies. Bone. 2008;43:203.
3. Bonnet, N., Laroche, N., Vico, L., Dolleans, E., Courteix, D., Benhamou, C.L.,Assessment of trabecular bone microarchitecture by two different X-ray microcomputed tomographs: a comparative of the rat distal tibia using Skyscan and Scanco devices. Medical Physics. 2009;36:1286.
4. Shalabi, M.M., Wolke, J.G.C., Cuijpers, V.M.J.I., Jansen, J.A., Evaluation of bone response to titanium-coated polymethul methacrylate resin (PMMA) implants by X-ray tomography. Journal of Materials Science. Materials in Medicine. 2007;18:2033.
5. Cha, J-Y., Lim, J-K., Song, J-W., Sato, D., Kenmotsu, M., Inoue, T., Park, Y-C., Influence of the length of the loading period after placement of orthodontic mini-implants on changes in bone histomorphometry: microcomputed tomographic and histologic analysis. The International Journal of Oral & Maxillofacial Implants. 2009;24:842.
6. Stock, S.R., Micro-Computed Tomography, Methodology and Applications, 1st edition, 2009:85. Baca Raton: CRC Press, Taylor & Francis Group.
7. Stoppie, N., Wevers, N.,Naert, I.E., Feasibility of detecting trabecular bone around percutaneous titanium implants in rabbits by *in vivo* microfocus computed tomography. Journal of Microscopy. 2007;228:55.
8. Banhart, J., Advanced Tomographic Methods in Materials Research and Engineering, 1st edition, 2008:145. Oxford: Oxford University Press.
9. Zou, W., Hunter, N., Swain, M.V., Application of polychromatic μCT for mineral density determination. Journal of Dental Research. 2011;90:18.
10. Calvo Guirado, J.L., Ortiz Ruiz, A.J., Negri, B., López Marí, L., Rodriguez Barba, C., Schlottig, F., Histological and histomorphometric evaluation of immediate implant placement on a dog model with a new implant surface treatment. Clinical Oral Implants Research. 2009;21:308.
11. Junker, R., Manders, P.J.D., Wolke, J., Borisov, Y., Jansen, J.A., Bone reaction adjacent to microplasma sprayed calcium phosphate-coated oral implants subjected to occlusal load, an experimental study in the dog. Clinical Oral Implants Research. 2001;22:135.
12. Sasov, A., Liu, X., Salmon P.L., Compensation of mechanical inaccuracies in micro-CT and nano-CT. In: Stock S.R., eds. Developments in X-ray Tomography VI, Proc. Of SPIE 2008;7078:1.

13. Schouten, C., Meijer, G.J., Beucken van den, J.J., Spauwen, P.H., The quantitative assessment of peri-implant bone responses using histomorphometry and micro-computed tomography. Biomaterials. 2009;30:4539.
14. Junker, R., Manders, P.J.D., Wolke, J., Borisov, Y., Braceras, I., Jansen, J.A., Bone-reaction adjacent to microplasma sprayed CaP-coated oral implants subjected to occlusal load; an experimental study in th dog. Part III: Marginal bone and soft tissue healing-long term results. Clinical Oral Implants Research. 2010;21:189.
15. Junker, R., Manders, P.J.D., Wolke, J., Borisov, Y., Jansen, J.A., Bone reaction adjacent to microplasma sprayed CaP-coated oral implants subjected to occlusal load, an experimental study in the dog. Part I: Short-term results. Clinical Oral Implants Research. 2010;21:1251.
16. Lubbe van der, H.B., Klein, C.P., Groot de, K., A simple method for preparing thin (10 micron) histological sections of undecalcified plastic embedded bone with implants. Stain Technology, 1988;63:171.
17. Stiller M., Rack, A., Zabler, S., Goebbels, J., Dalügge, O., Jonscher, S., Knabe S., Quantification of bone tissue regeneration employing ß-tricalcium phosphate by three-dimensional non-invasive synchrotron micro-tomography - A comparative examination with histo-morphometry. Bone. 2009;44:619.
18. Yue, S., Lee, P.D., Poologasundarampillai, G., Yao, Z., Rockett, P., Devlin, A.H., Mitchell, C.A., Konerding, M.A., Jones J.R., Synchrotron X-ray microtomography for assessment of bone tissue scaffolds. Journal of Materials Science. Materials in Medicine. 2010;21:847.
19. Appel, A., Anastasio, M.A.,Brey, E.M., Potential for imaging engineered tissues with X-ray phase contrast. Tissue Engineering: Part B. 2011;17:321.
20. Perilli, E., Baruffaldi, F., Visentin, M., Bordini, B., Traina, F., Cappello, A., Viceconti, M.J., MicroCT examination of human bone specimens: effects of polymethylmethacrylate embedding on structural parameters. Journal of Microscopy. 2007;225:192.
21. Linder, L., Albrektsson, T., Brånemark, P.I., Hansson, H.A., Ivarsson, B., Jönsson, U.,Lundström, I., Electron microscopic analysis of the bone – titanium interface. Acta Orthopaedica Scandinavica. 1983;54:45.
22. Albrektsson, T.,Hansson, H.A., Interface analysis of titanium and zirconium bone implants. Biomaterials. 1985;6:97.
23. Britz, H.M., Jokihaara, J., Leppanen, O.V., Jarvinen, T.,Cooper, D.M., 3D visualization and quantification of rat cortical bone porosity using a desktop micro-CT system: a case study in the tibia. Journal of Microscopy. 2010;240:32.
24. Particelli, F., Mecozzi, L., Beraudi, A., Montesi, M., Baruffaldi, F., Viceconti, M., A comparison between micro-CT and histology for the evaluation of

cortical bone: effect of polymethylmethacrylate embedding on structural parameters. Journal of Microscopy. 2011;245:302.

25. Salmon, P.L., Sasov, Y.A., Application of nano-CT and high-resolution micro-CT to study bone quality and ultrastructure, scaffold biomaterials and vascular networks. In: Qin, L., Genant H.K., Griffith, J. & Leung K-S., eds. Advanced Bioimaging Technologies in Assessment of the Quality of Bone and Scaffold Materials. Techniques and Applications. 1st edition, 2007:323. Heidelberg: Springer Verlag Berlin.
26. Hove van, R.P., Nolte, P.A., Vatsa, A., Semeins, C.M., Salmon, P.L., Smit, T.H., Klein-Nuland, J., Osteocyte morphology in human tibiae of different bone pathologies with different bone mineral density – Is there a role for mechanosensing ? Bone. 2009;45:321.

# CHAPTER 6

# Micro-computed tomographical imaging of soft biological materials using contrast techniques

Kaeuis A. Faraj, Vincent M.J.I. Cuijpers, Ronnie G. Wismans, X. Frank Walboomers, John A. Jansen, Toin H. van Kuppevelt, Willeke F. Daamen.

Tissue Eng Part C Methods. 2009 Sep;15(3):493-499.

## INTRODUCTION

The development of high-resolution X-ray computed tomography (micro-CT) started in the early 1980s and has been used extensively to study the structure and architecture of bone tissue.[1–5] Various parameters can be calculated with this technique, depending on the computational capability of the hardware and software. In addition, micro-CT is basically a non-destructive technique.[6]

Researchers have employed micro-CT in the field of tissue engineering.[6–8] The versatility of micro-CT has been demonstrated in the evaluation of scaffolds, because this single technique is capable of characterizing multiple aspects of the scaffolds.[6] Micro-CT enables to get three-dimensional (3D) images of the internal area of a sample, and a detailed 3D view of pores at any depth.[9] Further, different parameters may be calculated such as porosity, surface area to volume ratio, pore size, pore wall thickness, anisotropy, cross-sectional area, and permeability.[6] Micro-CT has been used for several polymer-based scaffolds that hold sufficient intrinsic contrast. For example, the internal geometry, pore network, and pore interconnectivity of poly-ε-caprolactone scaffolds have been determined;[10] in addition, the porosity, surface area to volume ratio, and interconnectivity of scaffolds made from a copolymer of poly ethylene glycol, poly-ε-caprolactone, and polylactic acid have been evaluated.[6] Quantification of microarchitectural parameters, including volume fraction, density, thickness, spacing, and degree of anisotropy, of porous poly(L-lactide-co-DL-lactide) scaffolds with axially oriented macroporosity and random microporosity has also been reported.[7]

Scaffolds based on natural proteins such as collagen do not have the intrinsic X-ray attenuation capacity to be imaged by 3D micro-CT. Consequently, additional contrast has to be imposed upon such scaffolds. The aim of this work was to introduce micro-CT for proteinaceous scaffolds as exemplified by collagen, and to compare results with those obtained by scanning electron microscopy and light microscopy. Two structurally different scaffold types were tested, one with round pores and one with unidirectional lamellae. Different heavy metal contrast agents were assessed to find useful radio-opaque

contrast agents that allow the use of micro-CT imaging for collagen scaffolds in particular and protein-based scaffolds in general.

## MATERIALS AND METHODS

### Collagen scaffolds

Collagen scaffolds were prepared as previously described.[11] Briefly, a collagen suspension was prepared by incubation of 0.9% purified insoluble type I collagen in 0.25 M acetic acid at 4°C for 16h. The suspension was homogenized on ice, followed by deaeration by centrifugation at 525 *g*, resulting in the collagen suspension to be used for the scaffold.
Scaffolds with round pores were prepared by freezing 4 mL of collagen suspension per well of a six-well culture plate at -20°C. Scaffolds with unidirectional lamellae connected by thin struts (about 1–2 μm) were prepared using a temperature gradient between liquid nitrogen (-196°C) and ambient temperature. This induces a temperature gradient starting from the side of $N_2$ (l) toward the ambient temperature, thus producing lamellar structures. The principle is essentially the same as described by Schoof et al.[12] The frozen collagen suspensions were then lyophilized to obtain dry scaffolds. Samples of approximately 5x5x5 mm were used for analysis.

### Scaffold preparation for imaging

To obtain collagen scaffolds with appropriate contrast for micro-CT imaging, different contrast agents were used: osmium tetroxide ($OsO_4$), uranyl acetate ($UO_2(CH_3COO)_2{\cdot}2H_2O$), and lead citrate ($(C_6H_5O_7)_2Pb_3$. The stains were selected based on contrast agents used in electron microscopy: first, because they bind to biological materials, and, second, because by being heavy metals they have the ability to apply contrast. In particular, uranyl acetate and lead citrate are used to stain collagen for electron microscopy.[13] All scaffolds were treated

with different contrast agents in distilled water at 22°C, followed by three 20 min washings in distilled water. The applied procedures were as follows:

(1) 1% (w/v) osmium tetroxide for 26 h;
(2) 1% (w/v) osmium tetroxide for 6 days;
(3) 1% (w/v) lead citrate for 24 h;
(4) 2% (w/v) uranyl acetate for 24 h;
(5) 2% (w/v) uranyl acetate for 24 h, followed by three washings in distilled water for 20 min and 1% (w/v) lead citrate for 24 h;
(6) 1% (w/v) osmium tetroxide for 6 days, followed by three washings in distilled water for 20 min and 1% (w/v) lead citrate for 24 h;
(7) 1% (w/v) osmium tetroxide for 6 days, followed by three washings in distilled water for 20 min and 2% (w/v) uranyl acetate for 24 h;
(8) 1% (w/v) osmium tetroxide for 6 days, rinsed five times for 15 min with distilled water, followed by 1% (w/v) thiocarbohydrazide for 1h, rinsed five times for 15 min with distilled water, and 1% osmium tetroxide for 1 h (treatment according to Kelly et al.[14] for enhanced contrast intensity due to increased binding of osmium tetroxide in a post-incubation step[15]).

After each procedure, scaffolds were dehydrated in an ascending series of ethanol and critical point dried in a Polaron E3000 apparatus (Quorum Technologies, Newhaven, UK) using liquid $CO_2$.

## CT-scan imaging and data analysis

The samples were scanned using the SkyScan 1072 Micro-CT (SkyScan, Kontich, Belgium) with Feldkamp cone-beam reconstruction. NRecon V1.4.0 software was provided by SkyScan. The sample was mounted on a rotation stage in front of the X-ray source with Optosil (Heraeus, Armonk, NY). A high-resolution charge-coupled device, with a resolution of 1024x1024 pixels, was applied to detect the X-rays from the scanned samples and to store data. The following micro-CT settings were applied based on a pilot experiment: (1) the X-ray source was set to 47 kV and 142 µA, (2) a relatively high magnification (125x, pixel size: 2.26 µm) was applied to detect the structures of interest, (3) a relatively low exposure time (1.9 sec) was taken, (4) samples were rotated 180° with a rotation step of 0.45°, and

(5) a 1mm aluminium filter was omitted. An optical 1 $mm^3$ selection was taken in the middle of the scaffold. After acquisition of the images at all rotation steps, the raw data were reconstructed to provide axial picture cross sections. After cone-beam reconstruction, the raw data were converted to a 16-bit bitmapped picture files with a resolution of 512x512 pixels. Using SkyScan's CT-analyzer v1.6 analyzing program, the pore size in the porous scaffolds and the distances between the lamellae in the unidirectional collagen samples were determined. Ten pores and the distance between 10 lamellae were measured automatically from a two-dimensional (2D) image at the largest diameter of the pore in the X and Y directions. 3D-Doctor V4.0 (Able Software, Lexington, MA) was used to create a final 3D model of the collagen sample. Model editing (e.g., rotating, editing, and transparency) was applied to optimize visualization of the collagen structures. Standardized software settings for scanning, cone-beam reconstruction, and gray-level thresholding were used in the projected and reconstructed files.

## Scanning electron microscopy

Collagen scaffolds were mounted on stubs and sputtered with an ultrathin layer of gold in a Polaron E5100 Coating System (Quorum Technologies). Collagen scaffolds were studied with a Jeol (Tokyo, Japan) JSM-6310 SEM at an accelerating voltage of 15 kV.

## Light microscopy

Scaffolds were fixed in 2.5% glutaraldehyde and 1% osmium tetroxide in 0.1 M phosphate buffer (pH 7.4) and embedded in epon. Sections of ~1 mm thickness were cut with an ultramicrotome, mounted on glass slides, and stained with 2% (w/v) toluidine blue in 5% (w/v) aqueous sodium tetraborate·$10H_2O$ for 20 s. Sections were examined and photographed with a Leica (Wetzlar, Germany) DM 6000B light microscope.

## RESULTS

Two structurally different types of scaffolds were analyzed: scaffolds with large (~100 μm) round pores and scaffolds with unidirectional lamellae. The samples were rotated 180° with a scanning period of 0.45°/1.9s without the use of an additional filter. The average scanning time per sample was 1h.

Table 1. Summary of Different Contrast Procedures and Their Effect on Micro-CT Contrast Enhancement of Collagenous Scaffolds

| Contrast agent(s) | Percentage applied | Impregnation time | Contrast |
|---|---|---|---|
| Osmium tetroxide | 1% | 1 day | Weak |
| Osmium tetroxide | 1% | 6 days | Moderate |
| Lead citrate | 1% | 1 day | Weak |
| Uranyl acetate | 2% | 1 day | Moderate |
| Uranyl acetate + lead citrate | 2% + 1% | 1 day + 1 day | Good |
| Osmium tetroxide + lead citrate | 1% + 1% | 6 days + 1 day | Moderate |
| Osmium tetroxide + uranyl acetate | 1% + 2% | 6 days + 1 day | Good |
| Osmium tetroxide + thiocarbohydrazide + osmium tetroxide | 1% + 1% + 1% | 6 days + 1h + 1h | Moderate |

Scaffolds with random round pores were visualized with different contrast enhancement techniques. Table 1 gives an overview of the protocols used and the contrast obtained as determined by visual inspection. Without any contrasting method, collagen scaffolds could not be visualized (data not shown). Moderate contrast enhancement in combination with a homogeneous distribution was achieved by the use of 2% uranyl acetate for 1 day, whereas the use of 1% osmium tetroxide for 1 day resulted in a lower signal, thus lower contrast (Fig. 1B, E). However, when scaffolds were impregnated with osmium tetroxide for 6 days, moderate contrast was achieved. In addition, thiocarbohydrazide was used to produce more contrast, but still only moderate contrast was obtained. The use of lead citrate gave poor results. A combination of contrast agents proved to be effective. The

most suitable contrast techniques for visualization of collagen scaffolds were a combination of 1% osmium tetroxide for 6 days and 2% uranyl acetate for 1 day (Fig. 1A, D) or a combination of 2% uranyl acetate for 1 day and 1% lead citrate for 1 day. These good contrast methods lead to most detail in the 3D reconstructions, whereas a weak contrasting protocol resulted in a poor 3D reconstruction (Fig. 1C, F). Two movies (see Supplemental Movies roundpores.avi and unidirectional-lamellae.avi, available online at www.liebert-online.com) show the 3D reconstruction of the collagen scaffolds with round pores and of the unidirectional lamellae from different angles rotated around the x-axis and y-axis. Figure 2 is a compilation of snapshot images from these movies.

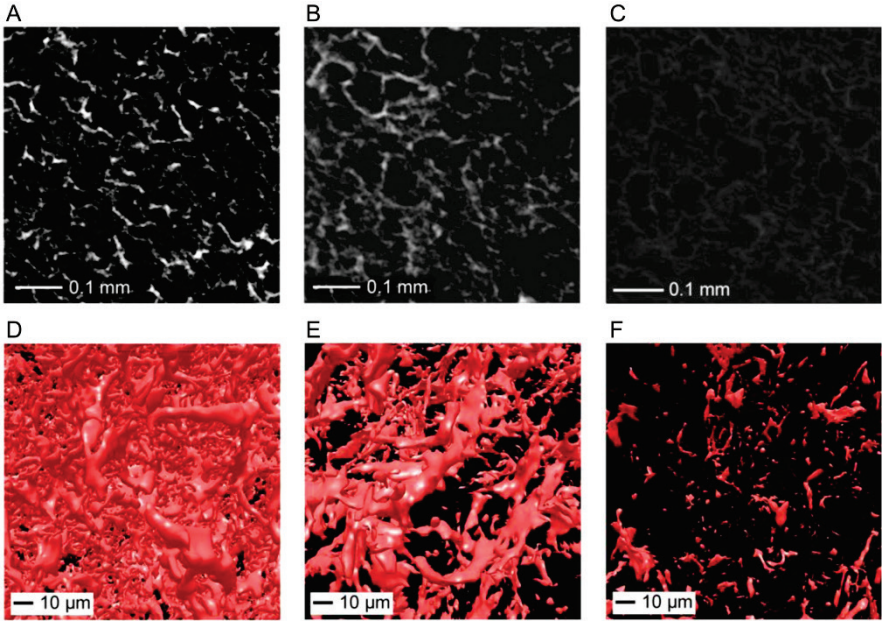


**Figure 1.** Effect of three contrast procedures on the attenuation of X-rays by porous collagenous scaffolds in a micro-CT setting. (A–C) represent 2D images, whereas (D–F) represent 3D images. (A, D) 1% osmium tetroxide for 6 days followed by 2% uranyl acetate for 1 day; (B, E) 1% osmium tetroxide for 6 days; (C, F) 1% osmium tetroxide for 1 day. Note good contrast in (A, D), moderate contrast in (B, ), and poor contrast in (C, F).

Figure 2A–D indicates random porosity of the porous scaffold, whereas Figure 2E–H points out the unidirectionality of the unidirectional scaffold.

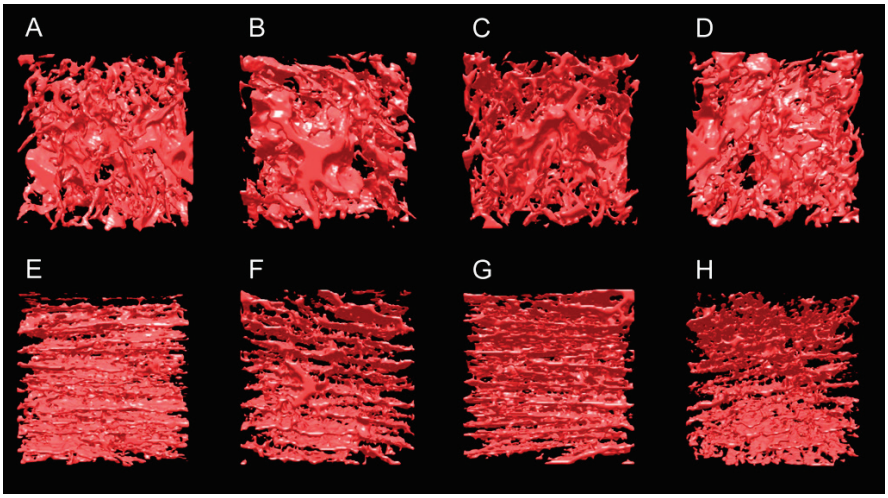


**Figure 2.** Snapshot still images taken from (A–D) a porous scaffold rotated around its y-axis and (E–H) a unidirectional scaffold rotated around its x-axis.

Using contrasting protocol 6, initial measurements were made, and the pore diameter could be determined. A representative part of the whole samples of collagen scaffolds with round pores and unidirectional lamellae was reconstructed using a stack of 2D images (see Fig. 3B for a scaffold with round pores and Fig. 3E for a unidirectional scaffold). Micro-CT images of collagen scaffolds with round pores revealed pore sizes of ~100 µm (Fig. 3A), whereas the distance between the lamellae in unidirectional scaffolds was around 50 µm (Fig. 3D). With the use of the whole file series of all gray-values from the scaffold material compared to the radio opaque air, the porosity of the scaffold was estimated to be 86 ± 5% (n=5 ± SD). Finally, the data obtained by micro-CT were compared to data acquired by scanning electron microscopy and by light microscopy.

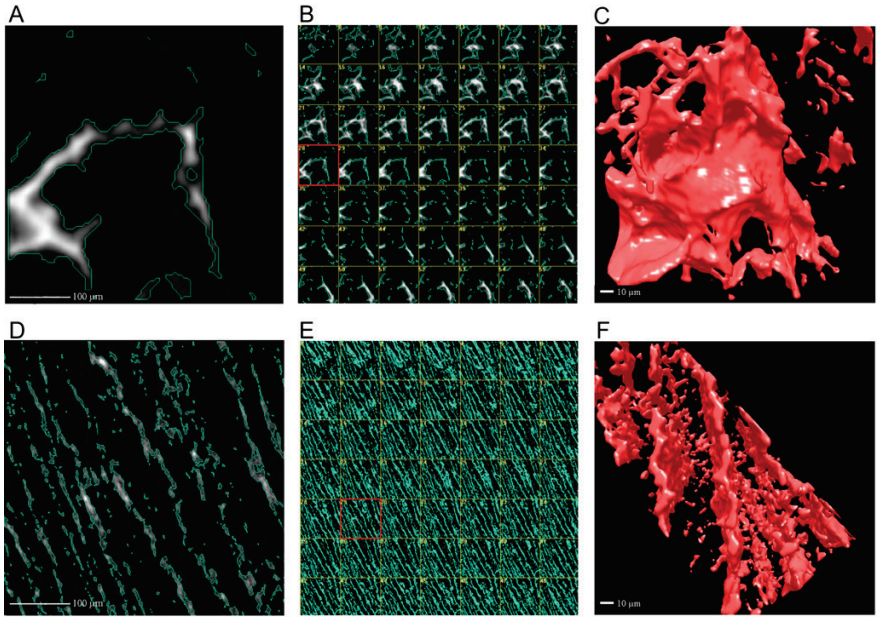


**Figure 3.** Micro-CT analysis of two different contrast-enhanced collagenous scaffolds. (A–C) Scaffold with round pores; (D, E) scaffold with unidirectional lamellae (D–F). (A, D) Single 2D projection image of a representative part of the scaffold; (B, E) complete stack of 2D images, covering 225 µm; (C, F) final 3D reconstruction showing porous and lamellar structures, respectively. Round pore diameters are ~100 µm, whereas distances between the lamellae are ~50 µm. Contrast method: 1% osmium tetroxide for 6 days and 2% uranyl acetate for 1 day. Scale bars are 100 µm in (A, D) and 10 µm in (C, F).

The pore diameter in scaffolds with round pores was generally about 100 µm for both methodologies, similar to micro-CT data (Fig. 4A–C). Scaffolds with unidirectional lamellae examined with scanning electron microscopy showed a distance between the lamellae of 51 ± 11 µm (n = 50 ± SD), similar to micro-CT. Using light microscopy, this distance was 64 ± 9 µm (n = 50 ± SD) (Fig. 4D–F). However, the micro-CT image of the unidirectional scaffold did not reflect the complete structure of the scaffold; the small struts in between the lamellae (generally 1–2 µm) were too thin to be visualized, because they are below the resolution limit of the equipment, which is about 6 µm using the applied settings.

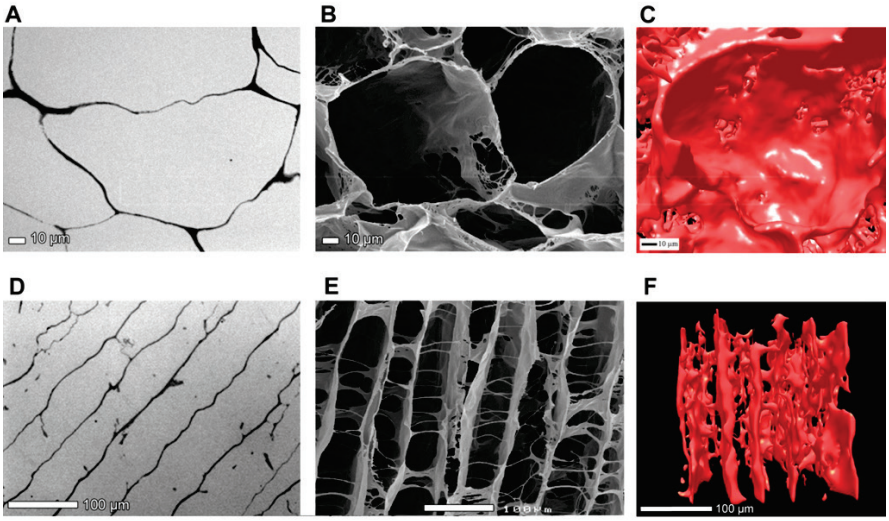


**Figure 4.** Comparison of images obtained using micro-CT with those obtained by light and electron microscopy pictures of random (A–C) and unidirectional (D–F) collagen scaffold obtained with light microscopy (A, D), scanning electron microscopy (B, E), and micro-CT imaging (C, F). Note comparable morphology between different analysis techniques. Also note that the fine struts in between collagen lamellae are not visible in the micro-CT image. Scale bars are 10 µm in (A–C) and 100 µm in (D–F).

## DISCUSSION

The 3D architecture of the scaffold is of great importance for the behaviour of cells. Cells behave differently in a 3D environment compared to a 2D structure.[16–19] Therefore, effective scaffold assessment techniques are required to evaluate the structural characteristics of scaffolds. Among these techniques SEM analysis is most popular for soft tissue, whereas micro-CT is generally used for hard tissue (such as bone).[3–5,10]

We here show imaging of collagen scaffolds by means of micro-CT. Using metal-based contrast enhancement methods, the structure of

collagen scaffolds was visualized. In this study, we only looked at porosity, but with the appropriate software, it is possible to determine other parameters, like density and interconnectivity, for soft scaffolds. When the structures in the collagen scaffolds are not too small, the 3D data sets obtained using micro-CT provide information about the sample's structure that is comparable to complementary methods such as light and electron microscopy, but with the obvious advantage of 3D of the whole specimen.[20–23] We were unable to visualize collagen scaffolds without contrast agents. Buttafoco et al.[24] did succeed in micro-CT visualization of collagen–elastin tubes without contrast agents. This difference with our scaffolds cannot be explained because the presence of thick elastin fibers does not provide more image contrast.

When structures are too small, one encounters the instrumental limitations of the micro-CT equipment. The estimated porosity may thus be overvalued because of this. Nano-CT may be a solution to this problem. The theoretical instrumental limitation of the nano-CT apparatus is 200 nm compared to 2 μm for the micro-CT apparatus.[25] Drawbacks of micro-CT are the difficulty of thresholding, beam hardening, and the need for specialized software to quantify certain parameters (e.g., interconnectivity).[6] Before 3D modeling, the crucial step is to separate scaffold material from background (performed by thresholding the image gray-level[9]), which affects the subsequent visualization. When too much thresholding is applied, scaffold material is undervalued. Beam hardening is known as the high exposure of the scaffold center as a result of scaffold attenuation of the lower energy rays of the used polychromatic X-ray beam. As a consequence, thresholding is no longer dependent solely on radio-density, but also on specimen size.[26,27]

Although micro-CT still faces some problems when used for scaffolds made from soft natural biomaterials (i.e., limitation to visualize small structures), this method is able to provide a 3D reconstruction of the specimen in little time and with little processing, whereas techniques like scanning electron microscopy and light microscopy are very laborious. In addition, it is possible to scan a large specimen with good morphology of the whole scaffold. It should be seen as complementary to other methods.

## CONCLUSION

Using specific contrasting protocols, we showed the potential of imaging soft, proteinaceous materials by micro-CT. The most suitable contrast techniques for visualization of collagen scaffolds were a combination of 1% osmium tetroxide for 6 days + 2% uranyl acetate for 1 day, and a combination of 2% uranyl acetate for 1 day + 1% lead citrate for 1 day. A drawback is that small details (less than few μm, e.g., struts in unidirectional scaffolds) cannot be observed with micro-CT. For better resolution, nano-CT is needed.

## REFERENCES


1. Guldberg, R.B., Tissue engineering: micro-CT imaging. Sci Med. 2003;9:9.
2. Feldkamp, L.A., Goldstein, S.A., Parfitt, A.M., Jesion, G., Kleerekoper, M., The direct examination of threedimensional bone architecture *in vitro* by computed tomography. J Bone Miner Res. 1989;4:311.
3. Muller, R., Hildebrand, T., Ruegsegger, P., Non-invasive bone biopsy: a new method to analyse and display the threedimensional structure of trabecular bone. Phys Med Biol. 1994;39:145.
4. Ruegsegger, P., Koller, B., Muller, R., A microtomographic system for the nondestructive evaluation of bone architecture. Calcif Tissue Int. 1996;58:24.
5. Goulet, R.W., Goldstein, S.A., Ciarelli, J.L, Brown, M.B., Feldkamp, L.A., The relationship between the structural and orthogonal compressive properties of trabecular bone. J Biomech. 1994;27:375.
6. Ho, S.T., Hutmacher, D.W., A comparison of micro-CT with other techniques used in the characterization of scaffolds. Biomaterials. 2006;27:1362.
7. Lin, A.S.P., Barrows, T.H., Cartmell, S.H., Guldberg, R.E., Microarchitectural and mechanical characterization of oriented porous polymer scaffolds. Biomaterials. 2003;24:481.
8. Lin-Gibson, S., Copper, J.A., Landis, F.A., Cicerone, M.T., Systematic investigation of porogen size and content on scaffold morphometric parameters and properties. Biomacromolecules. 2007;8:1511.
9. Peyrin, F., Mastrogiacomo, M., Cancedda, R., SEM and 3D synchrotron radiation. Micro-tomography in the study of bioceramic scaffolds for tissue-engineering applications. Biotechnol Bioeng. 2007;9:638.
10. Wang, F., Shor, L., Darling, A., Khalil, S., Sun, W., Guceri, S., Lau, A., Precision extruding deposition and characterization of cellular poly-e-lactone tissue scaffolds. Rapid Prototyping J. 2004;10:42.
11. Faraj, K.A., van Kuppevelt, T.H., Daamen, W.F., Construction of collagen scaffolds that mimic the threedimensional architecture of specific tissues. Tissue Eng. 2007;13:2387.
12. Schoof, H., Apel, J., Heschel, I., Rau, G., Control of pore structure and size in freeze-dried collagen sponges. J Biomed Mater Res. 2001;58:352.
13. Ann Ellis, A., Poststaining grids for transmission electron microscopy conventional and alternative protocols. Methods Mol Biol. 2007;369:97.
14. Kelly, R.O., Dekker, R.A., Bleumink, K., Ligand-mediated osmium binding: its application in coating biological specimens for scanning electron microscopy. J Utrastruct Res. 1973;45:254.
15. Seligman, A.M., Wasserkrug, H.L., Hanker, J.S., A new staining method (OTO) for enhancing contrast in lipidcontaining membranes and droplets

in osmium tetraoxide- fixed tissue with osmiophilic thiocarbohydrazide (TCH). J Cell Biol. 1996;30:424.
16. Inanc, B., Elcin, A.E., Elcin, Y.M., Osteogenic induction of human periodontal ligament fibroblasts under two- and three-dimensional culture conditions. Tissue Eng. 2006;12:257.
17. Sun, T., Jackson, S., Haycock, J.W., MacNeil, S., Culture of skin in 3-D rather than 2D improves their ability to survive exposure to cytotoxic agents. J Biotechnol. 2006;122:372.
18. Stegemann, J.P., Nerem, R.M., Altered response of vascular smooth muscle cells to exogenous biochemical stimulation in two- and three-dimensional culture. Exp Cell Res. 2003;283:146.
19. Cukierman, E., Pankov, R., Stevens, D.R., Yamada, K.M., Taking cell-matrix adhesions to the third dimension. Science, 2001;294:1708.
20. Ritman, E.L., Micro-computed tomography-current status and developments. Annu Rev Biomed Eng. 2004;6:185.
21. Oosterwyck van, H., Sloten van der, J., Perre van der, G., Jansen, J., Wevers, M., Naert, I., Use of microfocus computerized tomography as a new technique for characterizing bone tissue around oral implants. J Oral Implantol. 2000;26:5.
22. Gauthier, O., Muller, R., Von Stechow, D., Lamy, B., Weiss, P., Bouler, J.M., Aguado, E., Daculsi, G., *In vivo* bone regeneration with injectable calcium phosphate biomaterial: a three-dimensional micro-computed tomographic, biomechanical and SEM study. Biomaterials. 2005;26:5444.
23. Cartmell, S., Huynh, K., Nagaraja, S., Guldberg, R., Quantitative microcomputed tomography analysis of mineralization within three-dimensional scaffolds *in vitro*. J Biomed Mater Res A. 2004;69:97.
24. Buttafoco, L., Engbers-Buijtenhuijs, P., Poot., A.A., Dijkstra, P.J., Vermes, I., Feijen, J., Physical characterization of vascular grafts cultured in a bioreactor. Biomaterials. 2006;11:2380.
25. Cnudde, V., Masschaele, B., Dierick, M., Vlassenbroeck, J., Hoorebeke van, L., Jacobs, P., Recent progress in X-ray CT as a geosciences tool. Appl Geochem. 2006;21:826.
26. Duvall, C.L., Taylor, W.R., Weiss, D., Guldberg, R.E., Quantitative microcomputed tomography analysis of collateral vessel development after ischemic injury. Am J Physiol Heart Circ Physiol. 2004;287:H302.
27. Bonse, U., Busch, F., X-ray computed microtomography (microCT) using synchrotron (SR). Prog Biophys Mol Biol 65, 133, 1996.

# CHAPTER 7

# Osteogenesis around CaP-coated titanium implants visualized using 3D histology and micro-computed tomography

Vincent M.J.I. Cuijpers, Hamdan S. Alghamdi, Natasja W.M. van Dijk, Jakub Jaroszewicz, X. Frank Walboomers, John A. Jansen.

J Biomed Mater Res Part A 2015. Nov;103(11):3463-73.

## INTRODUCTION

The success of bone-anchored implants is characterized by the presence of direct contact between the surrounding bone and implant surface.[1,2] Previous studies[3,4] suggested that bone formation is dependent on implant characteristics such as the used bulk implant material, implant surface texture, and eventually implant surface composition.[5,6] Several studies have already shown that surface modifications, such as calcium phosphate (CaP) coatings, can enhance bone-implant healing,[7-9] as they improve bioactivity and osteoconductivity.

Light microscopy is still the gold standard to study the implant-bone healing phase at submicron (i.e. cellular) resolution.[10] However, histological sections can create only a two-dimensional (2D) representation of a three-dimensional (3D) object. In contrast, bone remodeling is a dynamic process of simultaneous bone absorption and new bone deposition, which continuously occurs in all directions. Consequently, it is important to study this tissue reorganization phenomena in 3D. This becomes even more important when the dynamic equilibrium of balance is disturbed, as is the case in osteoporosis, a compromised bone condition affects the finally achieved implant fixation.[11] Several high-resolution 3D analysis techniques are available to study bone. For example, micro-computed tomography (micro-CT) is able to visualize the complete 3D bone architecture and to analyze bone structural parameters in 3D.[12,13] However, micro-CT has a resolution that is limited to the supracellular sizes of >5-10 μm.[14] Also, micro-CT does not allow the use of specific labels, which allow the detection of specific bone cells or dynamic processes. Therefore, it would be more optimal if a method is employed combining the higher resolution of conventional light microscopy, with the 3D imaging capacity from micro-CT imaging. In the current study, we aimed to assess 3D histology and postulated that such a technique can be used to fill in the shortcomings of micro-CT visualization.

In view of the above mentioned, the objective of the current study was to determine whether 3D histology is a potential tool to gain

additional insight into 3D bone architecture at high-resolution, including bone dynamics at the peri-implant area.

## MATERIALS AND METHODS

### Animal model

The number of experimental animals was determined by statistical power calculation based on earlier results.[15] Experimental animals were eight 12-week-old female Wistar rats with a mean weight of 250 g. All *in vivo* work was conducted in agreement with ISO standards and protocols of the Radboud University Medical Center, Nijmegen, The Netherlands. National guidelines for care and use of laboratory animals were obeyed and approval of the Experimental Animal Ethical Committee was obtained. (Approval No. RU-DEC 2011–203). Ovariectomies (OVX) were performed in four rats to establish an osteoporotic condition. The remaining four rats were indicated as control rats and received only sham surgery instead of an ovariectomy.

### Implants

Cylindrical-shaped titanium (Ti) implants (Ø 2mm and length 5 mm) were manufactured from commercially pure titanium, grit-blasted (roughness, $R_a$=0.5 μm) and ultrasonically cleaned in nitric acid 10% (15 min), acetone (15 min), and ethanol 70% (15 min) successively and thereafter air-dried. The implants were divided into two groups, i.e., with and without a calcium-phosphate (CaP) coating.

The non-coated implants were autoclaved and stored at room temperature without any further treatment before implantation. The coating procedure was performed using a radiofrequency (RF) magnetron sputter unit (Edwards ESM 100, Crawford, UK). Hydroxyapatite ($Ca_5(PO_4)_5OH$) granules (diameter 0.5-1.0 mm; CAM Bioceramics BV, Leiden, The Netherlands) were used as target material in the deposition process. Prior to sputtering, the implants

were cleaned by etching for 10 min with argon ions. The sputtering process pressure was 5 x $10^{-3}$ mbar and the sputter power 400 W, which resulted in a 0.5 µm thick CaP coating. After deposition, all coated specimens were subjected to an additional heat treatment using an infra-red oven (Quad Ellipse Chamber, Model E4-10-P, Research Inc., MN) for 30 sec at 650°C. This method and the resulting ceramic coating were described and analyzed previously in detail in a previous paper.[16] Before implantation, the coatings were characterized by thin film X-ray diffraction (Philips, PW3710, Almelo, The Netherlands). Then, implants were autoclaved and stored at room temperature.

## Surgical procedure and implant installation

Surgery was performed under general inhalation anesthesia and sterile conditions. Pre-operatively, Rimadyl® (5.0 mg/kg) and Temgesic® (0.02 mg/kg) were administered to reduce postoperative pain. In brief, after exposing the knee joints, cylindrical holes (Ø 2 mm) were prepared using a dental bur (Elcomed 100, W&H Dentalwerk Burmoos, Austria) with low rotational drill speed (1200 rpm) and continuous external cooling with saline. Implants were placed bilaterally, parallel to the long-axis of the femurs. The implants with and without coating were applied, alternating in the right and left femoral condyle, equally divided over both the control and OVX rats, which resulted always in n=4 for each individual group. After insertion of the implants, the soft tissue layers were closed with absorbable sutures (Vicryl® 4·0, Ethicon Products, Amersfoort, the Netherlands) and the skin with skin staples (Agraves®, InstruVet C.V., Cuijk, the Netherlands).

## Fluorochrome administration

To visualize bone turnover dynamics, all rats received sequential fluorochrome labels of calcein blue (4-Methylumbelliferone-8-methyliminodiacetic acid), calcein Bis[N,N–bis(carboxymethyl) amino- methyl], synonym: fluorescein, fluorexon), alizarin complexone

(alizarin-3-methyliminodiacetic acid) and rolitetracycline (all Sigma, St. Louis, MO) at 1, 3, 5 and 7 weeks postoperatively (Table 1). For each label, a stock-solution was prepared in 10 mL isotonic sodium bicarbonate solvent (2% $NaHCO_3$) and filtered (0.22 sterile Millipore filter). Finally, 100 µl fluorochrome solutions were used for subcutaneous administration. At 8 weeks post-implantation, rats were euthanized with an overdose of Pentobarbital (Nembutal, Apharmo BV, Arnhem, the Netherlands), and the implants with surrounding tissue were retrieved. The specimens were fixed for 48h in 10% neutral buffered formalin solution with subsequent dehydration in an ascending series of ethanol. Thereafter, specimens were processed for micro-CT respectively histological sectioning.

**Table 1**. Scheme for subcutaneous fluorochrome administration at two weeks intervals including dose, and selected fluorescence filters, including excitation and emission spectra filter specifications.

| Fluorochrome | Calcein Blue | Calcein | Alizarin-Complexone | Rolitetracycline |
|---|---|---|---|---|
| Color | Blue | Green | Red | Yellow |
| Dose (mg/kg body weight) | 30 | 10 | 30 | 25 |
| Weeks before sacrifice | 7 | 5 | 3 | 1 |
| Filter set | 01 | 10 | 00 | 18 |
| Excitation (nm) | BP 365/12 | BP 450-490 | BP 530-585 | BP 390-420 |
| Dichroic beam-splitter (nm) | FT 395 | FT 510 | FT 600 | FT 425 |
| Emission (nm) | LP 397 | BP 515-565 | LP 615 | LP 450 |

## Bone healing analysis

The overall design of the analysis of the retrieved specimens is shown in Figure 1. Analysis consisted of *ex vivo* micro-computed tomography and 3D histology. Schematically, specimens were divided in two groups, either embedded in PMMA (Figure 1); or implants were removed (Figure 1B), analyzed with micro-CT (Figure 1C) and finally embedded for paraffin sectioning (Figure 1E,F). The paraffin samples (decalcified and dehydration as described[15]) were cut into 5 µ thick

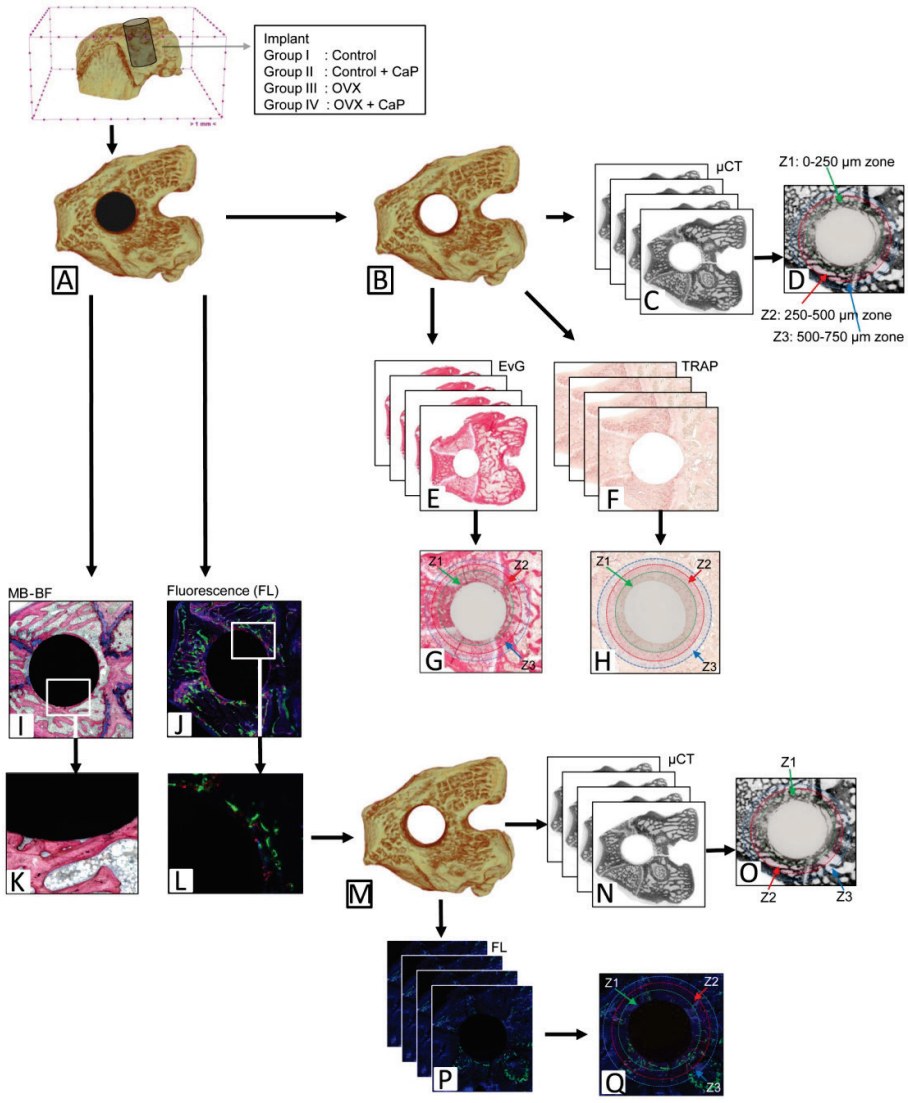


**FIGURE 1.** Schematic representation of the study design containing non-coated and CaP coated titanium (Ti) implants in the femoral condyle of control and osteoporotic (OVX) rats (group I-IV) before (A) and after (B) implant removal. Micro-computed tomography (µCT) bone volume analysis (C,D) in Ø 0-250, 250-500 and 500-750 µm zones from the implant surface (Z1-Z3). Serial paraffin sectioning and consecutive histology imaging of elastin van gieson (EVG) and tartrate resistant alkaline phosphate (TRAP) stained slices (E,F), including bone volume and osteoclast analysis in respectively EVG (G) and TRAP stained (H) slices in the three defined zones (Z1-

Z3). Histology slices containing the Ti implant, stained with methylene blue - basic fuchsin (MB-BF) and containing incorporated fluorochromes (FL) (calcein blue, calcein, alizarin complexone and rolitetracyclin) are depicted in (I) and (J), including detail (K) and (L). Implant removal (M) and consecutive µCT bone volume analysis (N,O) in the three defined zones Z1-Z3. Serial sectioning of samples containing fluorochromes (P) to analyze bone formation (Q) and resorption within the above mentioned zones (Z1-Z3).

serial transversal sections, starting from the just underneath the cortical bone, over a length of 2.5 mm. Each fifth serial slice was selected, i.e. resulting in approximately 100 sections for histological 3D reconstruction and analysis (Figure 1G,H). Elastin van Gieson (EVG) histochemical staining technique was used to visualize tissue, and tartrate-resistant acid phosphatase (TRAP) enzyme staining was applied to highlight osteoclast activity. For this purpose, slides were incubated at 37°C for respectively 1-2h in TRIS/$MgCl_2$-buffer and 2h in acid phosphate solution including pararosanilin, naphtol AS-BI phosphate, and potassium sodium tartrate.

For the PMMA embedded implants, three 15 µm thin transversal sections were made using a modified Leica SP1600 inner circular sawing microtome (Leica microsystems, Wetzlar, Germany).[17] These sections were also prepared starting from the level just beneath the cortical bone, at 300 µm distance from each other, and stained with methylene blue - basic fuchsin (MB-BF) to visualize overall bone tissue morphology (Figure 1I), or left unstained to assess fluorochrome expression at the bone-implant interface (Figure 1J). After these 3 sections were made, the remainder of the embedded implant was deplastified, the implant was removed, and the tissue sample was scanned using micro-CT (Figure 1M,N). Thereafter, the sample was re-embedded in PMMA, and 5 µm thick serial plastic sections were created over a length of 1mm (i.e., ~200 sections) using a RM2155 microtome with a TC 65 blade (both Leica Microsystems GmbH, Wetzlar, Germany). These serial sections were stretched on adhesive object slides (TruBond™ 380, Tru-Scientific LLC, Bellingham, WA) to allow analysis of the fluorescence signal in 3D (Figure 1P,Q).

For all serial sectioning methods, occasionally upon visual inspection, slices were found to be damaged or deformed. These sections were always replaced with an adjacent slice.

## *Ex-vivo* micro-computed tomography

All samples were scanned using a Skyscan 1172 micro-CT system (Bruker microCT, Kontich, Belgium) with the following scanning settings: X-ray source 80kV and 100µA, rotation step 0,3 degree, 180 deg rotation, 1 mm Al filter and image pixel size 8,1 µm. All projected files (Figure 1C) were reconstructed using the Nrecon V1.4 (Bruker) cone beam reconstruction program. CTAn V.1.11 and CT-Vox V2.1.1 software (Bruker) were used for segmentation, registration, quantification and 3D volume reconstruction of all micro-CT data. For BV percentage analysis, a standardized gray-value threshold was set for bone and the BV percentage was calculated in fixed volume of interest (VOI) zones of Ø 250, 500 and 750 µm surrounding the implant surface (Figure 1D) with a minimal depth of 1.5 mm.

## Histological analysis

Digital images were obtained of all histological sections using an automated Axio Imager Z1 microscope (Carl Zeiss Micro Imaging GmbH, Göttingen, Germany) at 100x magnification. In the acquired images, three zones of evaluation were created, at respectively 0-250, 250-500 and 500-750 µm from the implant surface.
Fluorochrome sequence, color, and dosage, sacrifice time and selected filter sets for fluorescence signal acquisition, including excitation, dichroic beam-splitter and emission filter specifications, are all listed in Table 1. To detect stain and fluorochrome expression, color recognition was based on the HSI (Hue, Saturation and Intensity) model values of the corresponding stain and fluorochrome (Table 2).[18] Therefore, threshold settings of color, saturation and brightness were defined and implemented.

For alignment of the EVG stained bone, TRAP stained osteoclasts, and bone incorporated fluorochrome microscopy image series, the StackReg plug-in for ImageJ (National Institutes of Health (NIH), Bethesda, MD) was used.[19]

For 3D analysis and visualization, separate stacks of binarized 2D images were created, which contained the boundaries of the bone, TRAP, and fluorochrome expression. After interpolating the 2D boundaries into 3D, the bone-, TRAP-, and fluorochrome volumes were calculated within the three defined VOI cylinders. Thereafter, the measured bone-, TRAP- and fluorochrome volumes were subtracted from the total VOI cylinders, resulting in volume percentages of bone, osteoclasts, and the fluorochromes calcein, alizarin complexone and rolitetracycline, within each defined volume. 3D-Doctor (Able Software Corp, Lexington, MA) was used to create and visualize 3D models of fluorochrome deposition and osteoclasts areas within the three VOIs, merging all solitary fluorochromes within one model.

**Table 2.** Hue, Saturation and Intensity (HSI) threshold settings for histochemical staining and fluorochrome selection.

| | Hue | Saturation | Intensity |
|---|---|---|---|
| Transmitted light microscopy: | | | |
| TRAP staining | 0-12 | 48-73 | 53-247 |
| EvG staining | 0-255 | 0-96 | 73-255 |
| Fluorescence microscopy: | | | |
| Calcein | 49-126 | 0-255 | 121-255 |
| Alizarin complexone | 204-255 | 0-255 | 86-255 |
| Rolitetracycline | 1-51 | 1-255 | 118-255 |
| Blue, total bone | 147-203 | 0-255 | 51-255 |

## Statistical Analysis

Statistical analysis was performed using GraphPad InStat, version 3.05 (GraphPad Software Inc., San Diego, CA). Un-paired *t*-test statistical analysis was applied on BV% data derived from both micro-CT and histological analysis. ANOVA analysis with *post-hoc* Tukey Kramer testing was used to evaluate BV% between all four groups within one of the defined zones from the implant surface; and for data derived from each individual fluorochrome and TRAP expression.

## RESULTS

General observations showed that all animals remained in good health during the experimental period and did not show any postoperative wound healing complications. At sacrifice, no signs of severe inflammation or other undesirable tissue reactions were seen around the titanium implants.

### Micro-CT analysis

Visual inspection of single transversal cross-section 2D micro-CT images showed that more trabecular bone was present around the control samples compared to the OVX group. Bone volume (BV) percentage results within the three distinct zones (0-250, 250-500 and 500-750 μm) from the implant surface of samples of the four groups are depicted in Figure 2A. Statistical analysis showed a significant ($p$<0.05) decrease in BV between the pooled data of all control vs. the OVX rats, which on average was 22.4%. No significant differences existed between the non-coated and CaP-coated implants in the control or OVX groups. On the other hand, a significant difference ($p$<0.05) in BV was found between the Ø 0-250 and 500-750 μm region around the non-coated implants in the OVX rats. There were no other significant differences between the defined zones in any of the groups.

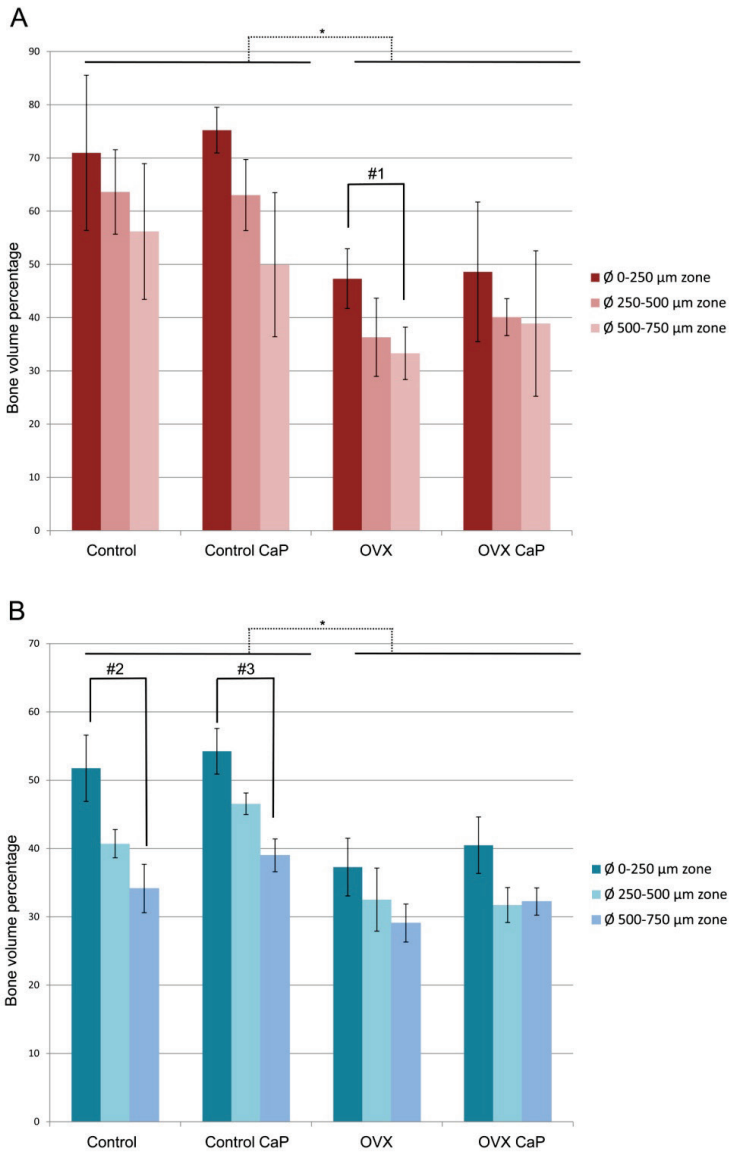


**FIGURE 2.** Micro-computed tomography (A) and histology (B) bone volume percentage analysis (BV%) of control and osteoporosis induced (OVX) rats with CaP and non-coated Ti implants in Ø 0-250, 250-500 and 500-750 µm zones from the implant surface. Significant difference between the pooled groups ($p$<0.05) and between zones are respectively depicted as * and #.

## Descriptive microscopical evaluation

In Figure 3 the microscopic images of histological stained slices of the femoral condyle samples of control (A-D) and osteoporotic (OVX) (E-L) rats with and without CaP-coated titanium (Ti) implants are presented. Light microscopical analysis of the EVG stained sections showed the formation of new bone around the implant surface (Figure 3A,D,G,J).
The methylene blue - basic fuchsin stained sections revealed that the newly formed bone was in direct contact with the Ti surface. Besides the clear presence of an osteoporotic condition in the osteoporotic animals, showing less bone compared to the control animals (see Figure 3H,K), no gross differences in bone response were observed between the various implant groups and conditions.

Fluorescence microscopy demonstrated the clear presence of calcein and alizarine complexone fluorescent signals in the samples with (Figure 3C,F,I,L) as well as without implant. Rolitetracycline was less bright and only detectable at higher magnification, whereas calcein blue was never seen.
Analysis at high magnification (400x) indicated that both control samples demonstrated calcein and alizarin complexone. In control animals with CaP coated implants, high levels of calcein, alizarin complexone and roliteracycline were found, as depicted in Figure 4A-D. Upon visual examination, the fluorescent signals detectable in the OVX animals were lesser evident. Also, calcein was seen mostly distant from the implant surface. However, the CaP coated implant in the OVX animal presented calcein and alizarin complexone in a comparable fashion to the control situation.

TRAP-staining showed the prominent presence of positively stained osteoclasts in remodeling lacuna in the bone surrounding the implants. In control animals, many osteoclasts were seen in vicinity of the non-coated implants, as shown in Figure 4E,F. However, most osteoclasts were present at a distance from the implant surface. Around the CaP coated implants, less osteoclasts were found, but they were more evenly distributed comparing the area close to the implant with more distant areas. In the OVX rats, almost no TRAP staining was

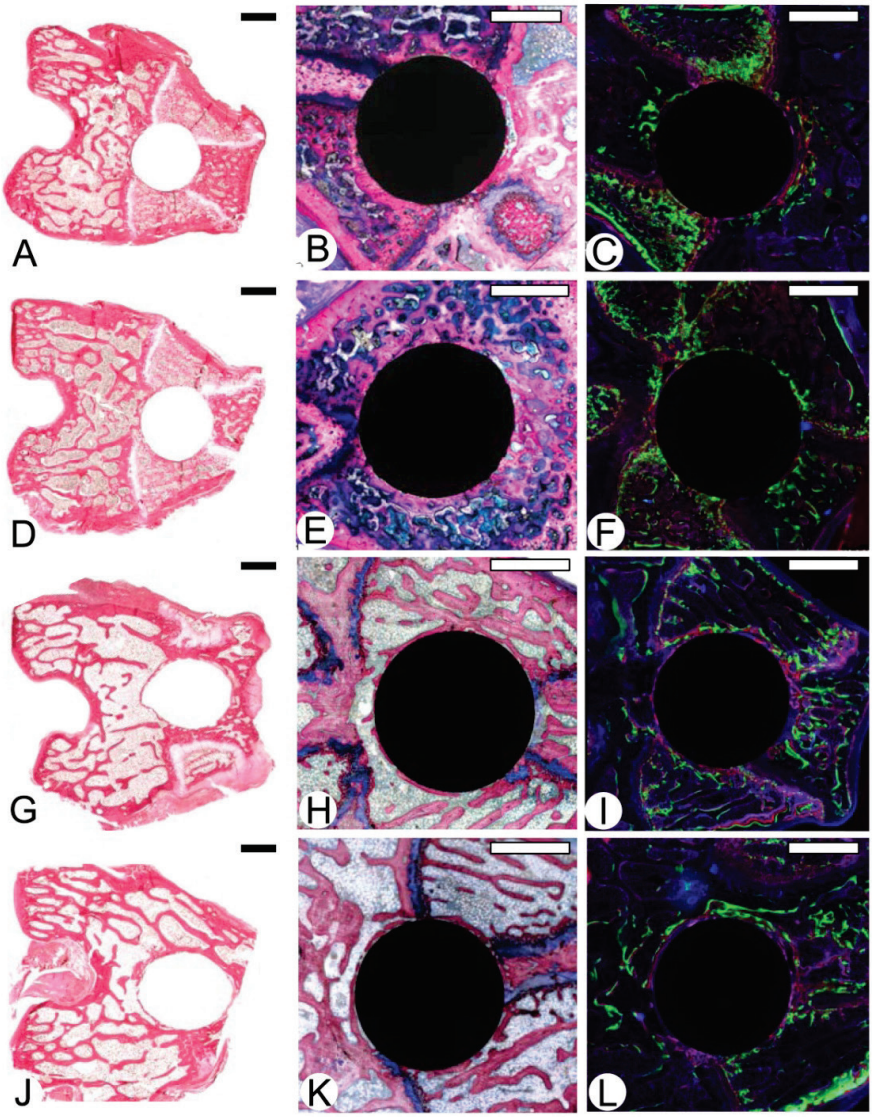


**FIGURE 3.** Histological images of the femoral condyle samples of control (A-D) and osteoporotic (OVX) (E-L) rats with and without CaP-coated titanium (Ti) implants. Elastin van Gieson staining (A,D,G,J) showing bone in red, methylene blue - basic fuchsin (B,E,H,K) whereby bone is pink-red, and fluorescence expression (C,F,I,L) of calcein, and alizarin complexone in respectively green and red. Bar size = 1mm.

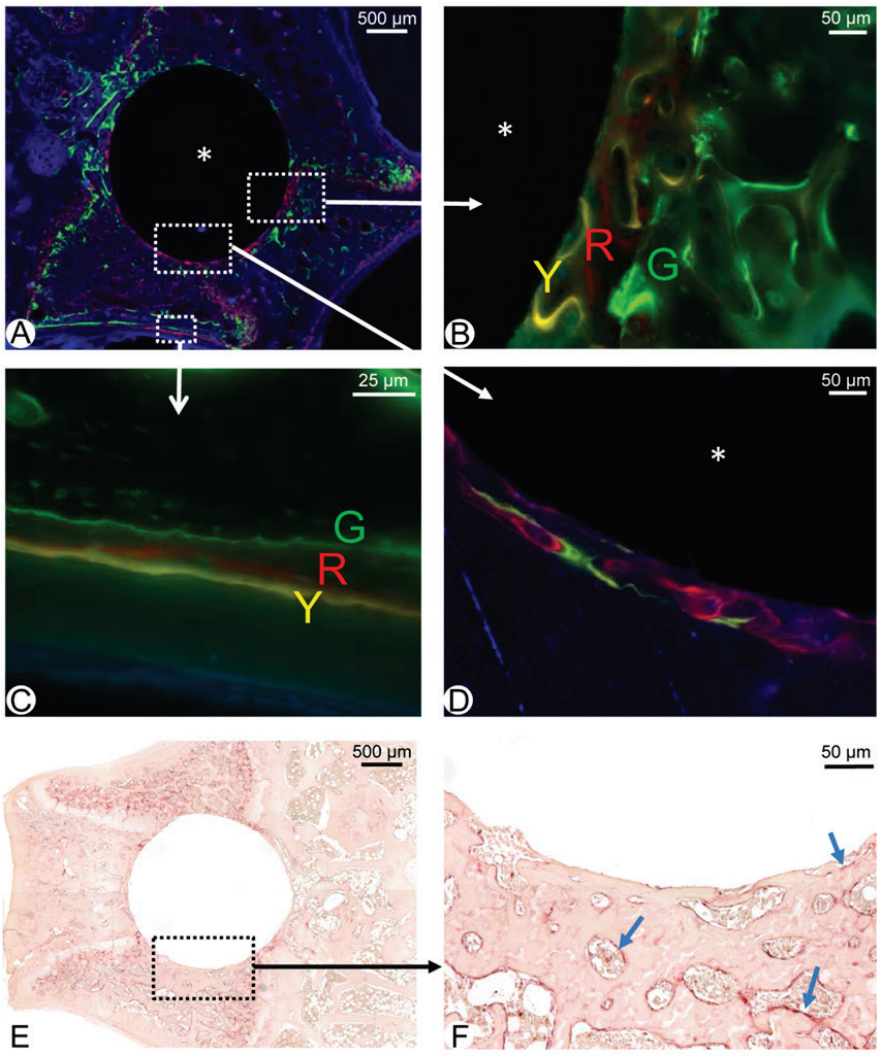


**FIGURE 4.** Fluorescent micrographs of the femoral condyle of control rats with a CaP-coated Ti implant. Detailed visualization (B-D) of deposition of calcein (green, G), alizarin complexone (red, R) and rolitetracycline (yellow, Y) at the bone-implant interface (B,D) and in cortical bone (C). Tartrate resistant alkaline phosphate (TRAP) stained light micrographs (E,F) of control rats without CaP coating showing osteoclast expression.

visible around the non-coated implants. However, in case of CaP-coated implants, again more osteoclasts were found, and similarly to the control animals, these cells were seen evenly distributed throughout the surrounding bone tissue.

### 3D histology bone volume analysis

Using the EVG stained sections, the histological bone volume (BV) percentages in the three pre-defined zones were calculated and are presented in Figure 2B. Statistical analysis showed a significant ($p$<0.05) decrease of 10,5% on average for BV, when assessed between the pooled data of all control vs. the OVX rats. No significant differences existed between the non-coated and CaP-coated implants in the control or OVX groups. On the other hand, significant differences ($p$<0.05) in BV were found between the Ø 0-250 and 500-750 µm regions in the control rats, both around the non-coated as well as around the CaP-coated implants. There were no other significant differences between the defined zones in the OVX groups.

### 3D histology fluorochrome analysis

The quantified fluorochrome measurement data are presented in Figure 5, as the volume percentage of calcein, alizarin complexone and rolitetracycline in Ø 0-250, 250-500 and 500-750 µm zones from non-coated and CaP-coated titanium implant surfaces in the femoral condyle of rats were demonstrated. Although individual comparisons between the different zones or different fluorochromes are not significant due to the too low power, results indicate that the pooled data of control animals showed significantly ($p$<0.05) higher total volumes of fluorescence within all defined zones, compared to the corresponding osteoporotic animals. This same statistical difference also applied, when the non-coated as well as the coated implants were regarded separately. Further, the non-coated implants showed significantly ($p$<0.05) lesser fluorochrome expression volume compared to the coated implants. This difference was found for the control, as well as for the osteoporotic animals.

A final comparison was made dealing with the temporal dynamics of the bone turnover. In the control rats, the signal for alizarin (injected 5 weeks before sacrifice) for all groups was significantly ($p$<0.05) greater than that of calcein (injected 7 weeks before sacrifice). In the osteoporotic rats, the opposite applied, i.e., the signal for calcein was significantly higher than alizarin.

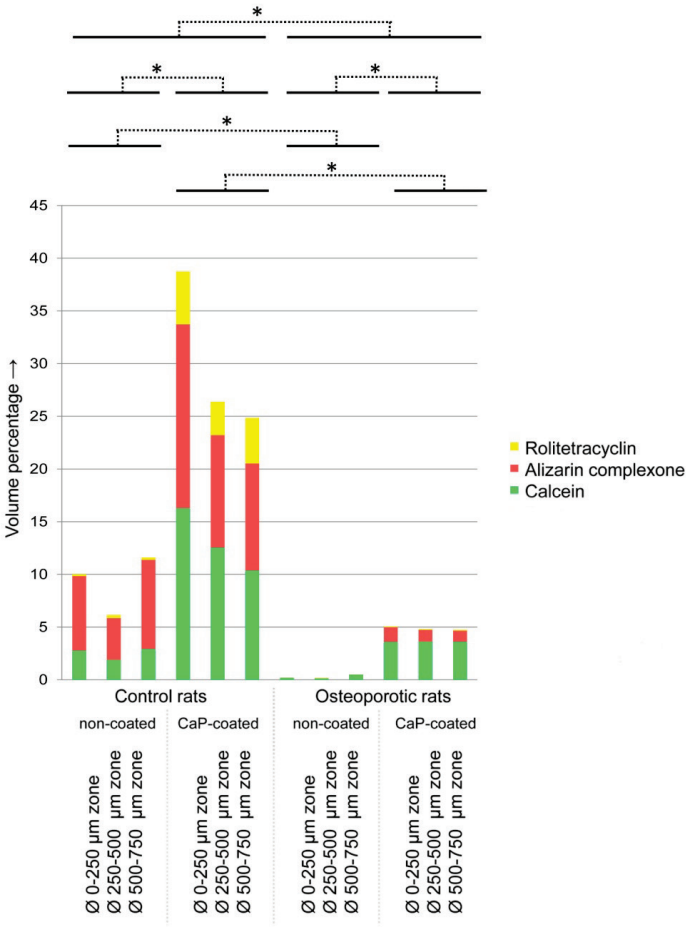


**FIGURE 5.** Volume percentage of calcein, alizarin complexone, and rolitetracycline in Ø 0-250, 250-500 and 500-750 µm zones (1mm height) from non-coated and CaP-coated titanium implant surfaces in the femoral condyle of rats. Significant difference ($p$<0.05) between pooled groups depicted as *.

## 3D histology TRAP analysis

Figure 6 depicts the quantification of the TRAP-positive volume percentage measured within the Ø 0-250, 250-500 and 500-750 µm zones from the non-coated and CaP coated Ti implant surface in the femoral condyle of all rats. In general, the measurements corroborated the visual inspection mentioned above.

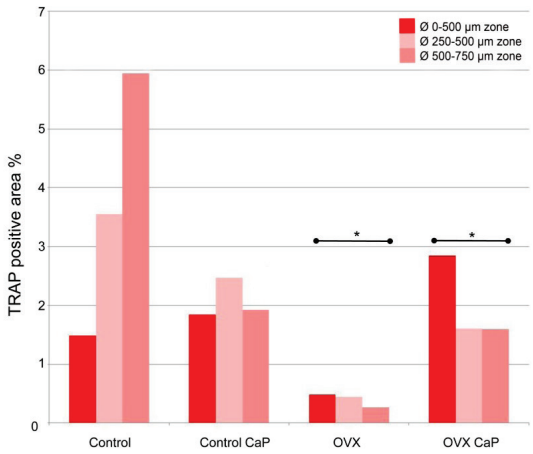


**FIGURE 6.** TRAP positive area percentage within the Ø 0-250, 250-500 and 500-750 µm zones from the non-coated and CaP-coated Ti implant surface in the femoral condyle of control and osteoporotic (OVX) rats. Significant difference ($p$<0.05) in BV% depicted as *.

Even though individual comparisons between the different zones are not significant due to the too low power, pooled data of the control animals showed significantly ($p$<0.05) more TRAP positive volume compared to the OVX animals. Also, significantly more osteoclast positive areas were found for the control animal with a non-coated implant, compared to the osteoporotic rat. For the OVX animals the coating resulted in a TRAP expression level, comparable to the control animals with coated implants. There were no other significant differences between the groups.

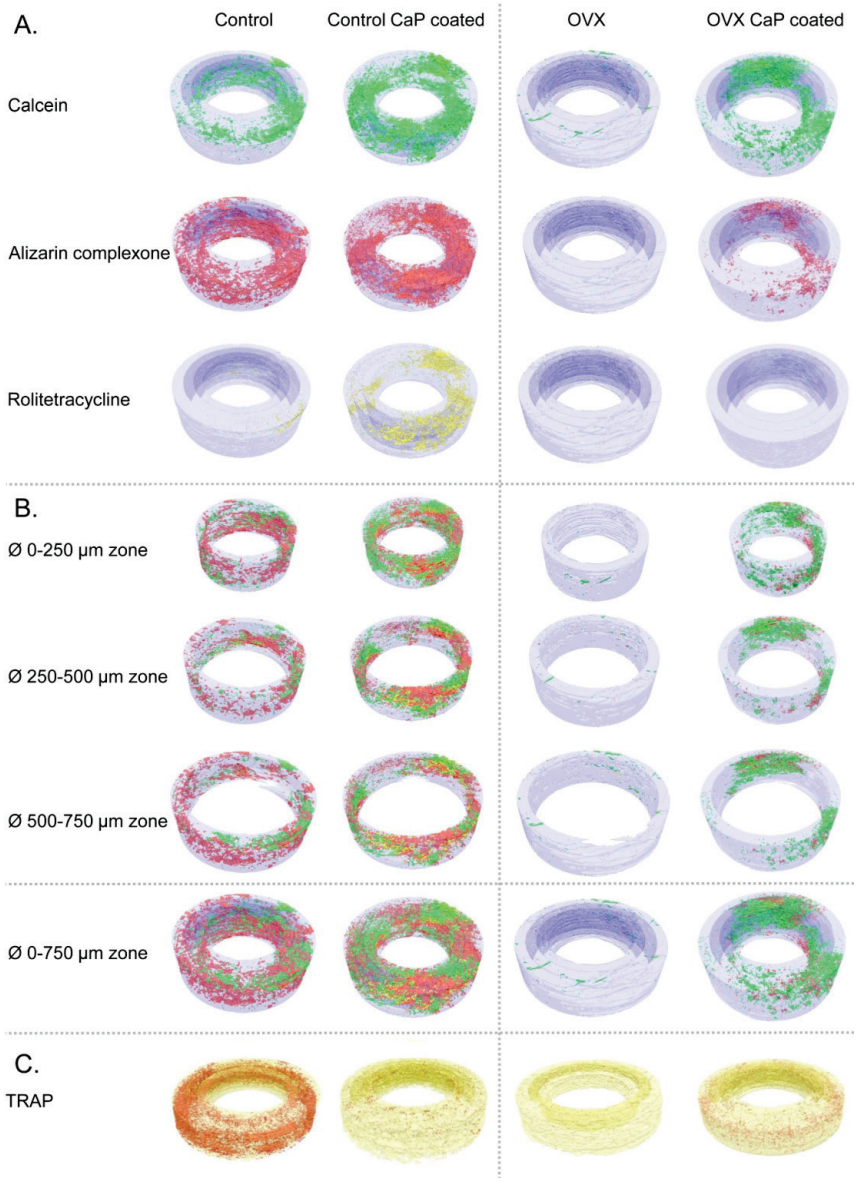


**FIGURE 7.** 3D surface reconstruction models of the fluorochrome (A,B) (calcein (green), alizarin complexone (red) and rolitetracycline (yellow)) and TRAP (C) expression (red-brown) within (A) the Ø 0-250, Ø 250-500, Ø 500-750, and Ø 0-750 µm zones (1mm height) and (B,C) separately in the Ø 0-750 µm zone from the surface of non-coated and CaP-coated Ti implants in the femoral condyle of control and osteoporotic (OVX) rats.

### 3D visualization models

Finally, a 3D model was reconstructed from the separate image stacks of the fluorescent labelled sections. Figure 7A presents the 3D surface reconstruction models of the solitary calcein, alizarin complexone, and rolitetracycline fluorochrome incorporation in the bone within the entire 0-750 μm zone from the implant surface, for both the non-coated and CaP-coated Ti implants. Figure 7B presents the same signals, however, merged for the calcein, alizarin complexone, and rolitetracycline expression, and depicted for the three different defined zone separately. Figure 7C illustrates the model of the 3D osteoclast expression (in red-brown) in all zones around the implant.

## DISCUSSION

This study aimed to assess the potential of 3D histology to gain insight into 3D bone architecture at high-resolution, including bone dynamics at the peri-implant area. Besides BV, dynamic parameters such as bone deposition and resorption were quantified using respectively fluorochrome incorporation and TRAP staining. Finally, 3D histological reconstructions were created at the peri-implant area. In general, both micro-CT and 3D histology showed a decrease in BV around the implants in OVX animals. In the control animals with CaP coated implants only, there were significant differences between the zone adjacent to the implant surface, vs. the distant zone representing the normal bone density. 3D fluorochrome volume fractions were measured to provide information about bone turnover activity.

Evidently, bone turnover was higher in the control vs. osteoporotic animals. Also, an increased fluorochrome volume was found in both types of animals around the CaP-coated implants. In the control animals, the bone turnover was more persistant over time, as indicated by higher fractions of alizarin vs. calcein. In addition, the osteoclast volume fraction was higher around the control vs. the osteoporotic animals.

Several technical remarks can be made towards the study design. For our analysis, we employed a micro-CT system. In principle, higher detail would have been possible using sub-micron (or nano-) CT systems.[20] However, such systems cannot visualize the complete 3D architecture of an entire specimen.

An additional technical remark is the selection of the analytical methods. High-resolution confocal laser scanning microscopy (CLSM) techniques, like multi-photon fluorescence microscopy (MFM) could also have been chosen to analyze samples without sectioning. However, CLSM as well as MFM have limitations in penetration depth when using bone samples.[21-23] Moy et al. described optical histology prior to CLSM, but it has to be noted that such a technique is only applicable on soft tissue, and furthermore is partially destructive.[24] On the other hand, 3D analysis and visualization combining the imaging modalities of micro-CT and histology was already shown to be applicable in multiple studies regarding bone morphology, which was the rationale for the current approach.[25-27]

When regarding the study outcomes, our micro-CT as well as histology data showed BV loss in osteoporotic animals compared to the control animals. It is known that osteoporosis alters the process of bone turnover, which can cause a significant decrease in BV and percentage of bone-implant contact.[15] Bone formation can be favored when using CaP coatings.[28] This beneficial biological effect of the ceramic coating is postulated to result from the chemical similarity between the synthetic and the natural CaP component in bone.[29] The CaP coating provides a physiochemical matrix suitable for new bone formation and stimulates cellular and intracellular signalling.[1,30] Still, it remains important to realize that, besides the positive effect of CaP coatings on bone formation, also other implant characteristics might have influenced our results, such as different surface micro- and nano-geometry between the groups. Moreover, the results might be affected to some extent by the chosen Ti alloy composition and/or design characteristics of overall implant size and shape.

Results in all previous studies were based on the use of three microscopical sections per sample and subsequent histomorpho-

metrical assessment of a 2D region-of-interest area measurement around the implant. In the current study, the entire 3D tissue volume around the implants was measured, which provides additional and corroborating information for such volume loss in osteoporotic conditions. However, the capacity of the CaP coating to enhance bone formation was only found significant for the control animals, when comparing the bone quality in the most distant zone to the zone directly adjacent to the implant surface (Figure 2B). Apparently, using a 3D measurement technique in our study did not result in a much improved detection capacity, as compared to earlier work. Thus, for the purpose of mere quantification applying a 3D method seems overly elaborate and not always as effective.

Still, the 3D measurements were also capable of supplying data on bone turnover.
Fluorescent signals, such as resulting from tetracycline incorporation, are very stable and can even be found back after thousands of years.[31] Moreover they are very sensitive, and even able to detect microdamage in bone.[32] A large range of fluorochromes can be used for polychrome labelling and detection when using spectral image analysis.[33,34] Several researchers have used fluorochromes to study bone formation around implants. For instance, Stadlinger and co-workers placed dental implants after surface conditioning with hydroxide ions. However, their fluorochrome analysis was limited, and only capable to distinguish differences in bone implant contact, but not to detect changes in bone dynamics.[35] In contrast, Guskuma et al. studied autografting around (non-coated) implants.[36] In their studies, the application of fluorochromes was found valuable, and could be applied to quantify differences in BV percentage. In a previous study in our own group, using conventional fluorescence imaging microscopy, Alghamdi et al. used analogous fluorochrome labels to study the labelled area within a 0-250 μm zone to the implant surface.[15] In that study, an increase of fluorochrome intensity was described, when using CaP coatings. Still, the measured area was based on one zone of investigation only, and used a conventional 2D view with a red-green-blue (RGB) color detection model. In the current approach, measurements were made in three separate and 3D volumes around

the implant as well as a hue-saturation-intensity (HSI) model was used to enable measurement over the entire color spectrum. In agreement with the earlier findings, higher fluorochrome expression was found in osteoporotic animals for the CaP coatings compared to non-coated implants. However, with the 3D measurements it was also possible to discern differences in the fractions of each color (representing the time of administration) and to provide insight into positioning of the signals.

Besides studying bone formation in time with the use of fluorescent labels, changes in the dynamic equilibrium of bone formation and resorption are also often studied on basis of osteoclast function, especially in the case of osteoporosis.[37,38] In our study, it was evident that osteoclasts were prominently present in healthy animals, compared to the lower levels found in the osteoporotic rats. This was consistent with the higher level of incorporated fluorochromes in healthy animals, i.e., a higher presence of osteoclasts apparently is directly linked to a higher bone turnover. Moreover, it was seen that in such healthy animals using control implants, most osteoclasts were present in the remote zone from the implant surface. In contrast, using CaP-coated implants, both the control and osteoporotic rats showed an almost uniform distribution of osteoclasts in all three measured zones. This clearly indicates that there is a shift of osteoclast activity, towards the implant surface, when using CaP coatings. Furthermore, it was striking that the amount of osteoclasts in the osteoportic animals was equal to that of normal animals, when CaP-coated implants were installed. Measurements on the presence of osteoclasts were previously also attempted in 2D models, but this did not result in significant data.[18] For future research, it would be interesting to directly link fluorochrome labels with fluorescence-based TRAP staining. However, attempts so far were found not to be suitable for *in vivo* animal systems.[39] Since bone resorption and deposition forms a continuous and dynamic process, it can be suggested that differences in the expression or localization of ostoclasts might have more pronounced consequences on bone remodeling over time. Therefore, the significance of these findings relative to long-term implant performance/function should also be determined.

Still, when regarding all our data critically, it is evident that the 3D models do not provide a lot more basic bone density data compared with 2D measurements. The additional value of a 3D model is mainly related to the observation of specific functional signals. Therefore, 3D visualization can be suggested to be very helpful in the study of bone metabolic processes. Many factors influence the osteoclast differentiation pathway, even malignant tumour cells can induce osteoclasts, and thus inhibit bone formation.[40] Furthermore, additional information on bone formation can be obtained by studying osteoblast differentiation together with visualization of mineralization makers such as osteocalcin, osteopontin, transforming growth factor β, and bone morphogenetic proteins. Efforts have already been made to do so, using either immune labeling,[4,41] or *in situ* hybridisation.[42] A final challenge remains to combine several anatomical and dynamic imaging modalities, such as microscopy or micro-CT, with micro-magnetic resonance imaging (micro-MRI) or micro-positron emission tomography (micro-PET) to study complex bone cell differentiation pathways in 3D at the peri-implant surface, and indeed focussed on long-term implant performance.

## CONCLUSION

The current study measured BV, bone remodeling, and osteoclast activity around CaP-coated bone implants in healthy and osteoporotic rats. 3D histology is a suitable technique to obtain data and visual insight into bone architecture around implants with relatively high-resolution. Bone formation was significantly reduced in osteoporotic conditions. The application of CaP coatings resulted in a higher BV directly around the implants for the osteoporotic animals, an enhanced bone turnover, and a shift of remodeling activity towards the implant surface.

## REFERENCES


1. Wilmowsky von, C., Moest, T., Nkenke, E., Stelzle, F., Schlegel, K.A., Implants in bone: Part I. A current overview about tissue response, surface modifications and future perspectives. Oral Maxillofac Surg. 2014;18:243-257.
2. Wilmowsky von, C., Moest, T., Nkenke, E., Stelzle, F., Schlegel, K.A., Implants in bone: Part II. Research on implant osseointegration : Material testing, mechanical testing, imaging and histoanalytical methods. Oral Maxillofac Surg. 2014;18:355-372.
3. Davies, J.E., Understanding peri-implant endosseous healing. J Dent m Educ. 2003;67:932-949.
4. Schouten, C., Meijer, G.J., Beucken van den, J.J., Spauwen, P.H., Jansen, J.A., Effects of implant geometry, surface properties, and TGF-beta1 on peri-implant bone response: an experimental study in goats. Clin Oral Implants Res. 2009;20:421-429.
5. Siebers, M.C., Brugge ter, P.J., Walboomers, X.F., Jansen, J.A., Integrins as linker proteins between osteoblasts and bone replacing materials. A critical review. Biomaterials. 2005;26:137-146.
6. Papalexiou, V., Novaes Jr, A.B., Grisi, M.F., Souza, S.S., Taba Jr, M., Kajiwara, J.K., Influence of implant microstructure on the dynamics of bone healing around immediate implants placed into periodontally infected sites. A confocal laser scanning microscopic study. Clin Oral Implants Res 2004;15:44-53.
7. Junker, R., Manders, P.J., Wolke, J., Borisov, Y., Jansen, J.A., Bone reaction adjacent to microplasma-sprayed CaP-coated oral implants subjected to occlusal load, an experimental study in the dog. Part I: short-term results. Clin Oral Implants Res. 2010;21:1251-1263.
8. Schouten, C., Meijer, G.J., Beucken van den, J.J., Leeuwenburgh, S.C., Jonge de, L.T., Wolke, J.G., Spauwen, P.H., Jansen, J.A., *In vivo* bone response and mechanical evaluation of electrosprayed CaP nanoparticle coatings using the iliac crest of goats as an implantation model. Acta Biomater. 2010;6:2227-2236.
9. Xie, C., Lu, H., Li, W., Chen, F.M., Zhao, Y.M., The use of calcium phosphate-based biomaterials in implant dentistry. J Mater Sci Mater Med. 2012;23:853-862.
10. Chai, W.L., Moharamzadeh, K., Brook, I.M., Noort van, R., A review of histomorphometric analysis techniques for assessing implant-soft tissue interface. Biotech Histochem. 2011;86:242-254.
11. Alghamdi, H.S., Beucken van den, J.J., Jansen, J.A., Osteoporotic Rat Models for Evaluation of Osseointegration of Bone Implants. Tissue Eng Part C Methods. 2014;20:493-505.

12. Particelli, F., Mecozzi, L., Beraudi, A., Montesi, M., Baruffaldi, F., Viceconti, M., A comparison between micro-CT and histology for the evaluation of cortical bone: effect of polymethylmethacrylate embedding on structural parameters. J Microsc. 2012;245:302-310.
13. Ho, J.T., Wu, J., Huang, H.L., Chen, M.Y., Fuh, L.J., Hsu, J.T., Trabecular bone structural parameters evaluated using dental cone-beam computed tomography: cellular synthetic bones. Biomed Eng Online. 2013;12:115-125.
14. Peyrin, F., Salome, M., Cloetens, P., Laval-Jeantet, A.M., Ritman, E., Ruegsegger, P., Micro-CT examinations of trabecular bone samples at different resolutions: 14, 7 and 2 micron level. Technol Health Care. 1998;6:391-401.
15. Alghamdi, H.S., Cuijpers, V.M., Wolke, J.G., Beucken van den, J.J., Jansen, J.A., Calcium-phosphate-coated oral implants promote osseointegration in osteoporosis. J Dent Res. 2013;92:982-988.
16. Yoshinari M, Hayakawa T, Wolke JG, Nemoto K, Jansen JA. Influence of rapid heating with infrared radiation on RF magnetron-sputtered calcium phosphate coatings. J Biomed Mater Res. 1997;37:60-67.
17. Lubbe van der, H.B., Klein, C.P., Groot de, K., A simple method for preparing thin (10 microM) histological sections of undecalcified plastic embedded bone with implants. Stain Technol. 1988;63:171-176.
18. Laak van der, J.A., Pahlplatz, M.M., Hanselaar, A.G., Wilde de, P.C., Hue-saturation-density (HSD) model for stain recognition in digital images from transmitted light microscopy. Cytometry. 2000;39:275-284.
19. Thevenaz, P., Ruttimann, U.E., Unser, M., A pyramid approach to subpixel registration based on intensity. Ieee Transactions on Image Processing. 1998;7:27-41.
20. Cuijpers, V.M., Jaroszewicz, J., Anil, S., Al Farraj Aldosari, A., Walboomers, X.F., Jansen, J.A., Resolution, sensitivity, and *in vivo* application of high-resolution computed tomography for titanium-coated polymethyl methacrylate (PMMA) dental implants. Clin Oral Implants Res. 2014;25:359-365.
21. Grotz, K.A., al-Nawas, B., Piepkorn, B., Reichert, T.E., Duschner, H., Wagner, W., [Micromorphological findings in jaw bone after radiotherapy. Confocal laser scanning microscopy and fluorescence darkfield microscopy studies]. Mund Kiefer Gesichtschir. 1999;3:140-145.
22. Smith, I.O., Ren, F., Baumann. M.J., Case, E.D., Confocal laser scanning microscopy as a tool for imaging cancellous bone. J Biomed Mater Res B Appl Biomater. 2006;79:185-192.
23. Nishikawa, T., Masuno, K., Mori, M., Tajime, Y., Kakudo, K., Tanaka, A., Calcification at the interface between titanium implants and bone:

24. observation with confocal laser scanning microscopy. J Oral Implantol. 2006;32:211-217.
25. Moy, A.J., Wiersma, M.P., Choi, B., Optical histology: a method to visualize microvasculature in thick tissue sections of mouse brain. PLoS One. 2013;8: e53753.
26. Handschuh, S., Schwaha, T., Metscher, B.D., Showing their true colors: a practical approach to volume rendering from serial sections. BMC Dev Biol. 2010;10:41-57.
27. Bernhardt, R., Kuhlisch, E., Schulz, M.C., Eckelt, U., Stadlinger, B., Comparison of bone-implant contact and bone-implant volume between 2D-histological sections and 3D-SRmicroCT slices. Eur Cell Mater. 2012;23:237-248.
28. Marchand, C., Chen, H., Buschmann, M.D., Hoemann, C.D., Standardized three-dimensional volumes of interest with adapted surfaces for more precise subchondral bone analyses by micro-computed tomography. Tissue Eng Part C Methods. 2011;17:475-484.
29. Junker, R., Manders, P.J., Wolke, J., Borisov, Y., Jansen, J.A., Bone-supportive behavior of microplasma-sprayed CaP-coated implants: mechanical and histological outcome in the goat. Clin Oral Implants Res. 2010;21:189-200.
30. Kuzyk, P.R., Schemitsch, E.H., The basic science of peri-implant bone healing. Indian J Orthop. 2011;45:108-115.
31. Surmenev, R.A., Surmeneva, M.A., Ivanova, A.A., Significance of calcium phosphate coatings for the enhancement of new bone osteogenesis--a review. Acta Biomater. 2014;10:557-579.
32. Cook, M., Molto, E., Anderson, C., Fluorochrome in Roman Period Skeletons from Dakhleh Oasis, Egypt. American Journal of Physical Anthropology. 1989;80:137-143.
33. Lee, T.C., Mohsin, S., Taylor, D., Parkesh, R., Gunnlaugsson, T., O'Brien, F.J., Giehl, M., Gowin, W., Detecting microdamage in bone. J Anat. 2003;203:161-172.
34. Pautke, C. Tischer, T., Vogt, S., Haczek, C., Deppe, H., Neff, A., Horch, H.H., Schieker, M., Kolk, A., New advances in fluorochrome sequential labeling of teeth using seven different fluorochromes and spectral image analysis. J Anat. 2007;210:117-121.
35. Pautke, C., Vogt, S., Kreutzer, K., Haczek, C., Wexel, G., Kolk, A., Imhoff, A.B., Zitzelsberger, H., Milz, S., Tischer, T., Characterization of eight different tetracyclines: advances in fluorescence bone . J Anat. 2010;217:76-82.
36. Stadlinger, B., Lode, A.T., Eckelt, U., Range, U., Schlottig, F., Hefti, T., Mai, R., Surface-conditioned dental implants: an animal study on bone formation. J Clin Periodontol. 2009;36:882-891.
37. Guskuma, M.H., Hochuli-Vieira, E., Pereira, F.P., Rangel-Garcia Junior , I., Okamoto, R., Okamoto, T., Magro Filho, O., Bone regeneration in surgically

created defects filled with autogenous bone: an epifluorescence microscopy analysis in rats. J Appl Oral Sci. 2010;18:346-353.
38. Pyo, S.W., Kim, Y.M., Kim, C.S., Lee, I.S., Park, J.U., Bone formation on biomimetic calcium phosphate-coated and zoledronate-immobilized titanium implants in osteoporotic rat tibiae. Int J Oral Maxillofac Implants. 2014;29:478-484.
39. Marco, F., Milena, F., Gianluca, G., Vittoria, O., Peri-implant osteogenesis in health and osteoporosis. Micron. 2005;36:630-644.
40. Filgueira, L., Fluorescence-based staining for tartrate-resistant acidic phosphatase (TRAP) in osteoclasts combined with other fluorescent dyes and protocols. J Histochem Cytochem. 2004;52:411-414.
41. Miyamoto, T., Suda, T., Differentiation and function of osteoclasts. Keio J Med. 2003;52:1-7.
42. Derkx, P., Nigg, A.L., Bosman, F.T., Birkenhager-Frenkel, D.H., Houtsmuller, A.B., Pols, H.A., Leeuwen van J.P., Immunolocalization and quantification of noncollagenous bone matrix proteins in methylmethacrylate-embedded adult human bone in combination with histomorphometry. Bone. 1998;22:367-373.
43. Seto, H., Aoki, K., Kasugai, S., Ohya, K., Trabecular bone turnover, bone marrow cell development, and gene expression of bone matrix proteins after low calcium feeding in rats. Bone. 1999;25:687-695.

# CHAPTER 8

## Summary, address to the aims, closing remarks and future perspectives

## Summary and address to the aims

Because of the ageing of the world population, and the associated increase in life expectancy, more people will suffer from deteriorating, failing or malfunctioning of body parts, organs or tissues. The developing field of tissue engineering aims to regenerate these deteriorated or damaged organs and tissues by combining cells with scaffold materials to guide the growth of new tissue. Intensive research over the last two decades resulted in an ever-increasing bio-mimetic set of biomaterial scaffolds to be applied in medicine.
To monitor and assess biomaterial scaffold function, biomedical imaging techniques crucial for evaluation, should also be developed in order to visualize and analyse these structures at sub-micron scale.
In tissue engineering research, high resolution X-ray imaging is still the most practical imaging modality. The aim of the present research was to explore fundamental imaging-based strategies to improve three-dimensional (3D) imaging in tissue engineering, and to enhance X-ray micro-computed tomography applications in biomaterial research.

In chapter 1, a general introduction on imaging possibilities in tissue engineering research and a description of the aims of this thesis are presented. Subsequently, the following chapters each discuss a separate research question.

1. What is the current state-of-the-art in biomaterial imaging?

This review focuses on the application of high-resolution X-ray imaging modalities, currently available for the assessment of biomaterials and (bone) tissue engineered constructs, with a specific focus on micro-computed tomography (CT) and CT-derived techniques. Also, the development, applications and limitations of both *in vivo* and *ex vivo* micro-CT imaging methods are discussed. Moreover, state-of-the-art X-ray imaging techniques, like X-ray phase contrast, scatter contrast, fluorescence contrast and hybrid X-ray

imaging are described in detail. Finally, challenging nano-resolution multi-modal *in vivo* imaging is presented. Such techniques are providing a simultaneous view into associated molecular, functional, and anatomical changes.

2. Is there a straightforward technique to pinpoint biomaterials inside a specimen to facilitate histological tissue processing?

In order to adequately process tissues from patients and animal studies, it is desirable to know the exact three-dimensional (3D) position of structures or objects within different tissue samples in relation to the specimen surface. Also, for adequate histological processing of implanted biomaterials or tissue engineered constructs, it could be essential to obtain insight into the localization of structures inside the tissue samples. Visualization of 3D surface reconstruction, including basic photorealistic texture characteristics as surface pattern and color combined with X-ray computed tomography 3D reconstruction at a different levels, is a useful approach to localize anatomical or implanted structures within experimental tissue samples. Because of the possible visualization of structures of interest in a 3D environment, fusion of these techniques can greatly facilitate histological processing.

3. Is it possible to visualize and quantify cells on a biomaterial surface in 3D with conventional scanning electron microscopy (SEM)?

In tissue engineering research, various 3D techniques are available to study cell morphology, biomaterials and their relations. To overcome disadvantages of frequently used imaging techniques, the current study proposes stereo imaging in conventional scanning electron microscopy. First, the 3D SEM application was validated using a series of standardized microspheres. Thereafter, MC-3T3 cell morphology was visualized and cell parameters as cell height were quantified on titanium and calcium phosphate materials using 3D reconstruction

software. Besides 3D visualization of the cells, quantitative assessment showed significant substrate-dependency of cell spreading in time. Such quantification of cell spreading kinetics can be used for optimization of tissue engineering scaffold surface properties. However, further standardization of SEM image acquisition and 3D SEM software settings are still essential for 3D cell analysis.

4. Is high resolution / nano-computed tomography suitable to analyze sub-micron biomaterials and biological structures in 3D?

The aim of this study was (1) to determine the spatial resolution and sensitivity of micro- versus nano-computed tomography (CT) techniques, and (2) to validate micro- versus nano-CT in a dog dental implant model, compared to histological analysis. To determine spatial resolution and sensitivity, standardized reference samples containing standardized nano- and micro-spheres were prepared in polymer and ceramic matrices. Thereafter, 10 titanium-coated polymer dental implants were placed in the mandible of Beagle dogs. Both micro- and nano-CT, as well as histological analysis were performed. The reference samples confirmed the high resolution of the nano-CT system, which was capable to reveal sub-micron structures embedded in radiodense matrices. The dog implantation study and subsequent statistical analysis showed equal values for bone area and bone-implant contact measurements between micro-CT and histology. However, because of the limited sample size and field of view, nano-CT was not rendering reliable data representative of the entire bone-implant specimen. We concluded that micro-CT analysis is an efficient tool to quantify bone healing parameters at the bone-implant interface, especially when using titanium-coated PMMA implants. Nano-CT is not suitable for such quantification, but reveals complementary morphological information rivaling histology, yet with the advantage of a 3D visualization.

5. Is it possible to enhance contrast sensitivity of radiolucent biomaterials in micro-computed tomography imaging?

The aim of this work was to introduce high resolution computed tomography (micro-CT) for scaffolds made from soft natural biomaterials, and to compare these data with the conventional techniques as scanning electron microscopy and light microscopy. Collagen-based scaffolds were used as an example. Unlike mineralised tissues, collagen scaffolds do not provide enough X-ray attenuation for micro-CT imaging. Therefore, various metal-based contrast agents were applied and evaluated using two structurally distinct scaffolds: one with round pores and one with unidirectional lamellae. The optimal contrast techniques for obtaining high-resolution three-dimensional images were either a combination of osmium tetroxide and uranyl acetate, or a combination of uranyl acetate and lead citrate. The data obtained by micro-CT analysis were in line with data obtained by light and electron microscopy. However, small structures (less than a few μm) could not be visualized due to limitation of the spot size of the micro-CT apparatus. In conclusion, reliable three-dimensional images of scaffolds prepared from soft natural biomaterials can be obtained using appropriate contrast protocols. This extends the use of micro-CT analysis to soft materials, such as protein-based biomaterials.

6. Are 3D bone dynamic studies possible with a histological approach?

Calcium phosphate (CaP) coatings can enhance the performance of bone implants in compromised conditions, such as osteoporosis. Therefore, this study compared non-coated vs. CaP coated (n=8) titanium implants in osteoporotic ovariectomized (OVX) rats. Bone volume (BV) was assessed using micro-computer tomography (micro-CT) and three-dimensional (3D) histology, in three zones from the implant surface. Bone remodeling was assessed using fluorochrome labels and osteoclast staining. Micro-CT and 3D histology showed a BV reduction in OVX animals, of respectively 22,4 and 10,5%. BV was

significantly increased inside all zones around CaP coatings, especially in the inner zone of the OVX animals. Fluorochrome labels were predominantly seen when the coating was applied. Osteoclasts were mainly found in the area remote from the surface of non-coated implants in control animals. For the coated implants, osteoclasts were distributed evenly, and present in direct vicinity of the surface. In conclusion, 3D histology is a suitable technique to obtain data and insight into bone architecture around implants at relatively high resolution. Bone formation was significantly reduced in osteoporotic animals. CaP coatings resulted in a higher bone volume directly around implants installed in osteoporotic animals, enhanced turnover, and a shift of remodeling activity towards the implant surface.

## Closing remarks and future perspectives

This thesis aimed to investigate and optimize the use of several 3D imaging modalities, especially X-ray imaging, to study cells, tissues and biomaterials in bone-tissue-engineering research.
First, in order to adequately process human and animal tissues prior to imaging, the visualization and fusion of 3D surface information with X-ray computed tomography (CT) was found to be a useful approach for the exact localization of implanted structures within experimental samples. Next, to overcome disadvantages in 3D imaging like limitations in spatial resolution, stereo imaging was proposed and was shown to be functional in conventional scanning electron microscopy, demonstrating 3D visualization of the cells. Moreover, quantitative assessment of cell spreading kinetics could easily be determined. Such information could potentially be applied for optimization of scaffold surface properties. Furthermore, the spatial resolution and contrast sensitivity of both micro- and nano-computed tomography on (sub)micron level was compared. This showed that micro-CT analysis is an efficient tool to quantify bone-healing parameters at the bone-implant interface in a practical volume of interest, whereas nano-CT reveals additional superior histology detail. Nevertheless, the restricted radio-attenuation of soft tissues and some biomaterials is a

major drawback in micro-CT imaging. Therefore we introduced an optimal contrast technique for micro-CT analysis of collagen-based scaffolds. These compounds extended the use of micro-CT analysis to soft materials, such as protein-based biomaterials. Finally, we developed a technique to study bone tissue dynamics in tissue engineering to overcome the limitation of static *ex vivo* micro-CT imaging. Our approach, applying sequential fluorochrome in an animal osteoporosis model combined with 3D histology, was demonstrated to be feasible, albeit time-consuming.

Whereas the research results are promising, major challenges still remain for further exploration of imaging-based strategies to improve 3D imaging and to enhance X-ray micro-computed tomography applications in tissue engineering and biomaterial research. Therefore, several comments should be made regarding the development of imaging modalities, the effect of several wavelengths of the electromagnetic spectrum on cells and tissues, and advances in image contrast, resolution and fusion in X-ray imaging.

As extensively described in chapter 2, imaging techniques are based on the application of different wavelengths, for example visible light and X-radiation. There is an ongoing development to construct and improve new techniques derived from existing imaging modalities, as eg. synchrotron phase-, scatter-, and fluorescence contrast imaging techniques. On the contrary, there is almost no difference in the underlying methodology of conventional microscopy and X-ray imaging. Although image contrast has extensively improved, the specificity of both above mentioned imaging techniques has barely improved. In 1686, Antoni van Leeuwenhoek illustrated bacteria, cells, tissues and other species using a primitive microscope, and fundamental microscopic determination and analysis is still essential and plays a key role in the clinical diagnosis and research today.[1-3] Van Leeuwenhoek was not aware of his important findings, as he noted: *"I'm well aware that these my writings will not be accepted by some, as they judge it to be impossible to make such discoveries…"[but] ''I will say once more that 'tis my habit to hold fast to my notions only until I'm better informed or till my observations make me go over to others…"*.[4]

Similarly, X-ray has been the gold standard for bone imaging since 1895, when it was discovered and described by Wilhelm Conrad Röntgen. The first X-ray photography of a hand taken by Röntgen was compared to an X-ray image taken of a woman's hand in the Mayo Clinic (Rochester, MN) a hundred years later (Figure 1). At first sight, the second image reveals the supremacy of current X-ray imaging. However, the improvement in image quality is almost entirely due to improved sensitivity of the radiographic film, whereas the basic technique has not changed. A 2D superposition image is still the most common.

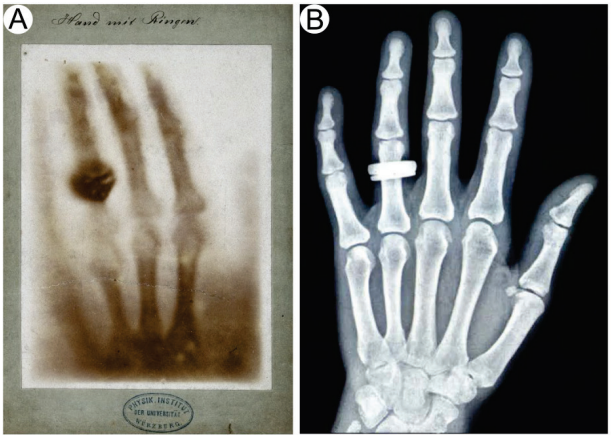


**FIGURE 1.** Historical perspectives in X-radiography. X-ray radiographs of (A) a of hand made by W.C. Röntgen on December 22, 1895 (original plate is in the Deutsche Museum, Munich, Germany), and (B) of a patient's hand made in 1995 at the Mayo Clinic ((Rochester, MN). Image courtesy of R.A.Robb.[6]

To achieve real break-troughs, more imaging modalities should be exploited, using different wavelengths from the electromagnetic spectrum, including ultrasound, magnetism and nuclear radiation. The current knowledge has already shown these to be extremely valuable in a broad range of applications in medicine, including tissue engineering research. X-ray and γ-radiation in PET and SPECT nuclear imaging are important applications to visualize and analyse structures, and track dynamic processes. However, a remark can be made on the ambivalent function of γ-radiation when applied in

medicine. Low radiation energy is successfully employed in PET and SPECT for dynamic imaging in medicine, whereas high γ-radiation doses are practical in radiotherapy to treat diseases as cancer. As a result, disadvantages as acute or late side effects, including benign and malignant processes, can be expected on the level of a large population.

For all imaging techniques described in this thesis, image contrast is fundamental. Furthermore, the interplay of contrast sensitivity and spatial resolution defines what can be achieved with these imaging techniques. Radiopaque characteristics of specimens generate contrast and therefore structures are visualized in X-ray imaging. However, contrast agents are crucial to visualize radiolucent tissues and biomaterials. Besides the development of contrast agents to improve image contrast, new "smart" contrast compounds are suitable to be applied in multiple imaging techniques such as in X-ray CT as well in MRI imaging. Moreover, these innovative compounds could be tracked in time and are to a greater extent used in the clinic to target and treat diseases. Besides the broad range of potential contrast compounds in imaging, there is a continuous improvement of both image contrast and imaging acquisition systems.

When applying micro-CT or nano-CT imaging, the relation between specimen size, field-of-view (FOV) and final image resolution must be realized. As a consequence, researchers have to find a compromise between these parameters when imaging at high resolution. The relation and discrepancy of image resolution and FOV is especially visible in *in vivo* animal micro-CT imaging versus *ex vivo* micro-CT imaging. In the first technique, the image resolution is limited due to hardware construction and short X-radiation exposure times. This is also obvious when comparing clinical human X-ray CT scanners to synchrotron X-ray imaging systems, as the resolution increases from millimetre to nanometre level.

Furthermore, the development of detailed 3D imaging in medicine could also have other applications besides direct imaging, such as the production of precise photorealistic 3D medical representations and exclusive 3D printed models. Especially in oral and maxillofacial

research, the results are valuable for clinicians and surgeons as a diagnostic tool, for preoperative planning and postoperative evaluation. In one of our studies 3D image fusion on sub-millimetre scale in tissue engineering was presented, showing 3D image fusion could possibly be applied on (sub)micron level in the near future when using various imaging techniques. Moreover, computer added tissue engineering and 3D printing of scaffolds will bring tissue engineering to a higher level in the near future.

We can conclude that each imaging technique has its strengths and weaknesses. Generally, dynamic imaging and highly sensitive imaging techniques show a low resolution compared to static imaging and high specific imaging techniques as X-ray imaging. The development of innovative emerging X-ray imaging methodologies providing anatomical as well as functional information, such as X-ray fluorescence contrast CT imaging, are progressing. Supplementary information, such as 3D element mapping using X-ray fluorescence CT imaging and 3D soft tissue contrast visualization due to phase contrast potentials, expands the exploration level in tissue engineering. These complex techniques are applied in synchrotron radiation facilities and therefore less practical. Still, the interest in multi-modal imaging is increasing. Although multimodal analyses gain complementary information, it complicates the processing and interpretation of research results. Nowadays, researchers and companies are expanding the field of (pre)clinical imaging by developing hybrid imaging systems, optimizing the present generation of systems for multimodal measurements as PET-CT, PET-SPECT-CT, and PET-MRI.

The most recent development in medical imaging is the emergence of new complementary imaging technologies. Most likely, implementing energy sources as protons or neutrons will be applied in medical imaging, including biomaterial scaffolds research. 3D proton beam tomographic imaging is already functional in monitoring proton radiation therapy in the clinical field, whereas neutron imaging, using the high attenuation ability of hydrogenous materials and the high penetrability for even heavy metals, could be a valuable tool in medical scientific investigations as tissue engineering.

After all, as the current research results on the application of 3D imaging based techniques and contrast compounds suggest, micro-CT applications will substantially contribute to improve knowledge in the field of tissue engineering.

## REFERENCES


1. Cytological examinations of Leewenhoek's first microbial specimens. Brian J. Ford. Tissue & Cell 1982 14(2) 207-217.
2. The Rotifera of Antony van Leeuwenhoek. Brian J. Ford. Reprinted from Microscopy The Journal of the Quekett Microscopical Club. Vol. 34. Part 5. Page 362-373.
3. Den Waaragtigen Omloop des Bloeds, Antoni van Leeuwenhoek, (in Dutch) 7 Sept 1688. From The project Gutenberg EBook #18929, July 28, 2006.
4. A salute to Antony van Leeuwenhoek of Delft, most versatile 17th century founding father of protistology. John O. Corliss. A. van Leeuwenhoek in letters to the Royal Society (excerpts taken from English translations given by Dobell 1932), Protist, Vol. 153, 177-190, June 2002.
5. On a new kind of rays. W.C. Röntgen. From the translations of "Ueber eine neue Art von Strahlen" in Nature by Arthus Stanton. From the Sitzungsberichte der Würzburger Physik.-medic. Gesellschaft. Würzburg, 1896, S. 1-9. Science, Feb. 14, 1896. 227-231.
6. Biomedical imaging, visualization, and analysis. R.A. Robb. Wiley-liss, Inc. Chapter 1, Historical perspectives, p3-5.

# CHAPTER 9

# Samenvatting, evaluatie van de doelstellingen, afsluitende opmerkingen en toekomstperspectieven

## Samenvatting en evaluatie van de doelstellingen

Door het steeds ouder worden van de wereldbevolking en de daaraan gerelateerde toename in levensverwachting zullen meer mensen belast worden met achteruitgaande, uitvallende of niet-werkende lichaamsdelen, organen of weefsels. Ontwikkelingen in weefselregeneratie ('tissue engineering') hebben tot doel om aangetaste of beschadigde organen en weefsels te herstellen door cellen te combineren met dragermaterialen die de regeneratie van nieuw weefsel vergemakkelijken. In de laatste twee decennia resulteerde intensief onderzoek in een voortdurende toename van gebruik van verschillende functionele dragermaterialen in de geneeskunde.
Om de functie van deze dragermaterialen te monitoren en te meten zullen biomedische beeldvormende technieken ook verder ontwikkeld moeten worden. Deze technieken zijn cruciaal om deze structuren te evalueren en op submicrometer niveau te visualiseren en analyseren.

Bij onderzoek naar tissue engineering is Röntgen beeldvorming met een hoge resolutie nog steeds de meest praktische beeldvormende techniek. Het doel van dit proefschrift was om fundamentele beeldvormende strategieën te onderzoeken om de driedimensionale beeldvorming van tissue engineering te verbeteren, en de toepassing van Röntgen microcomputertomografie in onderzoek naar biomaterialen te optimaliseren.

In hoofdstuk 1 worden de beeldvormende mogelijkheden in onderzoek naar tissue engineering geïntroduceerd en worden de doelen van dit proefschrift beschreven. Daarna wordt in elk volgend hoofdstuk een afzonderlijke onderzoeksvraag bediscussieerd.

1. Wat is de huidige status van beeldvorming van biomaterialen?

In dit hoofdstuk wordt de toepassing van verschillende hoge-resolutie beeldvormende Röntgen technieken uitgelegd, die tegenwoordig beschikbaar zijn voor evaluatie van biomaterialen en (bot)weefsel

gegenereerde constructen. Hierbij ligt de focus op microcomputer-tomografie (CT) en CT afgeleide technieken. Daarnaast worden de ontwikkelingen, toepassingen en beperkingen van zowel *in vivo* als *ex vivo* micro-CT beeldvormende methoden besproken. Vervolgens worden geavanceerde Röntgen beeldvormende technieken, zoals Röntgen fase contrast, scatter contrast, fluorescentie contrast en hybride Röntgen beeldvorming in detail beschreven. Tenslotte worden innovatieve gecombineerde *in vivo* beeldvormende technieken op nanometer resolutieniveau gepresenteerd. Deze technieken geven gelijktijdig een beeld van moleculaire, functionele, en anatomische veranderingen.

2. Is er een eenvoudige techniek om de locatie van biomaterialen in een specimen te identificeren om de histologische weefselverwerking te vergemakkelijken?

Om nauwkeurig weefsels van patiënten- en dierstudies te verwerken, is het wenselijk om de driedimensionale (3D) locatie van structuren of objecten binnenin verschillende weefsels exact te kennen in relatie met het weefsel oppervlak. Daarnaast is het voor een adequate histologische bewerking van geïmplanteerde biomaterialen en gecreëerde weefselconstructen essentieel om inzicht te krijgen waar deze structuren in het weefsel liggen. Visualisatie van het driedimensionale oppervlak met fotorealistische textuurkenmerken, zoals oppervlaktepatronen en kleur, gecombineerd met Röntgen computertomografie 3D-reconstructies op verschillende niveaus, is een uitermate geschikte toepassing om geïmplanteerde structuren in experimentele weefsels te lokaliseren.

3. Is het mogelijk om cellen, gelegen op een biomateriaal oppervlak, in 3D met conventionele scanning elektronen microscopie (SEM) te visualiseren en te kwantificeren?

In onderzoek naar tissue engineering zijn verschillende 3D-technieken beschikbaar om celmorfologie, biomaterialen en hun relaties te bestuderen. Om de nadelen van veelgebruikte beeldvormende

technieken te omzeilen, wordt in deze studie stereo-beeldvorming voorgesteld met gebruik van een conventionele SEM. Als eerste werd de 3D-SEM toepassing getoetst door verschillende gestandaardiseerde microsferen te nemen. Daarna werd de morfologie van MC-3T3 cellen op materialen van zowel titanium als calciumfosfaat gevisualiseerd. Vervolgens konden de cel parameters als celhoogte door middel van 3D-reconstructie software gemeten worden. Naast de 3D-visualisatie van de cellen toonden kwantitatieve metingen een significante substraatafhankelijkheid van de celspreiding in de tijd aan. Hierdoor kan de kwantificering van celspreiding kinetica gebruikt worden om de oppervlakte-eigenschappen van gecreëerde dragermaterialen te optimaliseren. Niettemin zijn de standaardisatie van SEM-opnamen en 3D-SEM software instellingen nog steeds essentieel voor de 3D-celanalyse.

4. Is hoge-resolutie / nano-computertomografie geschikt om biomaterialen en biologische structuren van submicrometer grootte in 3D te analyseren?

Het doel van deze studie was om (1) de spatiële resolutie en de gevoeligheid van micro-CT versus nano-CT technieken te bepalen, en (2) om micro-CT versus nano-CT te valideren met behulp van een diermodel (een model met een dentaal implantaat bij Beagles). De validatie werd vergeleken met histologische analyse. Om de spatiële resolutie en de gevoeligheid te bepalen, werden referentiesamples gemaakt van polymeer en keramiek met daarin gestandaardiseerde nano- en microsferen. Daarnaast werden 10 titanium polymethyl-methacrylaat (PMMA) gecoate dentale implantaten geplaatst in de onderkaak van de honden. Er werd naast een micro- en nano-CT analyse ook een histologische analyse verricht. De referentiesamples bevestigden de hoge resolutie van het nano-CT systeem, die submicrometer structuren ingebed in de radiodense matrices kon onthullen. De implantatiestudie in het diermodel en de opvolgende statistische analyse toonden gelijke waarden voor het botoppervlakte en de botimplantaat contactmetingen bij zowel micro-CT als histologisch onderzoek. Door de beperkte samplegrootte en het gezichtsveld gaf nano-CT echter geen betrouwbare representatieve

resultaten voor het gehele botimplantaat monster. We concludeerden dat micro-CT een efficiënt hulpmiddel is om bot-helende parameters op de overgangszone tussen het bot en implantaat te kwantificeren. Dit was met name mogelijk wanneer PMMA-implantaten gecoat met titanium gebruikt werden. Nano-CT bleek niet geschikt voor kwantificering. Daarentegen toonde deze techniek aanvullende histomorfologische informatie, waarbij tevens 3D-visualisatie mogelijk was.

5. Is het mogelijk om de contrastgevoeligheid van radiolucente biomaterialen in microcomputer tomografie te verhogen?

Het doel van dit onderzoek was om hoge-resolutie computer-tomografie (micro-CT) te introduceren voor dragermaterialen bestaande uit zachte natuurlijke biomaterialen, en om deze resultaten te vergelijken met conventionele technieken als scanning elektronen microscopie en licht microscopie. Als voorbeeld werden dragermaterialen van collageen gebruikt. In tegenstelling tot gemineraliseerd weefsel geeft collageen onvoldoende vertraging van Röntgenstralen bij gebruik van micro-CT. Daarom werden verschillende op metaal gebaseerde contrastmiddelen toegepast en geëvalueerd. Er werd gebruik gemaakt van twee structureel verschillende collagene dragermaterialen: één met poreuze holten en één met parallel gelegen lamellen. De meest optimale contrasttechniek waarbij hoge-resolutie driedimensionale beelden werden verkregen, was of een combinatie van osmium tetroxide en uranyl acetaat, of een combinatie van uranyl acetaat en lood citraat. De verkregen micro-CT gegevens waren in overeenstemming met de resultaten verkregen door licht- en elektronenmicroscopie. Niettemin konden geen kleine structuren (kleiner dan enkele micrometer) gevisualiseerd worden door de beperking van de '*spot-size*' van de Röntgenbron van het micro-CT systeem. De conclusie is dat er betrouwbare driedimensionale beelden van natuurlijke dragermaterialen verkregen kunnen worden door gebruik te maken van op maat gemaakte contrast protocollen. Hierdoor wordt het gebruik van micro-CT voor zacht radiolucent materiaal uitgebreid, zoals voor visualisatie van

biomaterialen bestaande uit eiwitten.

6. Zijn driedimensionale bot dynamische studies mogelijk met een histologische benadering?

Calciumfosfaat (CaP) coatings kunnen de werking verhogen van implantaten geplaatst in aangetast bot, zoals bij osteoporose. Daarom vergeleek deze studie niet-gecoate versus CaP gecoate (n=8) titanium implantaten in osteoporotische ratten waarvan de ovaria waren verwijderd (OVX). Het bot volume (BV) werd gemeten door middel van microcomputertomografie (micro-CT) en driedimensionale (3D) histologie in drie zones vanaf het implantaatoppervlak. De botopbouw werd geanalyseerd met behulp van fluorochroom labels en een osteoclast kleuring. Micro-CT en 3D-histologie toonden een BV afname bij de OVX dieren van respectievelijk 22,5 en 10,5%. Het BV was significant toegenomen binnen alle zones bij de CaP coatings, met name in de binnenste zone bij de OVX dieren. De fluorochroom labels waren overwegend waarneembaar als er een coating toegepast was. Osteoclasten werden hoofdzakelijk gevonden bij de controle dieren met niet-gecoate implantaten, namelijk in het gebied met de grootste afstand tot het implantaatoppervlak. Bij de gecoate implantaten werden de osteoclasten gelijkmatig verdeeld gevonden, met name aanwezig in de nabijheid van het oppervlak. De conclusie is dat 3D-histologie een geschikte techniek is om met een relatief hoge resolutie data en inzicht te verkrijgen in de botarchitectuur rond implantaten. De botvorming was significant afgenomen bij de dieren met osteoporose. De CaP-coatingen resulteerden in een hoger botvolume direct om de implantaten geplaatst in de osteoporotische dieren, een verhoogde botomzetting, en een verplaatsing van botvernieuwing richting het implantaatoppervlak.

## Afsluitende opmerkingen en toekomst perspectieven

Dit proefschrift had ten doel om verschillende 3D-beeldvormende modaliteiten te onderzoeken en te optimaliseren, met name Röntgen beeldvorming, om cellen, weefsels en biomaterialen in regeneratief

botweefsel te onderzoeken. Als eerste bleek de visualisatie en fusie van 3D-oppervlakteinformatie samen met Röntgen computertomografie (CT) een succesvolle aanpak te zijn om de exacte lokalisatie van geïmplanteerde structuren, voorafgaand aan het verwerken van weefsels, te bepalen. Daarna werd vanwege beperkingen bij gebruik van sommige 3D-beeldvormende technieken, zoals de geringe spatiële resolutie, stereo-beeldvorming voorgesteld. Deze methode bleek bruikbaar te zijn in conventionele scanning elektronen microscopie en hiermee werd 3D-visualisatie van cellen gedemonstreerd. Bovendien was het eenvoudig om kwantitatieve metingen van celspreiding kinetica te verrichten. Deze informatie kan eventueel toegepast worden om de oppervlakte eigenschappen van dragermaterialen te optimaliseren. Daarnaast werden de spatiële resolutie en contrastgevoeligheid van zowel micro- als nano-CT op (sub)micrometer niveau vergeleken. Deze vergelijking toonde dat micro-CT analyse een efficiënt hulpmiddel is om binnen een volume van interesse bot helende parameters te kwantificeren die gelegen en functioneel zijn bij de overgang tussen het bot en het implantaat. Nano-CT liet echter zelfs histologisch detail zien. Desalniettemin is de geringe vertraging van radiogolven bij zachte weefsels en sommige biomaterialen een nadeel bij de micro-CT beeldvorming. Daarom introduceerden we een optimale contrasttechniek voor micro-CT analyse van dragermaterialen opgebouwd uit collageen. Deze chemische verbindingen breiden de mogelijkheden van het gebruik van micro-CT analyse uit naar zachte materialen, zoals biomaterialen bestaande uit eiwitten. Om de beperkingen van statische *ex vivo* micro-CT beeldvorming te verbeteren, ontwikkelden we uiteindelijk een techniek om dynamisch regeneratief botweefsel te bestuderen. Onze benadering om sequentieel fluorochromen in een osteoporose diermodel toe te passen, gecombineerd met 3D-histologie, was realiseerbaar, maar zeer tijdrovend.

Ondanks dat de onderzoeksresultaten veelbelovend zijn, blijven er belangrijke uitdagingen bestaan in op beeldvorming gebaseerde methoden, om 3D-beeldverwerkende methoden en Röntgen microcomputertomografie toepassingen in tissue engineering en onderzoek naar biomaterialen te verbeteren. Daarom dienen enkele

opmerkingen gemaakt te worden over de ontwikkeling van beeldverwerkende modaliteiten, het effect van de verschillende golflengten van het elektromagnetisch spectrum op cellen en weefsels, en ontwikkelingen van beeld contrast resolutie en fusie in Röntgen beeldvorming.

Zoals uitgebreid beschreven is in hoofdstuk 2 zijn beeldvormende technieken gebaseerd op de toepassing van verschillende golflengten, zoals zichtbaar licht en Röntgenstraling. Er bestaat een voortdurende ontwikkeling en verbetering van nieuwe technieken die afgeleid zijn van bestaande beeldvormende modaliteiten, bijvoorbeeld synchrotron fase contrast, scatter contrast en fluorescentie contrast. Aan de andere kant is er bijna geen verschil tussen de onderliggende methode van conventionele microscopie en Röntgen beeldvorming. Ondanks dat het beeldcontrast nu sterk verbeterd is, is de specificiteit van beide bovengenoemde beeldvormende technieken nauwelijks verbeterd. Zo beschreef Antoni van Leeuwenhoek al in 1686 met behulp van een primitieve microscoop bacteriën, cellen en weefsels, en speelt fundamentele microscopische determinatie en analyse nog steeds een essentiële rol bij de klinische diagnose en onderzoek.[1-3] Van Leeuwenhoek was zich niet bewust van zijn belangrijke bevindingen. Hij noteerde: *"Ik ben me bewust dat deze beschrijvingen niet door iedereen geaccepteerd worden, omdat ze oordelen dat het onmogelijk is om zulke ontdekkingen te doen.."[maar] "Ik zeg nog een keer dat het mijn gewoonte is om vast te houden aan mijn bevindingen totdat ik beter geïnformeerd ben of dat ik mijn observaties moet herzien…"*.[4] Hetzelfde geldt voor de beeldvorming van bot door middel van Röntgenstraling, ontdekt en beschreven door Wilhelm Conrad Röntgen, en nog steeds de gouden standaard sinds 1895. Figuur 1 vergelijkt de eerste Röntgenfoto van de hand van Röntgens vrouw met een Röntgenfoto van de hand van een vrouw genomen in the Mayo Kliniek (Rochester, MN) honderd jaar later. Op het eerste gezicht laat de tweede foto de superioriteit zien van de huidige Röntgenopname, maar de vooruitgang in beeldkwaliteit is bijna geheel te danken aan de verbetering van de gevoeligheid van de radiografische film, terwijl de techniek fundamenteel onveranderd is. Een tweedimensionaal

superpositioneel Röntgenbeeld is nog steeds de meest voorkomende beeldvormende techniek.

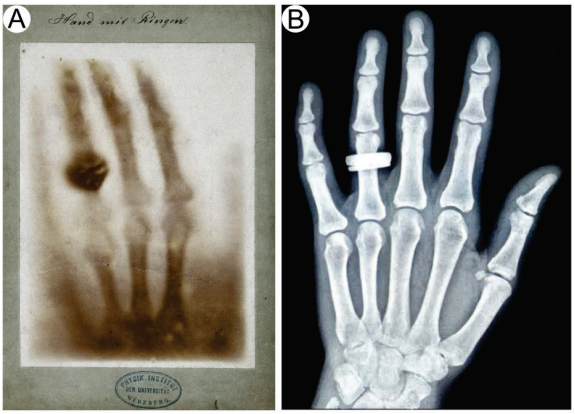


**FIGUUR 1.** Röntgen radiografie in historisch perspectief. (A) Röntgenfoto van een hand gemaakt door W.C. Röntgen op 22 December 22, 1895, (originele foto is in het Deutsche Museum, München, Duitsland) en (B) een foto van een hand van een patiënt gemaakt in 1995 in de Mayo Clinic (Rochester, MN) 100 jaar later. Foto R.A.Robb.[6]

Om een echte doorbraak te bereiken dienen meerdere beeldvormende modaliteiten onderzocht te worden die gebruik maken van verschillende golflengten van het elektromagnetische spectrum, zoals echografie, magnetisme en nucleaire reacties. Deze modaliteiten kunnen zeer waardevol zijn in een breed scala aan toepassingen in de geneeskunde, en daarom ook in onderzoek naar tissue engineering. Röntgen- en gammastraling in de nucleaire beeldvormende technieken *positron emission tomography* (PET) en *single-photon emission computed tomography* (SPECT) zijn belangrijke toepassingen om structuren te visualiseren en analyseren, en om dynamische processen te volgen. Desalniettemin dient een opmerking geplaatst te worden bij de ambivalente werking van gammastraling in de geneeskunde. Een lage dosis gammastraling wordt succesvol toegepast in PET en SPECT voor dynamische beeldvorming in geneeskunde, terwijl aan de andere kant hoge doses gammastraling in de praktijk worden toegepast bij radiotherapie om ziekten als kanker te behandelen. Hierdoor kunnen verschillende nadelen, zoals acute of

late bijeffecten, maar ook goedaardige en kwaadaardige processen, op termijn verwacht worden.

Voor alle in dit proefschrift beschreven beeldvormende technieken is beeldcontrast fundamenteel. Bovendien bepalen zowel de contrastgevoeligheid als de spatiële resolutie wat uiteindelijk de beeldkwaliteit is van de gebruikte beeldvormende techniek. Bij Röntgen worden radiogolven sterk vertraagd als het sample radiopaque is. De verschillende vertragingen genereren contrast waardoor structuren uiteindelijk gevisualiseerd kunnen worden. Toch zijn contrastmiddelen noodzakelijk om juist radiotransparante weefsels en biomaterialen te visualiseren. Naast de ontwikkeling van contrastmiddelen om beeldcontrast te verbeteren, zijn "slimme" contrastverbindingen beschikbaar die toegepast worden in meerdere beeldvormende technieken zoals in Röntgen CT en in *magnetic resonance imaging* (MRI). Bovendien kunnen deze innovatieve verbindingen in de tijd gevolgd worden, wat ze in de kliniek bruikbaar maakt om ziekten op te sporen en te behandelen. Naast het brede scala aan potentiële contrastverbindingen voor beeldvorming is er een continue verbetering van zowel het beeldcontrast als van de beeldvormende systemen.

Als men micro-CT of nano-CT beeldvorming gebruikt, moet men zich bewust zijn van de relatie tussen de objectgrootte, de grootte van het gezichtsveld en de uiteindelijke beeldresolutie. Dit heeft als consequentie dat onderzoekers een compromis moeten vinden tussen deze parameters wanneer er een hoge-resolutie beeldvervormende techniek wordt toegepast. De relatie en discrepantie van de beeldresolutie en het gezichtsveld is met name zichtbaar bij *in vivo* micro-CT systemen ten behoeve van dierstudies, versus *ex vivo* micro-CT, waarbij in de eerste techniek de beeldresolutie beperkt wordt door de hardware constructie en korte Röntgen bestralingstijden. Dit is ook duidelijk als menselijke Röntgen CT-scanners vergeleken worden met synchrotron gebaseerde Röntgensystemen: de resolutie neemt dan toe van millimeter tot nanometer niveau.

Verder kan de ontwikkeling van gedetailleerde 3D-beeldvorming in de geneeskunde ook andere toepassingen hebben naast directe

beeldvorming, zoals het maken van exacte fotorealistische 3D-modellen en exclusieve 3D-geprinte modellen. Met name bij oraal en maxillofaciaal onderzoek zijn deze resultaten waardevol voor clinici en chirurgen. Deze technieken kunnen dan een diagnostisch hulpmiddel zijn bij preoperatieve planning en postoperatieve evaluatie. In één van onze studies werd de fusie van 3D-beelden op submillimeter niveau in tissue engineering gepresenteerd, wat aangeeft dat de fusie van 3D-beelden in de toekomst toegepast kan worden bij verschillende beeldvormende technieken op (sub)micrometer niveau. Bovendien zullen computergestuurde weefselfabricaten en 3D-geprinte dragermaterialen de weefseltechnologie in de nabije toekomst naar een hoger niveau tillen.

We kunnen concluderen dat elke beeldverwerkende techniek zijn eigen sterke en zwakke punten heeft. In het algemeen tonen dynamische en hooggevoelige beeldvormende technieken een lagere resolutie vergeleken met statische en hoog specifieke beeldvormende technieken als Röntgen beeldvorming. Er zijn tegenwoordig vooruitstrevende innovatieve ontwikkelingen die van Röntgen beeldvorming zijn afgeleid, zoals Röntgen fluorescentie contrast CT, welke zowel anatomische als functionele informatie kan opleveren. Aanvullende informatie, zoals het in kaart brengen van elementen in 3D door middel van Röntgen fluorescentie CT en 3D-visualisatie van zacht weefsel door fasecontrast CT-methoden, breiden de mogelijkheden van onderzoek naar tissue engineering uit. Helaas worden deze complexe technieken hoofdzakelijk toegepast in synchrotron faciliteiten en zijn daarom minder toepasbaar in de praktijk. Bovendien leveren complexe beeldvormende systemen complementaire informatie, wat de verwerking en interpretatie van onderzoeksresultaten bemoeilijkt. Desondanks neemt de interesse in samengestelde beeldvormende technieken nog steeds toe. Daardoor breiden onderzoekers en bedrijven tegenwoordig het preklinisch onderzoeksveld uit naar de ontwikkeling van hybride beeldverwerkende systemen, waarbij ook de huidige generatie meervoudige beeldvormende systemen, zoals PET-CT, PET-SPECT-CT en PET-MRI, geoptimaliseerd worden.

De meest recente ontwikkeling in medische beeldvorming zijn nieuwe complementaire beeldvormende technieken. Technieken die protonen of neutronen als energiebronnen gebruiken zullen regelmatig toegepast worden in medische beeldvorming, ook voor onderzoek naar biomaterialen. Zo wordt 3D computertomografie met behulp van een protonenstraal al klinisch toegepast bij het monitoren van protonen bestralingstherapie en kan beeldvorming met behulp van neutronen een waardevol hulpmiddel zijn bij wetenschappelijk onderzoek in de geneeskunde, inclusief onderzoek naar tissue engineering. Bij beeldvorming met behulp van neutronen wordt gebruik gemaakt van de hoge vertraging van neutronen door waterhoudende materialen en een hoge mate van doordringbaarheid van zware metalen.

Concluderend kan worden gesteld dat de huidige onderzoeksresultaten van 3D-beeldvormende technieken en contrastmiddelen laten zien dat micro-CT toepassingen een substantiële bijdrage leveren aan het uitbreiden van de kennis op het gebied van tissue engineering.

## REFERENTIES


1. Cytological examinations of Leewenhoek's first microbial specimens. Brian J. Ford. Tissue & Cell 1982 14(2) 207-217.
2. The Rotifera of Antony van Leeuwenhoek. Brian J. Ford. Reprinted from Microscopy The Journal of the Quekett Microscopical Club. Vol. 34. Part 5. Page 362-373.
3. Den Waaragtigen Omloop des Bloeds, Antoni van Leeuwenhoek, (in Dutch) 7 Sept 1688. From The project Gutenberg EBook #18929, July 28, 2006.
4. A salute to Antony van Leeuwenhoek of Delft, most versatile 17th century founding father of protistology. John O. Corliss. A. van Leeuwenhoek in letters to the Royal Society (excerpts taken from English translations given by Dobell 1932), Protist, Vol. 153, 177-190, June 2002.
5. On a new kind of rays. W.C. Röntgen. From the translations of "Ueber eine neue Art von Strahlen" in Nature by Arthus Stanton. From the Sitzungsberichte der Würzburger Physik.-medic. Gesellschaft. Würzburg, 1896, S. 1-9. Science, Feb. 14, 1896. 227-231.
6. Biomedical beeldvorming, visualization, and analysis. R.A. Robb. Wiley-liss, Inc. Chapter 1, Historical perspectives, p3-5.

# Acknowledgements (Dankwoord)
# Curriculum Vitae
# List of Publications

# Acknowledgements (Dankwoord)

Het einde kroont het werk. Een proefschrift eindigt vanzelfsprekend met een woord van dank. Natuurlijk was deze thesis zonder de hulp van vele enthousiaste collega's niet tot stand gekomen.

Als kind was ik al gefascineerd door het ongrijpbare van de micro- en macrokosmos. Vakanties bracht ik zoekend naar mineralen en fossielen door en 's nachts tuurde ik door een telescoop, gekregen in het laatste jaar van de basisschool. Hierbij ging mijn interesse vooral uit naar gebieden die het voorstellingsvermogen te boven gaan, zoals dimensies in ruimte en tijd. Deze fascinatie heeft in hoge mate invloed gehad op mijn studiekeuze en de verdere ontwikkeling van mijn werk op de Radboud Universiteit, met als resultaat dit proefschrift.

Voorafgaand aan mijn werk op het laboratorium van Biomaterialen van de faculteit Tandheelkunde, waar dit proefschrift is volbracht, ben ik als research analist betrokken geweest bij verschillende onderzoeksprojecten van de afdeling Pathologie. Hier werd in de loop van de jaren mijn interesse gewekt voor de derde dimensie van cellen, weefsels en organen op microscopisch niveau. Het was anatoom dr. Albert Verhofstad (†2008) die mij destijds stimuleerde en de mogelijkheid gaf om dit onderwerp verder te doorgronden. Hiervoor ben ik hem enorm dankbaar.

Wie had kunnen denken dat een treinreis naar een cursus Moleculaire Technieken een overgang naar het laboratorium van Biomaterialen van de afdeling Tandheelkunde zou kunnen betekenen? Mijn ontmoeting met de voormalig hoofdanaliste van dit lab, Anja de Ruijter, inmiddels Operationeel Manager Tandheelkunde, betekende een verandering van werkzaamheden naar het gebied van 'image analysis' en driedimensionale beeldverwerkende technieken, waaronder microcomputertomografie. Beste Anja, bedankt voor de mogelijkheid tot zelfontplooiing op het laboratorium van Biomaterialen.

Na vele Bachelor- en Masterstudenten ondersteund te hebben bij hun onderzoeken, heb ik begin 2010 prof. dr. John Jansen gevraagd naar de mogelijkheid om een eigen thesis te publiceren. Mijn dank gaat dan ook het eerst uit naar prof. dr. John Jansen. Ik ben hem ontzettend dankbaar dat hij mij, met niet meer dan een BSc op zak, de gelegenheid heeft gegeven om aan dit promotieonderzoek te werken, naast mijn bestaande werkzaamheden op de afdeling. Beste John, de zeer constructieve periodieke bijeenkomsten over onderwerpen van het promotieonderzoek hebben enorm bijgedragen aan een relatief soepel gelopen PhD traject. Ik ben je zeer dankbaar voor alle hulp om mijn eigen vermogens verder te ontwikkelen. Jouw kennis en ervaring vormen nog steeds een grote inspiratie voor mij.

Beste dr. X. Frank Walboomers, beste Frank, voor mij ben je veel meer dan een copromotor. Ik kon altijd bij je terecht met allerlei vragen en voor ondersteuning op elk vlak. Van jouw uitgebreide kennis van vele vakgebieden heb ik enorm veel geleerd. Je leerde me de focus te leggen en wetenschappelijke publicaties te schrijven. Mede dankzij jouw onvoorwaardelijke steun heb ik dit proefschrift uiteindelijk tot een goed einde weten te brengen. Ik ben blij dat je zowel mijn copromotor als collega bent. Zonder jou was er geen thesis tot stand gekomen, waarvoor ik je enorm dankbaar ben.

Daarnaast hebben de overige stafleden van het laboratorium van Biomaterialen een belangrijke rol gespeeld. Dr. Joop Wolke, Dr. Sander Leeuwenburgh, Dr. Jeroen van der Beucken, Dr. Fang Yang, Dr. Jan-Willem Hoekstra en Dr. Bart van Oirschot, ik wil jullie allemaal hartelijk danken voor alle kennis en ervaring op het gebied van de chemie, biologie, fysica en geneeskunde die jullie me hebben bijgebracht. Ik heb ontzettend veel van jullie geleerd.

Ook heb ik enorm veel waardering voor mijn collega's die de basis vormen van een goed functionerend laboratorium van Biomaterialen, het analytisch ondersteunend personeel.
Beste Martijn, je staat altijd voor iedereen klaar. Ook ik kon gebruik maken van jouw uitgebreide expertise op het gebied van CaP scaffolds en scanning elektronen microscopie. Bedankt voor alle hulp en

natuurlijk de steun als paranimf.
Natasja, dank je voor alle hulp bij de weefsel verwerking en inzet voor het 3D histologie onderzoeksproject. Ik ken weinig mensen met zo'n loyaliteit.
Monique, dank voor alle antwoorden op mijn vragen over moleculaire biologie en natuurlijk voor de nodige structuur op het lab.

De fusering van enkele onderzoeksgroepen bracht ook nieuwe collega's. René, Pia, Marjon en Jan, dank voor de plezierige samenwerking op het lab. Frank, Hans en Jaap, bedankt voor de ondersteuning op allerhande gebieden.

Door de goede sfeer op de afdeling ben ik altijd met veel plezier naar mijn werk gegaan. Dit kwam onder andere door de prettige samenwerking met vele enthousiaste collega's uit bijna alle Europese landen, Noord- en Zuid Amerika (Verenigde Staten, Canada, Brazilië, Columbia), Afrika (Egypte, Soedan), Azië (China, Japan, Singapore, Indonesië, Saoedi-Arabië, Pakistan, Iran, Irak, Pakistan, Azerbeidjaan, Armenië, Turkije, Oekraïne) en Australië. Naast de verkregen kennis, hebben deze collega's mij een rijker mens gemaakt door mij meer inzicht te geven in hun verschillende sociaal-culturele en religieuze achtergronden.

Numerous colleagues have finalized their doctoral degree during my presence in the laboratory of Biomaterials. A relatively long list: Hamdan Alghamdi, Wanxun Yang, Arnold Nijhuis, Manuela Ventura, Na Yu, Kemal Sariibrahimoglu, Huanan Wang, Jinling Ma, Timothy Douglas, Alexey Klymov, Matilde Bongio, Wei Ji, Xiangzhen Yan, Jie An, Adelina Plavachova, Corinne Schouten, Ljupcho Prodanov, Meike van der Zande, Walter Loesberg, Lise de Jonge, Esther Bodde, Dennis Link, Afsheen Tabassum, Wouter Habraken, Sanne Both, Edwin Lamers, Daniel Oortgiesen, Xinjie Cai, Sander Grefte, Jochem Verstappen, Ruggero Bosco, Ditte Lundvig and Rudiger Junker. Nowadays, they work in different disciplines: in professional education, leading companies or top research institutes. Their personal development was a great incentive to go ahead in the field of imaging in tissue engineering. Currently, more than a few colleagues are working on their PhD. Winston Camargo, Muhanad Ali, Sónia de Lacerda Schickert,

Eline-Claire Grosfeld, Hatice Imran Gungordu, Irene Lodoso Torrecilla, Nathan Kucko, Robin Nadar, Jinlong Shao, Jiankang Song, Hongbo Tang, Roel op 't Veld, Yang Zhang, Daniela Petre, Eva Urquía Edreira, Astghik Hayrapetyan, Kambiz Farbod, Antonio Goncalves de Brito Castro, Simone Mastrogiacomo, Nehar Celikkin, Niels Cremers, Corien Oostendorp, Aysel Mammadova, Kriti Khandelwal, Bing Wang, Jiamian Wang, Mani Diba, Claire van Houdt, Laury Roa Fuentes, and Paola Carvajal Monroy, I want to thank you all for the pleasant teamwork and wish you all the best in the future.

Voor het promotieonderzoek heb ik naast collega's op de afdeling Tandheelkunde ook bijzonder prettig kunnen samenwerken met medewerkers van de afdelingen Orthopedie, Pathologie en Biochemie van de Radboud Universiteit. Dit kwam de kwaliteit van mijn thesis absoluut ten goede. Dr. Kaeuis Faraj, Ronnie Wismans en Dr. Toin van Kuppevelt van de afdeling Biochemie, bedankt voor de samenwerking op het gebied van contrastmiddelen voor radiolucente materialen (hoofdstuk 6). Dr. Ewald Bronkhorst, dank voor de hulp bij de statistiek.

International collaboration was absolutely essential in order to publish scientific articles related to this thesis. Therefore, I would like to thank Dr. Wojciech Święszkowski and Dr. Jakub Jaroszewicz (Warsaw University of Technology, Faculty of Materials Science and Engineering, Biomaterials Group, Warsaw, Poland) for the fruitful support on micro- and nano-CT analysis, resulting in several publications (Chapter 5 and 7). Moreover, thanks to Prof. dr. Anil Sukumaran, Dr. Hamdan Alghamdi and Dr. Abdullah Al Farraj Aldosari (College of Dentistry, Division of Periodontics, Riyadh, Saudi Arabia) for the rewarding cooperation on scientific publications (Chapter 5 and 7) and the introduction to the College of Dentistry of the King Saud University.

Daarnaast wil ik de medewerkers van het secretariaat, Kim Hendriks-Geijsberts, Monique Hermsen-Smeets, Vera Koert en Henriette Burgers, hartelijk danken voor de secretariële ondersteuning. Daarnaast dank ik hen ook voor de verrassende dagjes uit, Nieuwjaarsdiners en alle andere spandiensten.

Nicolai Giling, Harrie de Beijer en Richard Akkermans, dankzegging voor de goede bedrijfsvoering.

Dr. H. Jung en Dr. M. Sedelaar, bedankt voor jullie expertise.

Tenslotte wil ik me nog richten tot mijn ouders die voor mij de basis hebben gelegd. Lieve pa en ma, jullie hebben me al op jonge leeftijd alle mogelijkheden geboden voor mijn verdere persoonlijke ontwikkeling. Dank voor de harmonieuze jeugd en oneindige steun. Ook dankzegging aan mijn broer en zus, alle andere familieleden en vrienden voor alle belangstelling voor mijn werk op de Radboud Universiteit.

Als laatste wil ik de meest belangrijke personen in mijn leven bedanken: mijn vrouw en kinderen. Savannah en Youri, vaak meegenomen naar afgelegen oorden om mineralen en fossielen te zoeken, jullie hebben mijn leven enorm verrijkt. Ik ben enorm trots en blij dat jullie nu zelfstandig verder kunnen. Daarom wens ik jullie het allerbeste en heel veel geluk met jullie partners Wouter en Patricia.

Tenslotte, lieve Angélica, bedankt voor jouw onvoorwaardelijke steun en liefde. Je geeft me hoop, plezier en bent mijn steun en toeverlaat. Hopelijk mogen we nog lang van elkaar genieten.
Onze liefde is als één ziel in twee lichamen, ik hou van je.

# List of publications

## Related to this thesis

1. Three-dimensional localization of implanted biomaterials in anatomical and histological specimens using combined X-ray computed tomography and three-dimensional surface reconstruction: a technical note. **Cuijpers, V.M.**, Walboomers, X.F., Jansen, J.A., Tissue Eng Part C Methods. 2010 Feb;16(1):63-9.

2. Scanning electron microscopy stereo-imaging for three-dimensional visualization and analysis of cells in tissue-engineered constructs: technical note. **Cuijpers, V.M.**, Walboomers, X.F., Jansen, J.A., Tissue Eng Part C Methods. 2011;17(6):663.

3. Resolution, sensitivity, and *in vivo* application of high-resolution computed tomography for titanium-coated polymethyl methacrylate (PMMA) dental implants. **Cuijpers, V.M.**, Jaroszewicz, J., Anil, S., Al Farraj Aldosari, A., Walboomers, X.F., Jansen, J.A., Clin Oral Implants Res. 2014;25(3):359.

4. Micro-computed tomographical imaging of soft biological materials using contrast techniques. Faraj, K.A., **Cuijpers, V.M.**, Wismans, R.G., Walboomers, X.F., Jansen, J.A., Kuppenvelt van, T.H., Daamen, W.F., Tissue Eng Part C Methods. 2009;15(3):493.

5. Osteogenesis around CaP-coated titanium implants visualized using 3D histology and micro-computed tomography. **Cuijpers V.M.,** Alghamdi, H.S., Dijk van, N.W., Jaroszewicz, J., Walboomers, A.F., Jansen, J.A., J Biomed Mater Res A. 2015 J Biomed Mater Res Part A 2015, Nov;103(11):3463-73

## Other publications

6. Injectable self-gelling composites for bone tissue engineering based on gellan gum hydrogel enriched with different bioglasses. Douglas, T.E., Piwowarczyk, W., Pamula, E., Liskova, J., Schaubroeck, D., Leeuwenburgh, S.C., Brackman, G., Balcaen, L., Detsch, R., Declercq, H., Cholewa-Kowalska, K., Dokupi, l.A., **Cuijpers, V.M.**, Vanhaecke, F.,

Cornelissen, R., Coenye, T., Boccaccini, A.R., Dubruel, P., Biomed Mater. 2014;9(4):045014. doi: 10.1088/1748-6041/9/4/045014.

7. Osseointegration of oral implants after delayed placement in rabbits: a microcomputed tomography and histomorphometric study. Anil, S., **Cuijpers, V.M.**, Preethanath, R.S., Al Farraj Aldosari, A., Jansen, J.A., Int J Oral Maxillofac Implants. 2013;28(6):1506.

8. Calcium-phosphate-coated oral implants promote osseointegration in osteoporosis. Alghamdi, H.S,. **Cuijpers, V.M.**, Wolke, J.G., Beucken van den, J.J., Jansen, J.A., J Dent Res. 2013;92(11):982.

9. The biological performance of injectable calcium phosphate/PLGA cement in osteoporotic rats. Watering van de, F.C., Laverman, P., **Cuijpers, V.M.,** Gotthardt, M., Bronkhorst, E.M., Boerman, O.C., Jansen, J.A., Beucken van den, J.J., Biomed Mater. 2013;8(3):035012. doi: 10.1088/1748-6041/8/3/035012. Epub 2013 Apr 26.

10. Processing and *in vivo* evaluation of multiphasic calcium phosphate cements with dual tricalcium phosphate phases. Lopez-Heredia, M.A., Bongio, M., Bohner, M., **Cuijpers, V.M**,, Winnubst, L.A., Dijk van, N., Wolke, J.G., Beuckan van den, J.J., Jansen. J.A., Acta Biomaterialia. 2012;8:3500.

11. Validation of micro-CT against the section method regarding the assessment of marginal leakage of sealants. Chen, X., **Cuijpers, V.M.**, Fan, M.W., Frencken, J.E., Aust Dent J. 2012;57(2):196.

12. Bone formation analysis: effect of quantification procedures on the study outcome. Lopez-Heredia, M.A., Bongio, M., **Cuijpers, V.M.**, Dijk van, M.W., Beucken van den, J.J., Wolke, J.G., Jansen, J.A., Tissue Eng Part C Methods. 2012;18(5):369.

13. *In-vivo* generation of bone via endochondral ossification by *in vitro* chondrogenic priming of adult human and rat mesenchymal stem cells. Farrell, E., Both, S.K., Odörfer, K.I., Koevoet, W., Kops, N., O'Brien, F.J., Baatenburg Jong de, R.J., Verhaar, J.A., **Cuijpers, V.M.,** Jansen, J.A., Erben, R.G., Osch van, G.J., BMC Musculoskelet Disord. 2011;31(12):31.

14. Controlled fabrication of triple layered and molecularly defined collagen/elastin vascular grafts resembling the native blood vessel.

Koens, M.J., Faraj, K.A., Wismans, R.G., Vliet van der, J.A., Krasznai, A.G., **Cuijpers, V.M.**, Jansen, J.A., Daamen, W.F., Kuppevelt van , T.H., Acta Biomater. 2010;6(12):4666.

15. Marginal leakage of two newer glass-ionomer-based sealant materials assessed using micro-CT. Chen, X., **Cuijpers, V.M.,** Fan, M., Frencken, J.E., J Dent. 2010;38(9):731.

16. Optimal use of silver nitrate and marginal leakage at the sealant-enamel interface using micro-CT. Chen, X., **Cuijpers, V. M.,** Fan, M., Frencken, J.E., Am J Dent. 2009;22(5):269.

17. Micro-CT for measuring marginal leakage of Class II resin composite restorations in primary molars prepared *in vivo*. Eden, E., Topaloglu-Ak, A., **Cuijpers, V.M.,** Frencken, J.E., Am J Dent. 2008;21(6):393.

18. High resolution magic angle spinning NMR spectroscopy for metabolic assessment of cancer presence and Gleason score in human prostate needle biopsies. Asten van, J.J., **Cuijpers, V.M.,** Hulsbergen- Kaa van de, V., Soede-Huijbregts, C., Witjes, J.A,, Verhofstad, A.A., Heerschap, A., MAGMA. 2008;21(6):435.

19. *In vivo* biocompatibility of ultra-short single-walled carbon nanotube /biodegradable polymer nanocomposites for bone tissue engineering. Sitharaman, B., Shi, X., Walboomers, X.F., Liao, H., **Cuijpers, V.M.,** Wilson, L.J., Mikos, A.G., Jansen, J.A., Bone. 2008;43(2):362.

20. Evaluation of the biocompatibility of calcium phosphate cement/PLGA microparticle composites. Link, D.P., Dolder van den, J., Beucken van den, J.J., **Cuijpers, V.M.**, Wolke, J.G., Mikos, A.G., Jansen, J.A., J Biomed Mater Res A. 2008;87(3):760.

21. Evaluation of bone response to titanium-coated polymethyl methacrylate resin (PMMA) implants by X-ray tomography. Shalabi, M.M., Wolke, J.G., **Cuijpers, V.M.**, Jansen, J.A., J Mater Sci Mater Med. 2007;18(10):2033.

22. Degradable hydrogel scaffolds for *in vivo* delivery of single and dual growth factors in cartilage repair. Holland, T.A,, Bodde, E.W., **Cuijpers, V.M.**, Baggett, L.S., Tabata, Y., Mikos, A.G., Jansen, J.A., Osteoarthritis Cartilage. 2007;15(2):187.

23. Intracellular localization of ornithine decarboxylase and its regulatory protein, antizyme-1. Schipper, R.G., **Cuijpers, V.M.**, Groot de L.H., Thio, M., Verhofstad, A.A., J Histochem Cytochem. 2004;52(10):1259.

24. Induction of hyperammonia in irradiated hepatoma cells: a recapitulation and possible explanation of the phenomenon. Rijn van, J., Berg van den, J., Schipper, R.G., Jong de, S., **Cuijpers, V.M.,** Verhofstad, A.A., Teerlink, T., Br J Cancer. 2004;91(1):150.

25. Polyamines and prostatic cancer. – Review - Schipper, R.G., Romijn, J.C., **Cuijpers, V.M.**, Verhofstad, A.A., Biochem Soc Trans. 2003;31(2):375.

26. Automated identification of diploid reference cells in cervical smears using image analysis. Laak van der, J.A., Siebers, A.G., **Cuijpers, V.M.**, Pahlplatz, M.M., Wilde de, P.C., Hanselaar, A.G., Cytometry. 2002;47(4):256.

27. Quantification of tumour vascularity in squamous cell carcinoma of the tongue using CARD amplification, a systematic sampling technique, and true color image analysis. Hannen, E.J., Laak van der, J.A., Kerstens, H.M., **Cuijpers, V.M**,, Hanselaar, A.G., Manni, J.J., Wilde de, P.C., Anal Cell Pathol. 2001;22(4):183.

28. Practical aspects of fixatives in high resolution nuclear image analysis. Makkus, A.C., Hof van 't- Grootenboer, A.E., Pahlplatz, M.M., Wilde de, P.C., Gemmink, A.J., **Cuijpers, V.M**., Vooijs, G.P., Cytometry. 1994;15(4):302.

29. Immunocytochemical detection of ovarian carcinoma cells in serous effusions. **Cuijpers, V.M.,** Boerman, O.C., Salet- Pol van de, M.R., Vooijs, G.P., Poels, L.G., Ramaekers, F.C., Acta Cytol. 1993;37(3):272.

# Curriculum Vitae

Vincent Cuijpers was born in Boxmeer on December 11th, 1965. In 1985 he graduated from the Elzendaalcollege in Boxmeer, after which he started his studies in Cytology and Histology at the School of Higher Education in Laboratory Sciences in Nijmegen, which he completed in 1991 (BSc). A 12-month internship at the Department of Pathology (prof. dr. G. Vooijs) at the Radboud University Medical Center resulted in a scientific publication on "Immuno-cytochemical detection of ovarian carcinoma cells in serous effusions". From 1992 to 1998 he worked at the "Screening Center Nijmegen" and as a technician at the Department of Pathology, Divisions of Cyto-Histology and Quantitative Microscopy, Radboud University, (prof. dr. T. Hanselaar, later prof. dr. D. Ruiter and prof. dr. H. van Krieken). He attended several international courses and gave presentations on cyto-histological diagnostics and quantitative microscopy. His interest in cyto-histomorphometry arose during an 'In service training' at the British Columbia Cancer Agency, Vancouver, Canada. From 1999 to 2004 he worked as a Research Technician at both Departments of Pathology and Urology (Radboud University), focusing on polyamines related to prostatic cancer. Initiated by Dr. A. Verhofstad†, he attended the

'Digital and Video Microscopy' course at the McCrone Research Institute, Chicago, IL, to expand his knowledge regarding imaging modalities in microscopy. He attended the post-HBO course Molecular Biological Techniques, School of Higher Education Brabant, Etten-Leur, and became a member of the European Cooperation in Science and Technology group, resulting in presentations in Spa (Belgium), Madrid, Barcelona and Malaga (Spain), Vilnius (Lithuania), Trento (Italy) and Larnaca (Cyprus).

Since 2005, he has been working as a Research Technician at the Department of Biomaterials of the faculty of Dentistry (prof. dr. J. Jansen), were he started his PhD research in 2010 (supervisors: prof. dr. J.A. Jansen and dr. X.F. Walboomers). He attended several international symposia and meetings on microscopy, micro-computed tomography (micro-CT) and image analysis, presenting posters and giving presentations in London (United Kingdom), Porto (Portugal), Saint Petersburg (Russia), Singapore, Shanghai (China), Riyadh (Saudi Arabia) and Melbourne (Australia). Due to his interest in X-ray micro-CT, especially synchrotron radiation, he visited both the Singapore Synchrotron Light Source (SSLS) and the Australian Synchrotron. Furthermore, he collaborated with several departments of the Radboud University, as well as the Warsaw University of Technology, Faculty of Materials Science and Engineering, Biomaterials Group, Warsaw, Poland, (Dr. W. Święszkowski) and the King Saud University, College of Dentistry, Division of Periodontics, Riyadh, Saudi Arabia, (Dr. A. Al Farraj Aldosari).
Vincent is married to Angélica and they have two children, Savannah (21) and Youri (20).

*"The contemplation of celestial things will make a man both speak and think more sublimely and magnificently when he descends to human affairs"*

Marcus Tullius Cicero, roman philosopher, politician, orator and writer, 106 B.C. – 43 B.C.

## SPONSORS:

Radboud University Medical Center, Nijmegen
Bruker microCT N.V., Kontich, Belgium
Alicona Imaging GmbH, Raaba, Austria
Cam Bioceramics B.V., Leiden